

SeCURE

Saltwater intrusion and climate change: monitoring, countermeasures and informed governance

Deliverable 2.2.7 – Articles in international magazines

July 2023 – Final version

Contributing partners:

LP – UNIPD, PP1 – CNR-IGG, PP2 – REGVEN, PP3 – UNIST,

PP4 – DUNEA, PP5 – PIDNC, PP6 – CW

Table of Contents

| | |
|--|----------|
| 1. INTRODUCTION | 3 |
| 2. THE SECURE PUBLICATIONS | 3 |
| 2.1 Articles in magazine | 3 |
| 2.2 Abstracts in international conference proceedings | 6 |
| 2.3 Papers in international scientific journals | 9 |

1. Introduction

This deliverable collects the publications produced as part of the SeCure project. Totally, we published 2 articles in on-line/printed magazines, 3 abstracts in the most important international conferences on geosciences (AGU Fall Meeting and EGU Annual Meeting), 3 papers in international scientific journals.

2. The SeCure publications

2.1 Articles in magazine

- Kamber S., J. Prpić J. & I. Lavrinović I. (2022). Zaslavljenje vodonosnika-prijetnja obalnim regijama, *Hrvatska Vodoprivreda*, 240, 56-60, 2022.

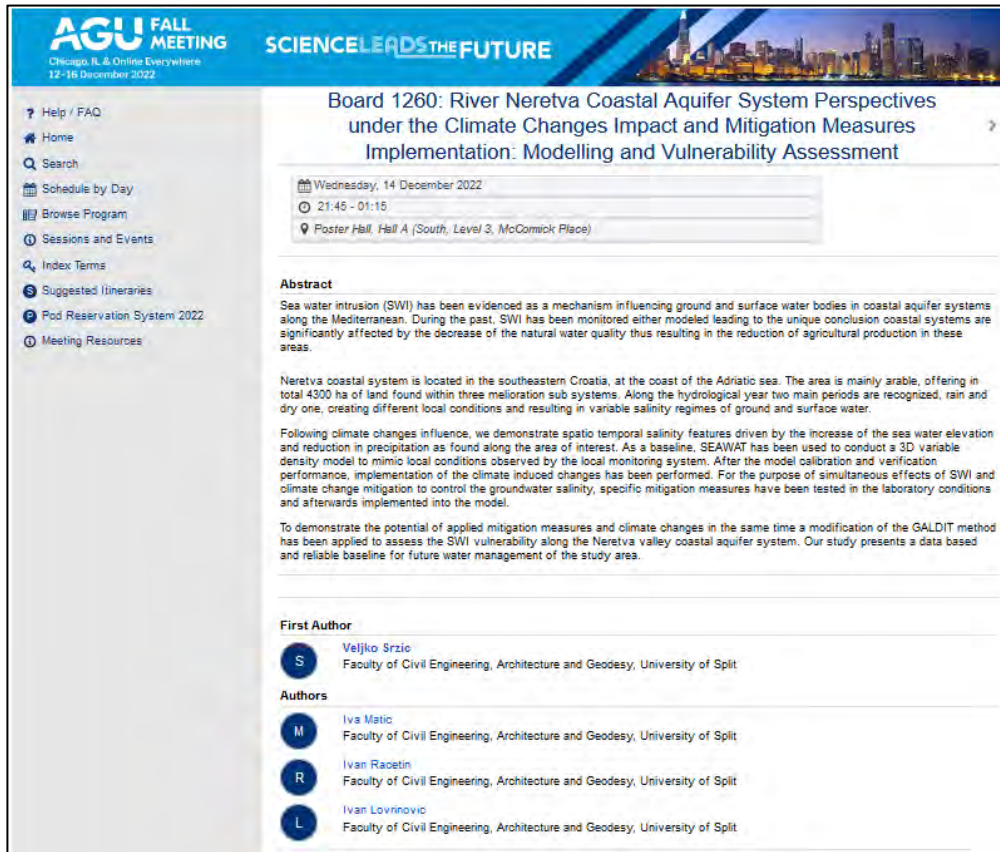


- SeCure Project (2023). Sea water in the lowlands: Ongoing study, *Platinum*, 16(46), 204, 2023.



2.2 Abstracts in international conference proceedings

- Srzic V., Matic I., Racetin I., & Lavrinović I. (2022). River Neretva Coastal Aquifer System Perspectives under the Climate Changes Impact and Mitigation Measures Implementation: Modelling and Vulnerability Assessment, *AGU Fall Meeting, 2022*.



AGU FALL MEETING
Chicago, IL & Online Everywhere
12-16 December 2022

SCIENCE LEADS THE FUTURE

Board 1260: River Neretva Coastal Aquifer System Perspectives under the Climate Changes Impact and Mitigation Measures Implementation: Modelling and Vulnerability Assessment

Wednesday, 14 December 2022
21:46 - 01:16
Poster Hall, Hall A (South, Level 3, McCormick Place)

Abstract

Sea water intrusion (SWI) has been evidenced as a mechanism influencing ground and surface water bodies in coastal aquifer systems along the Mediterranean. During the past, SWI has been monitored either modeled leading to the unique conclusion coastal systems are significantly affected by the decrease of the natural water quality thus resulting in the reduction of agricultural production in these areas.

Neretva coastal system is located in the southeastern Croatia, at the coast of the Adriatic sea. The area is mainly arable, offering in total 4300 ha of land found within three meioration sub systems. Along the hydrological year two main periods are recognized, rain and dry one, creating different local conditions and resulting in variable salinity regimes of ground and surface water.

Following climate changes influence, we demonstrate spatio temporal salinity features driven by the increase of the sea water elevation and reduction in precipitation as found along the area of interest. As a baseline, SEAWAT has been used to conduct a 3D variable density model to mimic local conditions observed by the local monitoring system. After the model calibration and verification performance, implementation of the climate induced changes has been performed. For the purpose of simultaneous effects of SWI and climate change mitigation to control the groundwater salinity, specific mitigation measures have been tested in the laboratory conditions and afterwards implemented into the model.

To demonstrate the potential of applied mitigation measures and climate changes in the same time a modification of the GALDIT method has been applied to assess the SWI vulnerability along the Neretva valley coastal aquifer system. Our study presents a data based and reliable baseline for future water management of the study area.

First Author

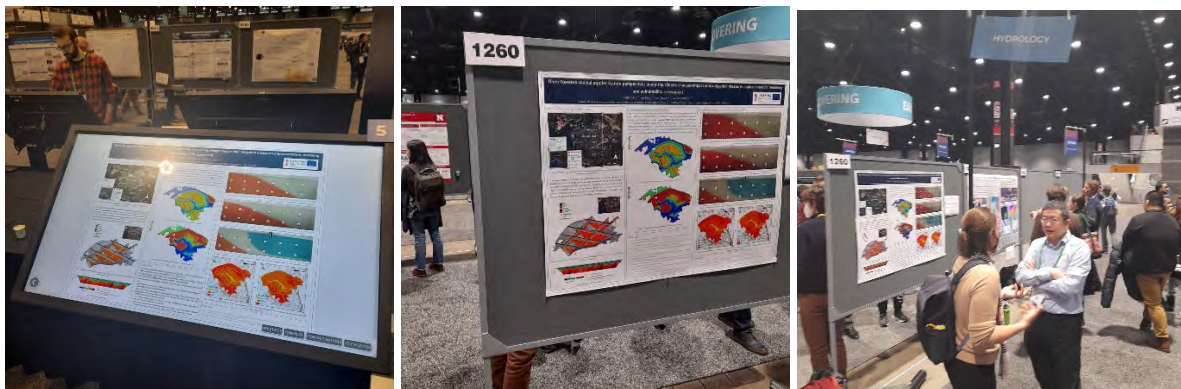
S Veljko Srzic
Faculty of Civil Engineering, Architecture and Geodesy, University of Split

Authors


M Iva Matic
Faculty of Civil Engineering, Architecture and Geodesy, University of Split

R Ivan Racetin
Faculty of Civil Engineering, Architecture and Geodesy, University of Split


L Ivan Lovnovic
Faculty of Civil Engineering, Architecture and Geodesy, University of Split



- Cosma, M., Zancanaro, E., Aljinović, I., Morari, F., Srzić, V., Teatini, P., Tosi, L., Bergamasco, A., Botto, A., Camporese, M., Cavallina, C., Da Lio, C., Donnici, S., Lovrinović, I., Racetin, I., Zaggia, L., Zoccarato, C., and Salandin, P.: Approaches and methodologies to monitor and mitigate saltwater intrusion in the Adriatic coastal plains, *EGU General Assembly 2023*, EGU23-12125, <https://doi.org/10.5194/egusphere-egu23-12125>, 2023.



EGU23-12125, updated on 16 Sep 2023
<https://doi.org/10.5194/egusphere-egu23-12125>
 EGU General Assembly 2023
 © Author(s) 2023. This work is distributed under the Creative Commons Attribution 4.0 License.



Approaches and methodologies to monitor and mitigate saltwater intrusion in the Adriatic coastal plains

Marta Cosma¹, Ester Zancanaro², Iva Aljinović³, Francesco Morari⁴, Veljko Srzić³, Pietro Teatini², Luigi Tosi¹, Alessandro Bergamasco³, Anna Botto², Matteo Camporese², Chiara Cavallina¹, Cristina Da Lio¹, Sandra Donnici¹, Ivan Lovrinović³, Ivan Racetin³, Luca Zaggia¹, Claudia Zoccarato², and Paolo Salandin²

¹Institute of Geosciences and Earth Resources, National Research Council, Padova, Italy
²Department of Civil, Environmental and Architectural Engineering (ICEA), University of Padova, Padova, Italy
³Faculty of Civil Engineering, Architecture and Geodesy, University of Split, Split, Croatia
⁴Department of Agronomy, Food, Natural resources, Animals and Environment (DAFNAE), University of Padova, Padova, Italy
⁵Institute of Marine Science, National Research Council, Venezia, Italy


Saltwater intrusion in coastal aquifers is a global problem recently worsened by anthropogenic activities (e.g., aquifer overexploitation, hydraulic reclamation and drainage of low-lying areas) and climate change effects (e.g., severe droughts, sea level rise) that contribute to reduce groundwater natural recharge, water quality, and agricultural production. Many low-lying coastal plains facing the Adriatic Sea are strongly affected by saltwater intrusion with serious consequences on agricultural activities and tourism that may become dramatic in a relatively short time due to climate change. In this framework, this work aims to identify monitoring strategies to characterize the process of saltwater intrusion under the effects of climate change and recommend appropriate countermeasures in two Adriatic low-lying coastal plain: south of the Venice Lagoon (north-eastern Italy), and at the Neretva River mouth (south-eastern Croatia).

Geomorphologic, stratigraphic, hydrogeologic, and agricultural data were collected to characterize the aquifer system at both sites and assess the effects of seawater intrusion on agricultural productivity. Saltwater intrusion was monitored and analysed through monitoring systems that provide qualitative and quantitative information on the processes influencing groundwater and surface water dynamics within the two coastal systems. Moreover, laboratory physical models were developed to serve as benchmarks for the numerical models used to simulate the field results. Numerical modelling reliably implements boundary and initial conditions defined in-situ on both sites, simulates existing states, specifies different scenarios, and predicts salinization dynamic changes caused by climate changes.


The results of the research activities include the development of specific tools for the management of agriculture-related activities and freshwater resources in coastal areas including vulnerability assessment, mitigation plans, and countermeasures against salt contamination. These results were obtained by integrating the findings gained on both sites, considering differences and peculiarities of the specific areas that are representative of many low-lying plains located on both sides of the Adriatic coast.

This study has been funded by the contribution from the EU cofinancing and the Interreg Italy-Croatia Cross Border Collaboration (CBC) Programme 2014–2020 (Priority Axes: Safety and Resilience) through the European Regional Development Fund as a part of the projects MoST (AID: 10047742) and SeCure (AID: 10419304).

- Lovrinovic, I., Aljinovic, I., and Srzic, V.: Evaluation of surface and groundwater quality and identification of saltwater sources by hydrogeochemical analysis in river Neretva coastal aquifer system, *EGU General Assembly 2023*, , EGU23-11976, <https://doi.org/10.5194/egusphere-egu23-11976>, 2023.



EGU23-11976, updated on 16 Sep 2023
<https://doi.org/10.5194/egusphere-egu23-11976>
EGU General Assembly 2023
© Author(s) 2023. This work is distributed under
the Creative Commons Attribution 4.0 License.



Evaluation of surface and groundwater quality and identification of saltwater sources by hydrogeochemical analysis in river Neretva coastal aquifer system

Ivan Lovrinovic, Iva Aljinovic, and Veljko Srzic
University of Split, Faculty of Civil Engineering, Architecture and Geodesy, Split, Croatia (ivan.lovrinovic@gradst.hr)

The river Neretva coastal aquifer system is the largest agricultural area along Croatia's Adriatic Sea coast. With the construction of an embankment, pumping stations, and melioration channels, a once-marshy area has been transformed into an area with favourable agricultural conditions. Due to its proximity to the sea, numerous anthropogenic impacts in the region, and climate change, groundwater and surface water in the study area are presently significantly influenced by the salinization process.

Multiple times per year, groundwater and surface water samples are collected to fully comprehend saltwater processes and the origin of saltwater in the study area. Within each sample, the concentration of major ions (K⁺, Na⁺, Ca⁺, Mg²⁺, Cl⁻, HCO₃⁻ and SO₄²⁻) is determined under laboratory conditions.

The analysis of major ions indicates that seawater intrusion is the primary source of salinization in both unconfined and confined aquifers. In contrast to unconfined aquifer, confined aquifer is minimally affected by precipitation and surface water regimes. In addition, samples of groundwater from unconfined aquifer are categorized into three groups based on their degree of contamination with seawater. The samples from the Diga area that are closest to the Adriatic Sea are most significantly influenced by the seawater. The groundwater quality in the Jasenska area varied significantly between dry and rain periods, whereas groundwater samples from the area of Vidrice revealed the lowest level of seawater contamination. Neretva river surface water samples reveal the presence of a salt wedge, while river Mala Neretva samples indicate that river Mala Neretva is the primary source of freshwater in the study area during dry season.

2.3 Papers in international scientific journals

- Zancanaro E., Zoccarato C., Morari F., & Teatini P. (2023). Estimation of hydraulic parameters in a heterogeneous low-lying farmland near Venice. *Hydrological Processes*, 37(1), e14791. <https://doi.org/10.1002/hyp.14791>.

RESEARCH ARTICLE

WILEY

Estimation of hydraulic parameters in a heterogeneous low-lying farmland near Venice

Ester Zancanaro¹ | Claudia Zoccarato¹ | Francesco Morari² | Pietro Teatini¹

¹Department of Civil, Environmental and Architectural Engineering (ICEA), University of Padova, Padova, Italy

²Department of Agronomy, Food, Natural Resources, Animals and Environment (DAFNAE), University of Padova, Legnaro, Italy

Correspondence

Ester Zancanaro, Department of Civil, Environmental and Architectural Engineering (ICEA), University of Padova, Via Marzolo, 9, 35131 Padova, Italy.
Email: ester.zancanaro@unipd.it

Funding information

European Regional Development Fund

Abstract

Estimating the hydraulic properties of the vadose zone is essential to understand soil-water dynamics and achieving appropriate water management in agricultural lands. Inverse modelling methods are commonly used to estimate hydraulic properties from field observations. Unlike the extensively applied local search methodologies, data assimilation techniques can fully account for multiple uncertainties and are becoming a widely used tool for estimating hydraulic parameters. However, only few applications on real field tests are available. The main objective of this study was to estimate the van Genuchten-Mualem (VGM) parameters and the saturated hydraulic conductivity (K_s) of a heterogeneous low-lying farmland at the margin of the Venice Lagoon, Italy, characterized by high peat content, sandy drifts, and a very shallow water table. To this end, two methods were tested, that is, the Ensemble Smoother (ES) and the Levenberg-Marquardt (LM) algorithm associated with hydrological modelling performed with Hydrus-1D. Volumetric water content (VWC) observations were collected at three monitoring sites from May to September 2011. Results on parameters highlighted that the ES technique effectively reduced the uncertainty of α and n , but it was less effective on θ_r and K_s . The results on VWC showed that the ES efficiency decreased with the increasing non-linearity of the system (e.g., higher sand content) and when the variability of the experimental data was lower (e.g., deepest soil layers where saturation remained permanently close to 1). Both LM and ES allowed to reproduce the VWC observations in the calibration and validation phases, with the former and the latter performing better in the case of sandy and peat soils, respectively. As concerns the method applicability, the ES was less time-demanding as it efficiently updated all the parameters at once and was less dependent on the user choices. Finally, the paper points out the importance of previous knowledge of the VGM parameters (e.g., from lab hydraulic analyses) in defining the constraints for the optimization.

KEYWORDS

data assimilation, ensemble smoother, Hydrus-1D, soil hydraulic properties, vadose-zone hydrology

1 | INTRODUCTION

The hydraulic characterization of the vadose zone is fundamental to understand water flow dynamics, particularly in agricultural fields with heterogeneous soil characteristics. Soil hydraulic properties such as soil water retention and hydraulic conductivity can be directly estimated by laboratory techniques applied on relatively small soil samples. However, these methods are time-consuming and results are strongly affected by the sample dimensions (Hopmans et al., 2002; Ramos et al., 2006; Valdes-Abellan et al., 2018; Vrugt et al., 2008). Moreover, conventional methods may be inadequate to investigate the hydraulic properties of peat soils due to their peculiar characteristics such as high porosity, low bulk density, high compressibility, and their swelling and shrinking capacity during wetting and drying cycles (Dettmann et al., 2019; Kechavarzi et al., 2010; Rezaeezad et al., 2016; Schwärzel et al., 2002).

Inverse modelling may be instead a powerful tool for the estimation of hydraulic parameters from field observations such as volumetric water content (VWC) and matric potential (h). Hydraulic parameters calibration is usually performed by iteratively solving the non-linear governing flow equation (i.e., the Richards' equation) to minimize the difference between observed and predicted variables. The final solution is gained when the model approximates as closely as possible the observed field response (Hopmans et al., 2002; Vrugt et al., 2008). Local search methodologies, such as the Levenberg–Marquardt (LM) algorithm (Marquardt, 1963), have been widely used when calibrating soil hydraulic parameters at the field scale (Abbasi et al., 2004; Abbasi, Jacques, Simunek, Feyen, & van Genuchten, 2003; Abbasi, Jacques, Simunek, Feyen, van Genuchten, & Shouse, 2003; Alletto et al., 2015; Jacques et al., 2002; Qu et al., 2014; Ramos et al., 2006). However, local optimization algorithms are very sensitive to the initial point in the parameter space and, for this reason, they may find a local minimum instead of a global unique solution (Simunek et al., 2012; Wholing et al., 2008). Global optimization algorithms may face the problem of non-uniqueness related to local search methods by using many simultaneous searches from different starting points. Many global optimizers have been developed and applied to hydrological modelling (Vrugt et al., 2008). Among those, one example is the particle swarm optimization that was recently applied both alone (Brunetti et al., 2016) or in combination with local search methods (Brunetti et al., 2022; Cao et al., 2019). Despite the successful applications of optimization-based inverse methodologies, they are mainly focused on the identification of a unique set of parameters without quantifying the uncertainties related to boundary conditions, field measurements, and modelling itself (Gao et al., 2019; Vrugt et al., 2005, 2008).

Data assimilation (DA) techniques based on a Bayesian approach can account for multiple uncertainties. Among those, ensemble methods (Evensen, 1994) have been widely applied in soil hydrology to update model states or to jointly update states and parameters. The ensemble Kalman filter (EnKF) and its variations are the most popular methods in soil hydrology. EnKF is a sequential DA approach that updates the investigated variables whenever new measurements

are made available. Most of the literature studies deal with synthetic applications (Brandhorst et al., 2017; Medina et al., 2014; Moradkhani et al., 2005; Shi et al., 2015; Song et al., 2014), and only a few authors applied ensemble methods using field datasets. For example, Narenda and Mohanty (2006) employed the EnKF approach to assimilate periodic remote sensed soil moisture data and estimate the root zone soil moisture. Rasmussen et al. (2015) and Zhang et al. (2016) investigated the performance of the ensemble transform Kalman filter (ETKF) in assimilating real observations to update multiple states with a coupled surface-subsurface flow model. The EnKF was also applied in real test cases to jointly update model state and parameters in a drainage experiment with a limited amount of data (Li & Ren, 2011). More recently, Botto et al. (2018) used the EnKF in combination with a Richards' equation-based hydrological model to test its efficacy in reducing the uncertainties of different states and parameters by assimilating observations collected during artificial hillslope experiments with controlled boundary conditions. Jiang et al. (2019) couple the EnKF with Hydrus-1D model to update the parameters of water movement and solute transport, soil moisture and salinity states by assimilating sparse field observations derived from soil sampling and analysis. Nevertheless, real field cases are characterized by uncontrolled boundary conditions that introduce multiple uncertainties. For this reason, using a limited number of observations distributed over a short time window can be insufficient when optimizing soil hydraulic parameters.

Despite EnKF successful applications, some authors reported that this method might be unsuitable for strongly non-linear processes such as groundwater flow in variably saturated conditions (Shi et al., 2015; Zha et al., 2019). Moreover, EnKF was originally developed for dynamic state forecasting (Moradkhani et al., 2005) and performs sequential updates at each available observation time. This requires the updating routine to be included in the model code or the simulation to be stopped and restarted with the new parameters (Bailey & Baù, 2010) making this method less efficient when estimating constant parameters, for example, van Genuchten–Mualem (VGM) soil hydraulic parameters. Li and Ren (2011) and Shi et al. (2015) reported that EnKF performed properly only when estimating a low number of parameters simultaneously.

Although its applications in the field of vadose zone hydrology are scarce, the Ensemble Smoother (ES) is an ensemble method that can address the EnKF issues highlighted by many authors and described above. The ES assimilates all the available observations in one step, and it computes a global update in the space–time domain (van Leeuwen & Evensen, 1996). For this reason, ES is considered more suitable when updating time-independent parameters (Bailey & Baù, 2010; Emerick & Reynolds, 2013). Despite the assumption of prior probability density functions (PDFs) Gaussianity that leads to a linear update equation, van Leeuwen (2001) demonstrated that the ES can also handle nonlinear processes. Moreover, Skjervheim et al. (2011) and Crestani et al. (2013) showed a strong reduction in the computational time of ES if compared with EnKF. Up to now, the ES method was applied by Bailey and Baù (2010) and by Crestani et al. (2013) to retrieve the hydraulic conductivity

distribution in two-dimensional groundwater flow and transport synthetic experiments. More recently, Cui et al. (2020) designed different synthetic experiments to evaluate the use of Ground Penetrating Radar (GPR) data as observations to calibrate the VGM parameters via ES with multiple data assimilation (ES-MDA). However, there is still a lack of knowledge on ES performance in the joint update of model states and parameters in variably saturated soils under real field conditions.

The present study aims to characterize the soil hydraulic properties of a low-lying agricultural field at the southern boundary of the Venice Lagoon, Italy, where two main peculiarities make model inversion even more challenging than usual: (i) heterogeneous soil properties with large peat content and (ii) a very shallow water table (i.e., approximately 1-m deep) kept almost constant by an artificial drainage system. VWC observations were daily acquired at four depths in three locations chosen within the study area to explore the wide variability of the soil organic content. The θ_r , α , n , and K_s VGM parameters were optimized using two methods: (i) the ES algorithm, which assimilates VWC records to reduce the uncertainty on parameters, and (ii) the Levenberg–Marquardt algorithm, which is implemented in Hydrus-1D for parameter calibration and uncertainty analysis. The effectiveness of the two methods in characterizing the hydraulic properties of the different soil types was investigated, with the observations split into calibration and validation periods to check the robustness of the calibrated model.

2 | MATERIALS AND METHODS

2.1 | Experimental site

The experimental site is a 21-ha agricultural field located at Ca' Bianca, Chioggia, North-East of Italy (45°10'57" N, 12°13'55" E, UTM, WGS84), along the southern margin of the Venice Lagoon

(Figure 1). It is bounded by the Morto Channel, Brenta, and Bacchiglione rivers. In the past, the area was occupied by swamps until it was reclaimed for agricultural purposes between the years 1892 and 1967. The site is affected by seawater intrusion and lies below the mean sea level (msl), with the elevation ranging from -1 m to -3.3 m msl. For this reason, the water table is very shallow and kept at a suitable depth for farming by a dense network of open ditches and a pumping station that drives the excess water into the lagoon. The depth to the water table ranges from 0.5 to 1.8 m below the soil surface (bss), with small vertical fluctuation (ca 0.5 m) during the year. Usually, the water table is maintained shallow during the summer periods to promote sub-irrigation.

The soil is heterogeneous, mainly silty clay (Molli-Gleyic Cambisols, FAO-UNESCO, 1989), with acidic peat deposits formed from the reedbeds and swamps in place before the reclamation and sandy drifts derived from past fluvial ridges and coastal strips. The dataset used in the present test was collected during the year 2011. The field was cultivated with rainfed maize (seeding 4th April and harvesting 2nd September). Soil tillage was an autumn ploughing to the 0.3 m depth, followed by standard seedbed preparation operations.

2.1.1 | Monitoring network

Five soil-water monitoring sites, A, B, C, D, and E were placed in five site-specific management units (SSMUs) based on apparent soil electrical conductivity and bare-soil reflectance (Scudiero et al., 2013) (Figure 1). Each one was equipped with four capacitance-resistance probes (ECH2O-5TE, Decagon Devices, Pullman, WA) for volumetric water content (VWC) monitoring installed at 0.1, 0.3, 0.5, and 0.7 m depths and connected to a datalogger (EM50, Decagon Devices, Pullman, WA) that recorded hourly data. The capacitance-resistance probes were previously calibrated in the laboratory with an accuracy of $\pm 3.8\%$ (Scudiero et al., 2012).

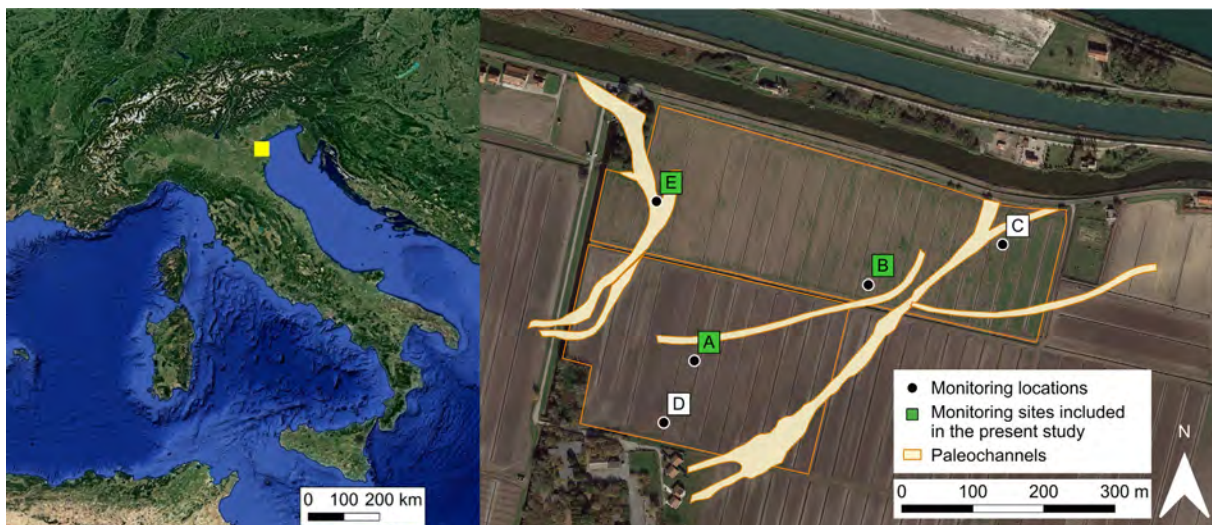


FIGURE 1 Location of the study area in Northern Italy and map showing the monitoring sites (A–E), the ones included in the present study (A, B, and E), and the main paleochannels

Moreover, a 2 m deep piezometer was installed at each site to monitor the depth to the water table weekly. To the end of this study, sites A, B, and E (Figure 1) were selected for their heterogeneous and exemplificative characteristics: site A is located in a peaty and silty area; site B partially intercepts the sandy paleochannel being characterized by a loamy soil in the upper layers and by a sandy soil in the bottom ones; site E is located in the coarse northwest paleochannel. Meteorological data were recorded from a weather station located 3 km from the study area by the Regional Agency for Environmental Protection, Veneto Region.

2.1.2 | Soil sampling and analysis

Disturbed soil samples were collected at four depth intervals (0–0.15, 0.15–0.45, 0.45–0.80, and 0.80–1.20 m) and analysed for soil texture (Mastersizer 2000, Malvern Instruments Ltd., Great Malvern, UK), pH, electrical conductivity (EC measured on the 1:2 soil–water extract, SevenMulti pH/conductivity meter, Mettler Toledo, Greifensee, Switzerland), total and organic carbon (SOC, CNS Vario Macro-elemental analyzer, Elementar, Hanau, Germany).

Undisturbed soil cores (0.07 m diameter, 0.06 m height) were collected with a hydraulic sampler to perform the hydraulic characterization of the upper 1 m vadose zone. Samples were removed at the four depths 0.05–0.11, 0.25–0.31, 0.45–0.51, and 0.65–0.71 m. Saturated hydraulic conductivity (K_s) was measured using a laboratory permeameter (Eijkelpkamp, Giesbeek, The Netherlands). Unsaturated hydraulic conductivity and retention curves were determined applying the Wind method (Dane & Topp, 2002) using the Ku-pF Apparatus DT 04-01 (Umwelt-Geräte-Technik GmbH, Müncheberg, Germany). Samples were then oven-dried at 105°C for 24 h to calculate bulk densities. Hydrus-1D numerical model (Simunek et al., 2015) was applied to invert Richards' equation and estimate van Genuchten-Mualem parameters from the lab pressure–water content measurements (Bevington et al., 2016, 2019).

2.2 | Unsaturated water flow modelling with Hydrus-1D

Hydrus-1D is a finite element modelling software (Simunek et al., 2015) for simulating the one-dimensional (1D) water flow, heat, and multiple solutes in variably saturated porous media. Hydrus-1D numerically solves the modified form of the Richards' equation:

$$\frac{\partial \theta}{\partial t} = \frac{\partial}{\partial z} \left[K(h) \left(\frac{\partial h}{\partial z} + 1 \right) \right] - S, \quad (1)$$

where, θ is the volumetric water content ($\text{m}^3 \text{m}^{-3}$), t the time (days), h the water pressure head (m), z the vertical spatial coordinate (m), $K(h)$ the unsaturated hydraulic conductivity function written as a function of h (m days⁻¹). S is the sink/source term and is defined as the volume of water removed/added from/into a unit volume of soil per unit time

due to external factors such as plant water uptake, evaporation, drainage, and precipitation ($\text{m}^3 \text{m}^{-3} \text{days}^{-1}$).

In the specific case of interest, the sink term is represented by precipitation, evaporation, and root water uptake. Concerning the latter, its contribution is given by Equation (2):

$$S(h) = a(h)S_p, \quad (2)$$

where the function $a(h)$ is the root-water uptake water stress response and S_p (days⁻¹) is the potential water uptake rate (Feddes et al., 1978; Simunek et al., 2015). Feddes' parameters for maize were selected from the database developed by Wesseling et al. (1991). S_p was not uniformly distributed over the root zone and can be described by means of the generalized Equation (3):

$$S_p = b(x)T_p, \quad (3)$$

where, $b(x)$ is the normalized water uptake distribution that describes the spatial variation of S_p (m^{-1}) and T_p is the potential transpiration rate (m day^{-1}). The rooting depth varied with time during the crop season. For this reason, the shape of $b(x)$ was described using the root distribution model proposed by Hoffman and van Genuchten (1983), while the Verhulst-Pearl logistic growth function was used to describe the root growth during the growing season. The root growth factor was calculated by assuming that 50% of the rooting depth was reached at the midpoint of the growing season (Dal Ferro et al., 2014; Vamerali et al., 2006).

Soil water retention, $\theta(h)$, and hydraulic conductivity, $K(h)$, were parameterized according to the VGM model:

$$\theta(h) = \begin{cases} \theta_r + \frac{\theta_s - \theta_r}{[1 + |\alpha h|^{n_1}]^m} & h < 0 \\ \theta_s & h \geq 0 \end{cases}, \quad (4)$$

$$K(h) = K_s Se^l \left[1 - (1 - Se^{3m})^m \right]^2, \quad (5)$$

where, θ_r and θ_s are the residual and saturated water content ($\text{m}^3 \text{m}^{-3}$), respectively, α the inverse of the air-entry value (m^{-1}), n and m the pore size distribution indexes with $m = (1 - 1/n)$, K_s the saturated hydraulic conductivity (m days^{-1}), and l the pore connectivity parameter. θ_s , θ_r , and K_s have physical meaning, while n , m , and l are empirical parameters that determine the shape of water retention and hydraulic conductivity curves (van Genuchten, 1980).

2.3 | Model calibration

Three simulations of field conditions were performed, one per each monitoring site (A, B, E). The field observations were split into two periods, one for model calibration from 5/17/2011 to 7/17/2011 and one for validation from 7/18/2011 to 9/23/2011. The calibrated parameters were θ_r , α , n , and K_s , while θ_s and l were a priori known. θ_s values were derived from available lab tests on undisturbed soil samples and differ for each soil layer. The value of l was set equal to 0.5 in

all layers and scenarios as generally assumed in field-scale simulations (Mualem, 1976; Wosten & van Genuchten, 1988).

In the following paragraphs, the ES approach and the LM algorithm, as implemented in Hydrus-1D, are briefly introduced.

2.3.1 | The ensemble smoother

The ES is a data assimilation algorithm based on Monte Carlo simulations, originally proposed by van Leeuwen and Evensen (1996). The ES is a variance-minimizing estimate that simultaneously assimilates all available observations in space and time. In this application, the ES is used to infer and reduce the uncertainty of the VGM parameters using VWC observations.

The ES is built on two steps, prior analysis and update. The prior analysis involves the simulation of an ensemble of model states, that is, VWC, based upon the solution of a numerical model which depends on uncertain input parameters defined by a probability distribution function. The ensemble of model states $\Psi(\mathbf{x}, t) \in \mathbb{R}^{n_\Psi \times N}$ is augmented with the uncertain parameters $\xi(\mathbf{x}) \in \mathbb{R}^{n_\xi}$, so that the matrix $A(\mathbf{x}, t) = [\Psi(\mathbf{x}, t); \xi(\mathbf{x})] \in \mathbb{R}^{n_{\Psi\xi} \times N}$ holds the N ensemble members of Ψ at time t and position \mathbf{x} and the parameters ξ at position \mathbf{x} :

$$A(\mathbf{x}, t) = \begin{pmatrix} \psi_{1,1}(\mathbf{x}, t) & \cdots & \psi_{1,N}(\mathbf{x}, t) \\ \vdots & \ddots & \vdots \\ \psi_{n_\Psi,1}(\mathbf{x}, t) & \cdots & \psi_{n_\Psi,N}(\mathbf{x}, t) \\ \alpha_{1,1}(\mathbf{x}) & \cdots & \alpha_{1,N}(\mathbf{x}) \\ \vdots & \ddots & \vdots \\ \alpha_{n_\alpha,1}(\mathbf{x}) & \cdots & \alpha_{n_\alpha,N}(\mathbf{x}) \end{pmatrix}, \quad (6)$$

with $n_{\Psi\xi} = n_\Psi + n_\xi$, and n_Ψ the number of states at all positions and time steps and n_α the size of the parameter space.

In the update step state and parameters are informed according to the following linear unbiased smoother estimate written in matrix form as:

$$A^u = A^p + K(D - HA^p), \quad (7)$$

where, A^u and A^p are the update and prior matrices of the augmented state, that is, state variables and parameters, $H \in \mathbb{R}^{n_d \times n_{\Psi\xi}}$ is a matrix of binary constants (0 or 1) used to map the model state output nodes into the observation locations, and $D \in \mathbb{R}^{n_d \times n_d}$ is the matrix of observations $\mathbf{d}(\mathbf{x}, t)$ perturbed by an ensemble of Gaussian noises $\epsilon \sim \mathcal{N}(0, C_o)$ with $C_o \in \mathbb{R}^{n_d \times n_d}$ the error covariance matrix and n_d the number of available observations. The matrix K is referred to as Kalman gain and calculated as:

$$K = C_p H^T (H C_p H^T + C_o)^{-1}, \quad (8)$$

where, C_p is the covariance matrix of the prior state A^p computed from the prior ensemble. Matrix K weights the residuals $D - HA^p$

according to model and observation errors. Uniform probability distribution functions (PDFs) were used to model parameter uncertainty. The choice of PDFs minimum and maximum values was based on previous knowledge about the hydraulic characteristics of the experimental site (Bevington et al., 2016). ES approach assumes PDFs for model prediction to be Gaussian meaning that they can be represented using only their mean and covariance and a linear update equation can then be used (Evensen, 2009).

A number of 500 realizations were sampled from a priori PDFs of the parameters. The ensemble size properly reproduced the selected statistics for each parameter, leading to linearly shaped cumulative distribution functions (CDFs). A Monte Carlo simulation was performed by running Hydrus-1D hydrological model. One simulation of water content (state forecast) over the 'calibration' time period was generated for each realization of the parameter set (parameter forecast). The available observations were then assimilated by applying the ES algorithm to update state and model parameters. The validation procedure consists of sampling a new ensemble of 500 members from the posterior parameter PDFs and running a Monte Carlo simulation by means of Hydrus-1D (forecast). Finally, mean, 10th, 50th, and 90th percentiles of the generated model state were calculated.

2.3.2 | The Marquardt–Levenberg parameter estimation technique implemented in Hydrus-1D

Hydrus-1D uses the LM algorithm for the inverse estimation of soil hydraulic parameters from measured data. This approach is a local optimization gradient method that requires knowledge about the initial estimate of the parameter to be optimized (Radcliffe & Simunek, 2010; Simunek et al., 2012; Simunek & Hopmans, 2002). The objective function J to be minimized is defined by:

$$J = \sum_{i=1}^{n_d} w_i [d_i - \psi_i]^2 + \sum_{j=1}^{n_\alpha} \hat{v}_j [\alpha_j^* - \alpha_j]^2, \quad (9)$$

where the first term represents the deviation between measured and calculated space–time variables (i.e., VWC at different locations and times) and the second term is a penalty function accounting for the deviation between prior knowledge of the soil hydraulic parameters α_j^* and their estimates α_j . The weights w_i associated with VWC values were set equal to the reciprocal of the error variance of the observations, while \hat{v}_j are pre-assigned weights for the parameters computed from the standard deviation of the prior probability distribution functions.

The parameters calibration procedure consisted of a number of optimization cycles equal to the number of parameters to be optimized. At each cycle, all the parameters were inverted except for one because the uncertain parameters of sites B and E exceeded the fixed number that can be simultaneously optimized by Hydrus-1D. The optimization procedure was consistent among the monitoring sites and avoids discrepancies due to user choices. As Hydrus-1D minimization is sensitive to the initial parameter values (Simunek et al., 2012), the procedure was repeated with five different sets.

2.3.3 | Metrics

The performances of ES and LM algorithms were evaluated using the root mean square error (RMSE, Equation 10), the mean absolute error (MAE, Equation 11), and the Nash Sutcliffe model Efficiency (NSE, Equation 12):

$$\text{RMSE} = \sqrt{\frac{1}{n_d} \sum_{i=1}^{n_d} (S_i - O_i)^2}, \quad (10)$$

$$\text{MAE} = \frac{1}{n_d} \sum_{i=1}^{n_d} |S_i - O_i|, \quad (11)$$

$$\text{NSE} = 1 - \frac{\sum_{i=1}^{n_d} (O_i - S_i)^2}{\sum_{i=1}^{n_d} (O_i - \bar{O})^2}, \quad (12)$$

where, O_i is the i th observation and \bar{O} their mean value, S_i the predicted value.

The NSE is a normalized statistic that evaluates the relative magnitude of the residual variance compared to the measured data variance. It ranges between $-\infty$ and $+1$ with the optimal value $= +1$. Values between 0 and $+1$ mean acceptable modelling performances (Moriassi et al., 2007; Nash & Sutcliffe, 1970).

2.4 | Model setup

2.4.1 | Water flow boundary conditions

Atmospheric conditions with surface runoff and variable pressure head were imposed as upper and lower boundaries of the model domain, respectively. Initial conditions were specified in terms of VWC. Specifically, the time-variable boundary conditions were precipitation, evaporation, transpiration on the model top, and groundwater level at the bottom. Daily values were provided in agreement with the selected time step (1 day). Rainfall data were obtained from the weather station (see Section 2.1). The reference evapotranspiration (ET_0) was computed according to the Penman-Monteith equation. Crop evapotranspiration under standard conditions (ET_c) was then calculated following the FAO56 single crop coefficient approach. The crop coefficient (K_c) varied during the growing season according to the maize phenological stage (Allen et al., 1998). As the simulations started 44 days after seeding, that is, the soil surface was almost fully covered, all the ET_c was assigned to transpiration and evaporation was consequently set equal to 0.

Groundwater level (GWL) data were weekly recorded at each monitoring site during the field experiment. GWL values in intermediate days were estimated by linear interpolation.

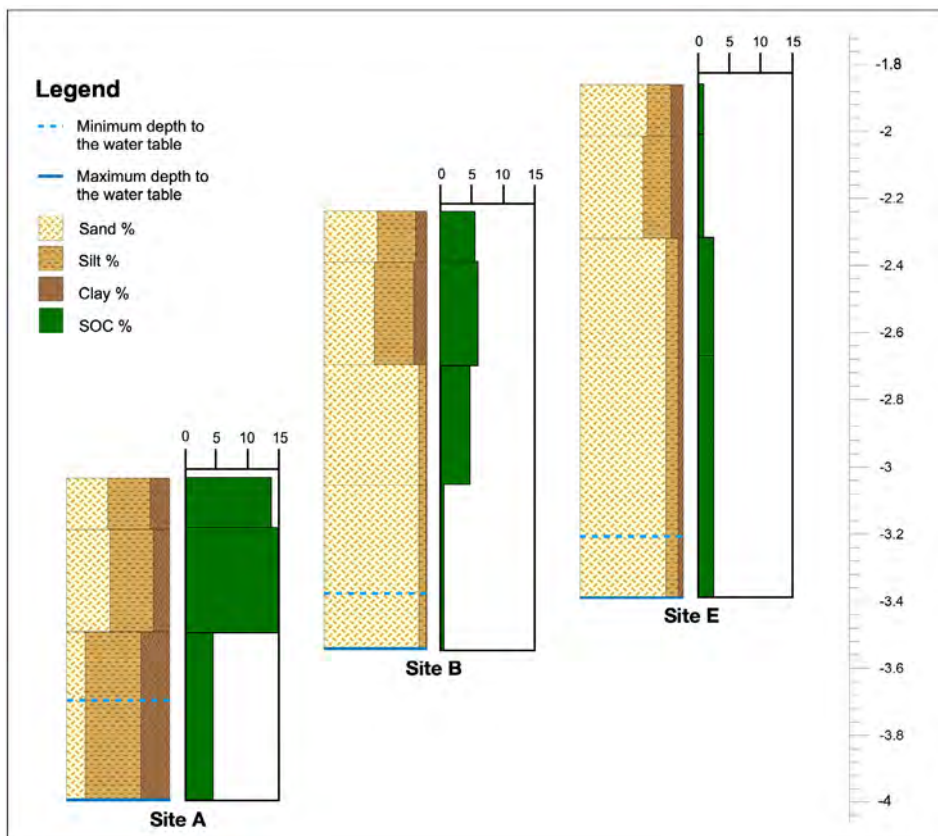


FIGURE 2 Soil profiles at monitoring sites A, B, and E referred to their elevation (m msl). Each block represents a soil layer as modelled in Hydrus-1D. Sand, silt, clay, and SOC percentages are represented in each block. The simulated domain is set equal to the maximum depth to the water table, which is represented by the blue continuous line. The dashed line represents the minimum depth to the water table recorded during the monitoring period

2.4.2 | Field experiments

The capability of the ES algorithm in reducing the uncertainty on the VGM parameters was tested by assimilating the VWC observations collected at sites A, B, and E. The soil profile at the three monitoring sites is highly heterogeneous. The characteristics of each material (i.e., texture and SOC) are presented in Figure 2. Soil texture is mainly loam in the top layers, while sand content increases in layers 2 and 3 at sites B and E. Site A is characterized by the presence of peat (soil organic carbon and BD are 11.5% and 0.93 g cm⁻³ on average), while the mean BD is 1.5 g cm⁻³ at site E that was located inside the northwest sandy paleo-channel (Figure 1). Intermediate characteristics were observed at site B, where the mean SOC and BD were 4.8% and 1.2 g cm⁻³, respectively.

The domain thickness was set equal to the maximum depth to the water table observed at each site during the monitored time period (0.94 m in A, 1.28 m in B, and 1.5 m in E) and it was divided into four soil layers (0–0.16, 0.17–0.41, 0.42–0.61, and 0.62 m-max), each of them associated with one capacitance resistance probe installed at 0.1, 0.3, 0.5, and 0.7 m depths. As the fourth layer of site A was permanently submerged by the groundwater, only three layers were considered (Figure 2). All the profiles were spatially discretized by 0.01 m mesh size. The standard deviation of the measurement error associated with all VWC measurements used to populate the covariance matrix C_o was set equal to 0.03, which corresponds to the probe measurement accuracy.

Uniform probability distribution functions (PDFs) were used to model parameter uncertainty. PDFs were generated between the minimum and maximum values of θ_r , α , n , and K_s parameters (Table 1) chosen according to previous analyses on the study area (Bevington

et al., 2016). Then, 500 ensemble realizations were sampled from the prior PDFs to be part of the augmented forecast matrix A . The same maximum and minimum values used to generate the PDFs were used as limits for the LM parameter inversion (Table 1). The choice of a maximum θ_r equal to 0.4 at site A is due to the large percentage of organic matter and agrees with the value used by Dettmann et al. (2019) and with the findings of Menbreu et al. (2021).

As already underlined, the LM inversion algorithm implemented in Hydrus-1D is very sensitive to the initial parameter values, thus the minimization problem was repeated with five parameter combinations, four of which were sampled from the prior PDFs and one with the VGM parameters obtained by lab hydraulic analyses. θ_s values were fixed and derived from previous studies (Bevington et al., 2016). The five parameter sets and the fixed θ_s values are available in the Supplementary Materials.

To compare the results obtained with LM and ES, the same error covariance matrix was used for both methods. In the Hydrus-1D-implemented LM, the parameters were weighted by using the standard deviation (STD) of the prior parameter distribution functions, whose values are reported in Table 1.

3 | RESULTS

3.1 | Time-variable boundary conditions: Weather, ET, and groundwater level

The total rainfall from 5/17/2011 to 9/23/2011 amounted to 218 mm with 113 and 105 mm during the calibration and

TABLE 1 Maximum and minimum values of the VGM parameters used to generate the uniform PDFs for the ES and to limit the LM inversion

| | | θ_r (cm ³ cm ⁻³) | α (cm ⁻¹) | n (-) | K_s (cm day ⁻¹) |
|--------|-----|--|------------------------------|---------|-------------------------------|
| Site A | Min | 0.010 | 0.010 | 1.100 | 0.5 |
| | Max | 0.400 | 0.250 | 2.200 | 650.0 |
| | STD | 0.110 | 0.070 | 0.320 | 187.5 |
| Site B | Min | 0.001 | 0.010 | 1.100 | 0.5 |
| | Max | 0.100 | 0.150 | 2.000 | 600.0 |
| | STD | 0.030 | 0.040 | 0.260 | 173.1 |
| Site E | Min | 0.001 | 0.001 | 1.300 | 1.0 |
| | Max | 0.120 | 0.050 | 3.000 | 1000.0 |
| | STD | 0.030 | 0.010 | 0.490 | 288.4 |

Note: STDs are used as weights in the LM inversion.

TABLE 2 Average depth to the water table and elevation of the water table relative to the mean sea level (m msl) over the calibration and validation periods

| Site | Calibration depth (m) | Calibration elevation (m msl) | Validation depth (m) | Validation elevation (m msl) |
|--------|-----------------------|-------------------------------|----------------------|------------------------------|
| Site A | 0.73 | -3.76 | 0.89 | -3.92 |
| Site B | 1.16 | -3.41 | 1.23 | -3.48 |
| Site E | 1.38 | -3.26 | 1.46 | -3.34 |

validation periods, respectively. The cumulative ET_c was higher during calibration because of the maize growth stage (300 and 211 mm during the two periods, respectively). The three monitoring sites differed in the average depths to the water table which were

0.81, 1.20, and 1.42 m at sites A, B, and E, respectively. Table 2 shows a comparison of depth to the water table and water table elevation relative to the mean sea level between calibration and validation periods.

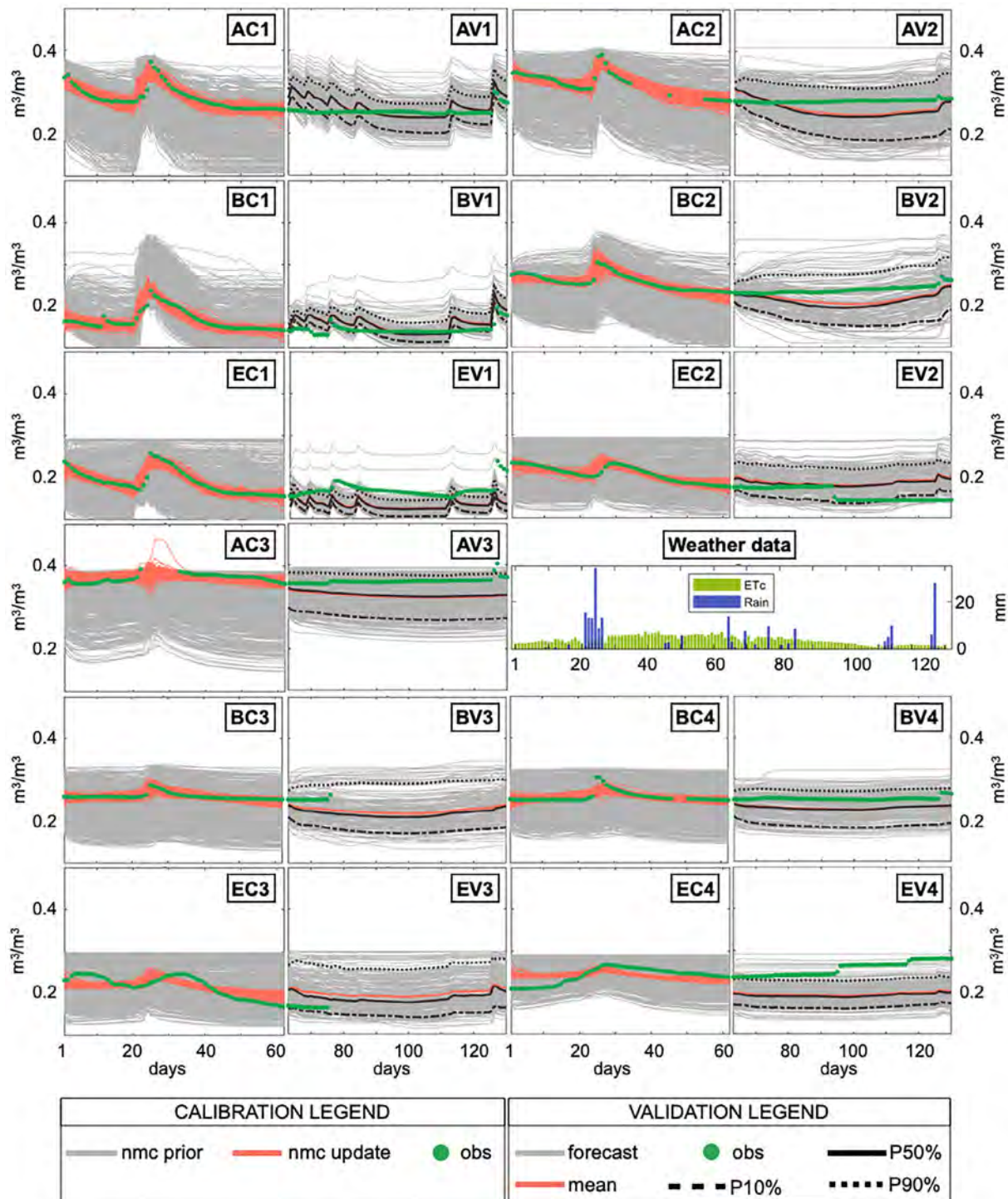


FIGURE 3 VWC versus time resulting from the ES application at each layer of sites A, B, and E. Each box represents the results of one site (A, B, E) during calibration or validation periods (C, V) at the four layers (1, 2, 3, 4). The calibration shows the prior ensemble of Monte Carlo simulations (nmc prior), the ensemble update (nmc update), and the observations (obs). The validation shows the Monte Carlo simulations obtained by running the hydrological model with the parameters sampled from the updated distributions (forecast), the mean, the 10th (P10%), 50th (P50%), and 90th (P90%) percentiles of those simulations, and the observations (obs). Notice that the mean can coincide with P50% and, consequently, is not clearly visible. The weather data chart shows daily rainfall and crop evapotranspiration (ET_c)

3.2 | ES outcomes

ES application to the field datasets was anticipated by a synthetic experiment to test its capability of reducing the prior uncertainty on the VGM parameters. The synthetic experiments were carried out using the setting developed for site A and assimilating (a) both pressure head and VWC observations, and (b) VWC observations only. The synthetic observations were generated by running Hydrus-1D with a 'true' set of hydraulic parameters. Note that when different measurement types were assimilated, a proper matrix scaling was performed (Evensen, 2003). The observation error was set equal to $\pm 15\%$ and $\pm 5\%$ for h and VWC, respectively. The ranges of the parameter uniform PDFs (θ_r , α , n , and K_s) from which the 500 realizations were sampled, the 'true' parameters used to generate the synthetic observations, and the results are provided in the Supplementary Materials.

The results of the two synthetic experiments were comparable in terms of uncertainty reduction, thus supporting the validity of the outcomes obtained with the real experiments where only VWC records are used.

Figure 3 shows the calibration and validation results on VWC state over time for the three sites. The parameter calibration improves water content estimates compared to the prior condition. At site A, almost all VWC observations are between the mean and the 90th percentile. The records seem unaffected by wetting and drying cycles caused by rainfall events and evapotranspiration possibly due to the presence of peat with high water holding capacity and the water table permanently close to the soil surface. The observations of all layers of site B were close to mean and median posterior realizations meaning that the smoother was able to find a parameter distribution that fitted both calibration and validation. On the contrary, the updated

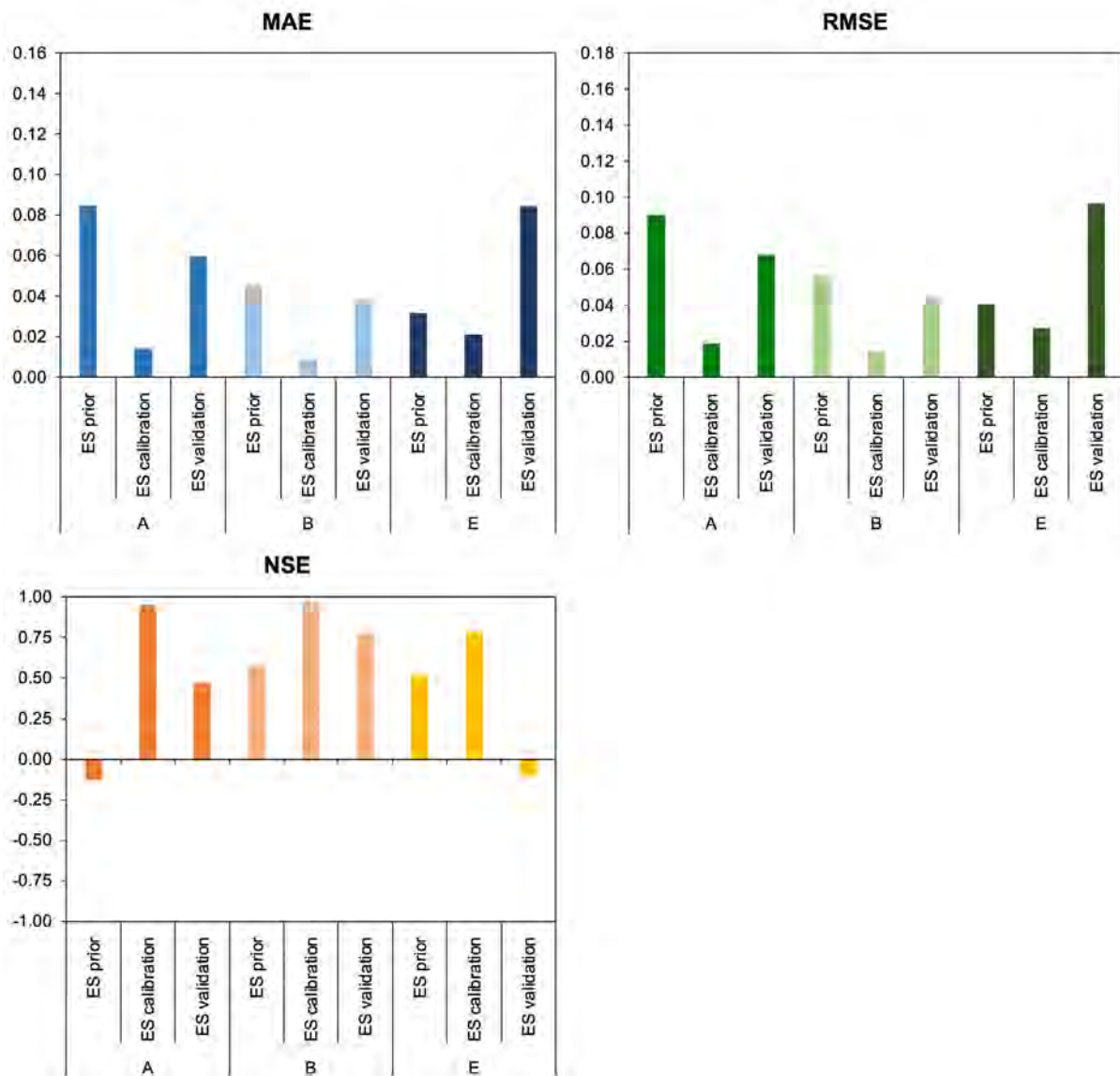


FIGURE 4 Performance parameters (MAE, RMSE, NSE) of the ES prior and ES update over the calibration and validation periods for the three monitoring sites

realizations are less able to capture the observations in site E, particularly at layers 1 and 4 where they are outside the 90th percentile.

The ES effect in reducing the parameter uncertainty was confirmed by the reduction of MAE and RMSE, and by the NSE close to 1 (Figure 4). Specifically, the update states matched the observations at sites A and B, while a consistent deviation can be noticed at the deepest layers of site E probably caused by the uncertainty on the boundary conditions. MAE, RMSE, and NSE indexes show a reduction in the modelling performance during the validation phase compared to the calibration (Figure 4). Additionally, the NSE of site E validation was lower than 0, meaning that the model demonstrated a negligible predictive skill.

The results of the assimilation in terms of prior and posterior parameter CDFs are summarized in Figure 5 for layer 1 of all monitoring sites, while layers 2–4 are available in the Supplementary Materials. A significant reduction in α uncertainty was obtained at all sites and depths. The same was found for n parameter, except in site E where the mean updated n was close to the prior mean at layers 1, 2, and 3. The posterior CDFs of θ_r were almost identical to the prior ones at sites B and E, while the uncertainty was reduced at site A where the updated means tend towards the upper limit. Finally, K_s uncertainty was consistently reduced at the upper layers of all sites, while the reduction in the spread of posterior CDFs was negligible at the lower layers.

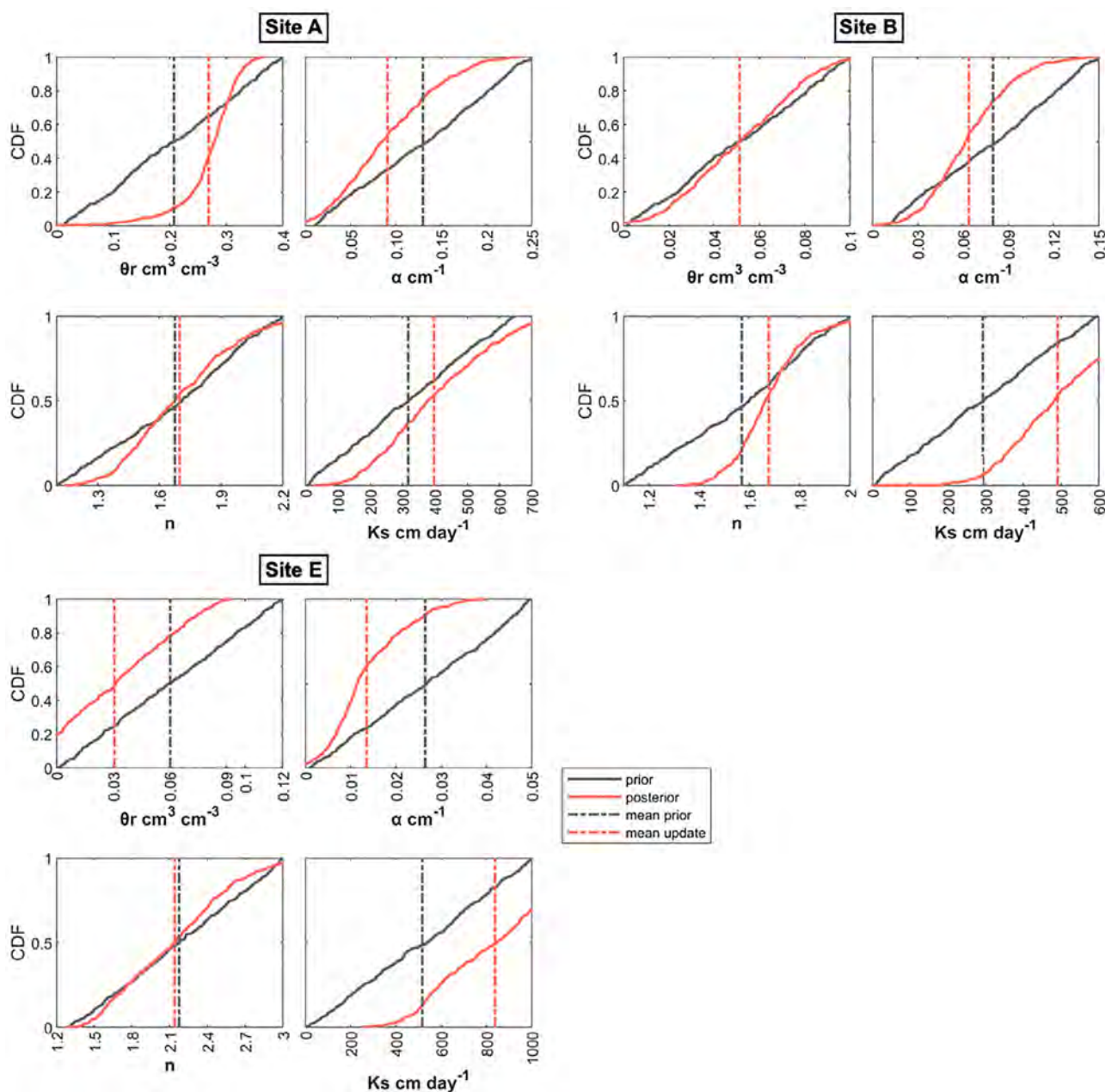


FIGURE 5 Prior and posterior cumulative distribution functions (CDFs) of VGM parameters at all layer 1 of all monitoring sites. The dashed black and red lines represent the mean of the prior (mean prior) and posterior (mean update) ensembles, respectively

3.3 | LM algorithm

Results of the LM inversion in terms of parameter calibration are presented in Table 3. As five inversions with different initial values were performed for each site, the one producing the lowest MAE between observations and model outcomes was considered. Figure 6 shows the behaviour of the experimental and simulated VWC versus time as obtained with the optimized parameters. The modelling outcome is in good agreement with observations over the calibration period for all sites except for layers 2 and 3 in site E where a shift between simulation and observations in the period from 6/5/2011 to 6/15/2011 is evident, similarly to the outcome obtained by the ES. During the validation, the calibrated models reproduce satisfactorily the experimental data although the experimental variability is not fully captured (e.g., in layer 1 of sites A and B the simulated VWC is more dynamic than observations). This was confirmed by the performance indexes calculated between observed and modelled data that demonstrated a greater modelling performance during the calibration (Figure 7).

3.4 | Soil-water retention curves (SWRCs)

The soil-water retention curves (SWRCs) obtained by the ES prior and updated parameters, the LM inversion calibration, and the lab analyses are shown in Figure 8. The SWRCs derived from the field data using the two inverse modelling techniques differ from those measured in the laboratory. This is particularly noticeable in the upper layers in all the three sites, with the lab curves wetter than those obtained by model calibration on the field data, that is, higher moisture content at the same capillary pressure, particularly approaching θ_r . In general, the curves obtained by the LM inversion are always inside the ES posterior ensemble. A better agreement between lab and inverse methods

is obtained in layer 3 at site A, layers 3 and 4 at site B, and layer 4 at site E.

4 | DISCUSSION

In this study, the ability of the Ensemble Smoother algorithm and the Levenberg–Marquardt inversion algorithm implemented in Hydrus-1D to reduce the uncertainty of VGM parameters was tested under real field conditions in three experimental locations (sites A, B, and E) located at the southern boundary of the Venice Lagoon. The low-lying experimental area is characterized by a very shallow water table, peat deposits (site A), sandy drifts (site E), and strong changes in the soil properties with depth (site B).

The peculiarity of the farmland, with a very shallow water table strongly controlled by drainage infrastructures and independent of climatic conditions and crop states, precludes significant variations of the water content over time, generally penalizing the performance of inversion methods to derive VGM parameters from VWC observations. The three tests demonstrated that the ES method approximates fairly well the water content state during the calibration, while the performance indexes show a lower efficiency during the validation, especially in site E. A satisfactory improvement was obtained at sites B and A, suggesting the suitability of the ES algorithm in reducing the uncertainty of water content state in peaty soils. At site E, despite the NSE of the calibration period was 0.78, it became negative in the validation period. This can be explained by the higher sand content of site E that increases the non-linearities of the system. Difficulties in calibrating sandy layers were also found by Li and Ren (2011) using the EnKF. Moreover, many authors stated that the efficiency of the ES typically decreases when the states are nonlinear functions of the parameters (Li et al., 2015; van Leeuwen & Evensen, 1996). To handle

TABLE 3 Initial and optimized parameters obtained by the LM inverse method implemented in Hydrus-1D

| | | θ_r (cm ³ cm ⁻³) | α (cm ⁻¹) | n (-) | K_s (cm day ⁻¹) |
|--------|---------|--|------------------------------|---------|-------------------------------|
| Site A | Initial | 0.252 | 0.029 | 1.467 | 54.5 |
| | Layer 1 | 0.318 | 0.050 | 1.709 | 445.9 |
| | Layer 2 | 0.106 | 0.036 | 1.478 | 10.8 |
| | Layer 3 | 0.231 | 0.091 | 1.122 | 377.3 |
| Site B | Initial | 0.026 | 0.122 | 1.856 | 411.8 |
| | Layer 1 | 0.074 | 0.080 | 1.591 | 565.2 |
| | Layer 2 | 0.087 | 0.057 | 1.357 | 354.3 |
| | Layer 3 | 0.058 | 0.070 | 1.288 | 400.6 |
| | Layer 4 | 0.041 | 0.070 | 1.370 | 173.8 |
| Site E | Initial | 0.113 | 0.039 | 1.810 | 170.4 |
| | Layer 1 | 0.113 | 0.009 | 2.453 | 570.0 |
| | Layer 2 | 0.120 | 0.026 | 1.474 | 746.0 |
| | Layer 3 | 0.046 | 0.024 | 1.304 | 660.0 |
| | Layer 4 | 0.115 | 0.012 | 2.853 | 1.0 |

Note: Among the five calibrations performed, the one with the lowest MAE between observation and model outcome was accepted as final result.

the stronger non-linear SWRCs typical of coarse soils, future work will be aimed at the application of an extended version of the ES, for example, the Ensemble Smoother with Multiple Data Assimilation (Emerick & Reynolds, 2013), in which the same data are iteratively assimilated multiple times. This method was recently applied by Cui et al. (2020) to estimate hydraulic parameters on synthetic tests and was demonstrated to be promising in handling strong non-linear problems.

The ES algorithm was only partially effective in reducing the uncertainty of VGM parameters. In agreement with the results by Li

and Ren (2011), the assimilation only partially constrains θ_r parameter. At site B, the shift of the mean update is negligible, while good results were obtained at the upper layers of site E and at site A (layers 1 and 2). Moreover, considerable uncertainty remains on K_s in agreement with the results by Valdes-Abellan et al. (2018) and Medina et al. (2014). The latter also found that K_s identifiability can be compromised by the limited variability of the assimilated observations as well as by the correlation between parameters. On the contrary, satisfactory results are obtained for α and n parameters (Figure 5, Supplementary Materials). In agreement with the outcomes obtained on VWC

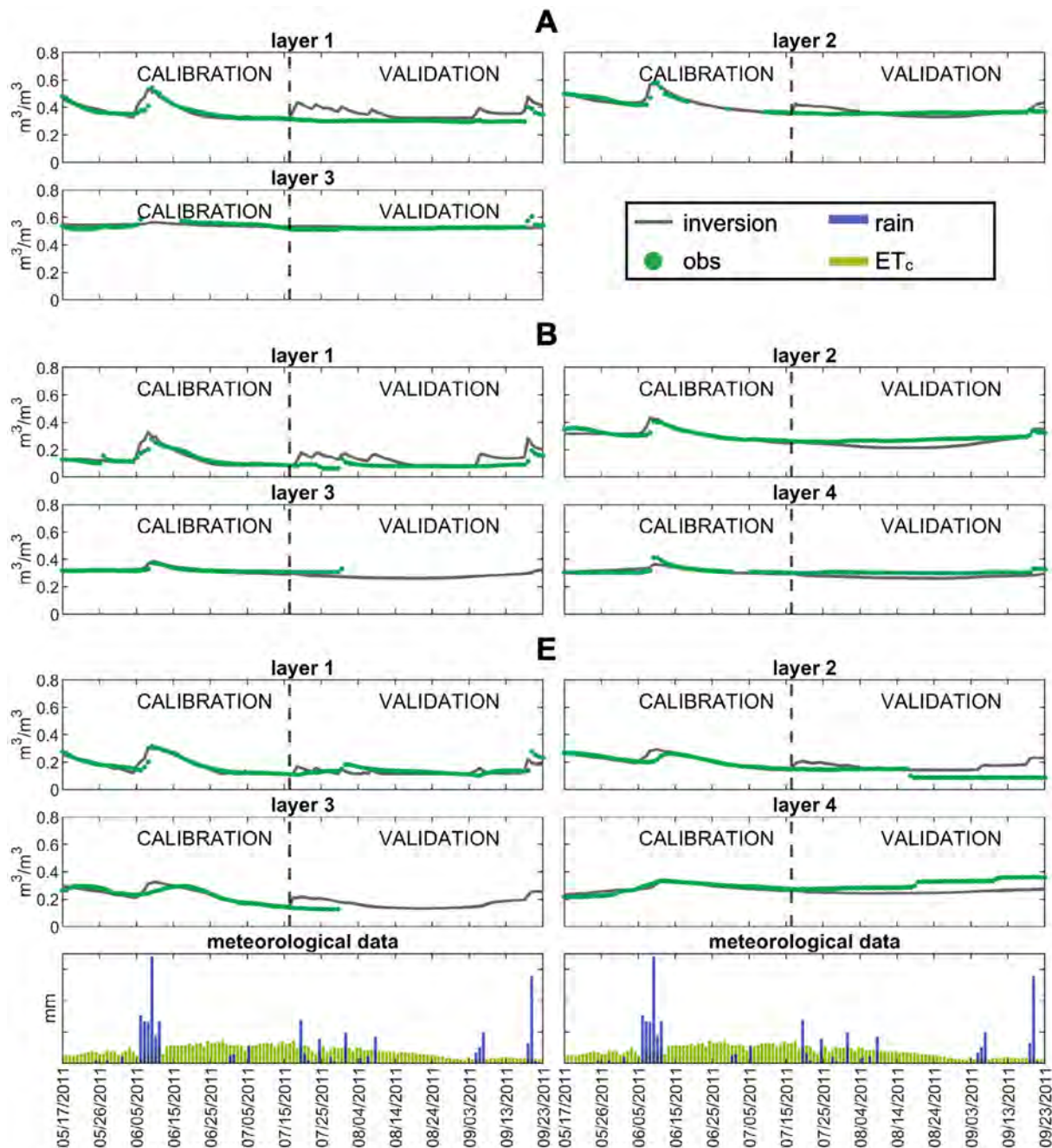


FIGURE 6 Model outcome for sites A, B and E as obtained by running Hydrus-1D with the parameters achieved by the LM inversion algorithm versus field observations (obs). The LM inversion was performed using the observations over the calibration period. The resulting parameters were then used to run the model during the validation phase. The two bottom charts provide rainfall and crop evapotranspiration ET_c

state, the results on VGM parameters suggested a good efficiency of the ES method applied on peaty soils. The results obtained at site A agree with the findings of Menbreu et al. (2021) that applied the Van Genuchten water retention model to several peat types.

LM algorithm implemented in Hydrus-1D demonstrates a good efficiency in terms of VWC prediction as confirmed by the performance indexes (Figure 7). In contrast to the ES, the LM does not show the same limitations in the sandy site E. However, as confirmed by many authors, LM local optimization algorithm is very sensitive to the initial parameters (Simunek et al., 2012; Vrucht et al., 2008; Wholing et al., 2008). For example, when using laboratory parameters as initial values instead of the distribution means, the LM result widely differs. It must be highlighted that the process of manual calibration is time-

consuming, particularly when the process is repeated with several sets of initial parameters. On the other hand, the ES allows the calibration of state and parameters of all layers simultaneously giving satisfactory results.

Despite the difficulties of laboratory-scale measurements to precisely characterize the soil hydraulic properties at the field scale (Valdes-Abellan et al., 2018; Vrucht et al., 2008), the analyses performed on undisturbed soil samples turned very useful to determine the limits of the prior parameter distributions. Moreover, the comparison between the laboratory SWRCs with those derived by the LM inversion and ES shows that, in the present hydrogeological setting, the lab analyses can provide useful information on the wetter part of the curve, particularly for the upper soil layer where, although the

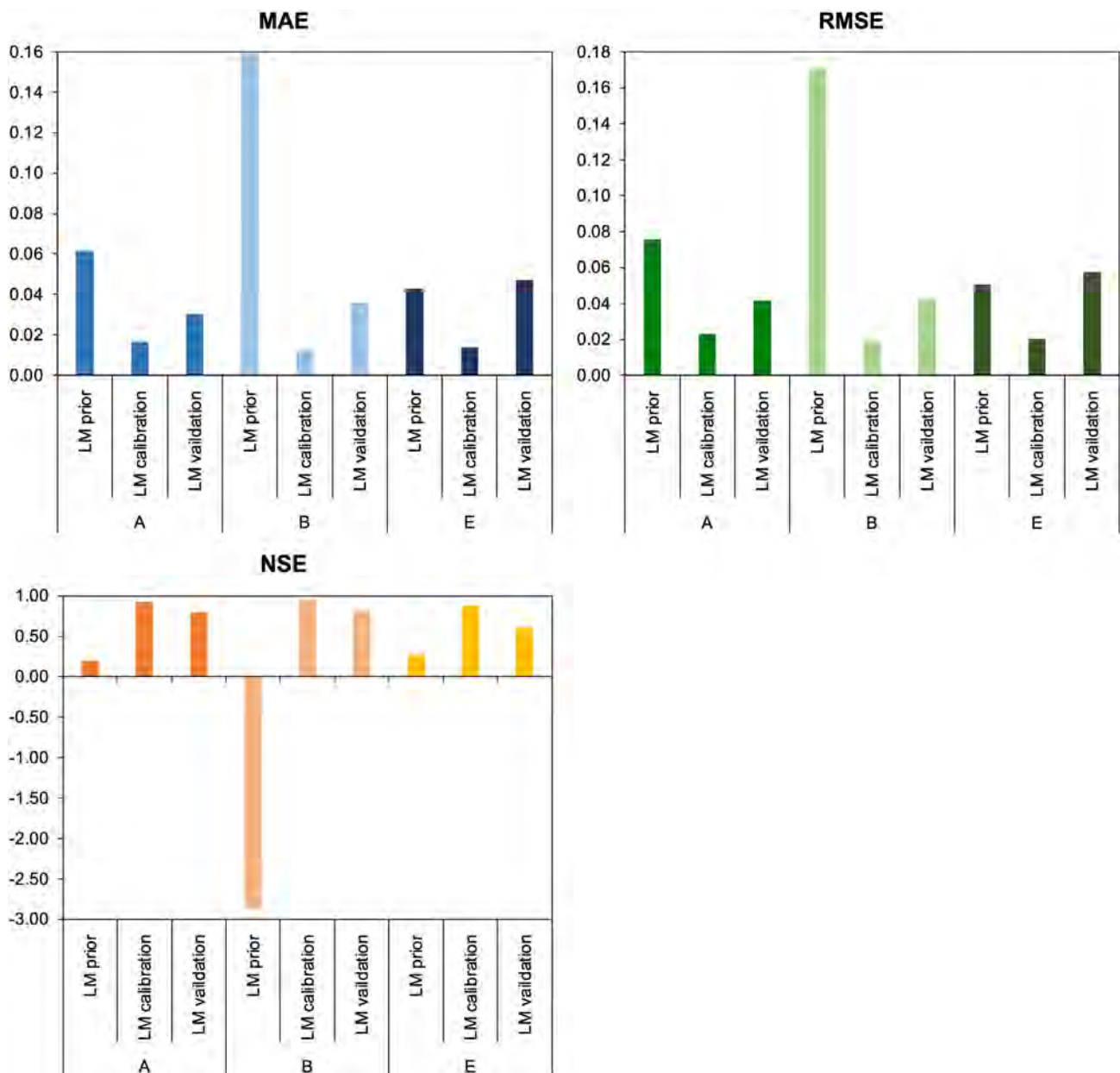


FIGURE 7 Performance parameters (MAE, RMSE, NSE) calculated between observed and modelled data before the calibration (prior) and after the LM inversion implemented in Hydrus-1D for both calibration and validation periods in the three monitoring sites

shallow water table, the saturation is almost never reached in field conditions due to the efficient drainage system. The lab SWRCs show higher moisture content at the same matric potential compared to LM and ES ones. Several reasons can be responsible for that difference: (i) the different scale of investigation between lab testing and the field observations, with the former that is only partially representative of the latter; (ii) the upper soil layers that never reach saturation in field conditions, while the lab samples were artificially saturated for the

analysis. Thus, as field measurements near the saturation range were not available, the calibration on field data gave results different from those obtained from lab calibration; (iii) the hysteresis that causes the water content along the drying curve to be larger than that along the wetting curve. While the lab curve is a drying curve, field data reflected both drying and wetting events.

Finally, in the context of the present study we point out that the ES could be used to deal also with other uncertainties, for example,

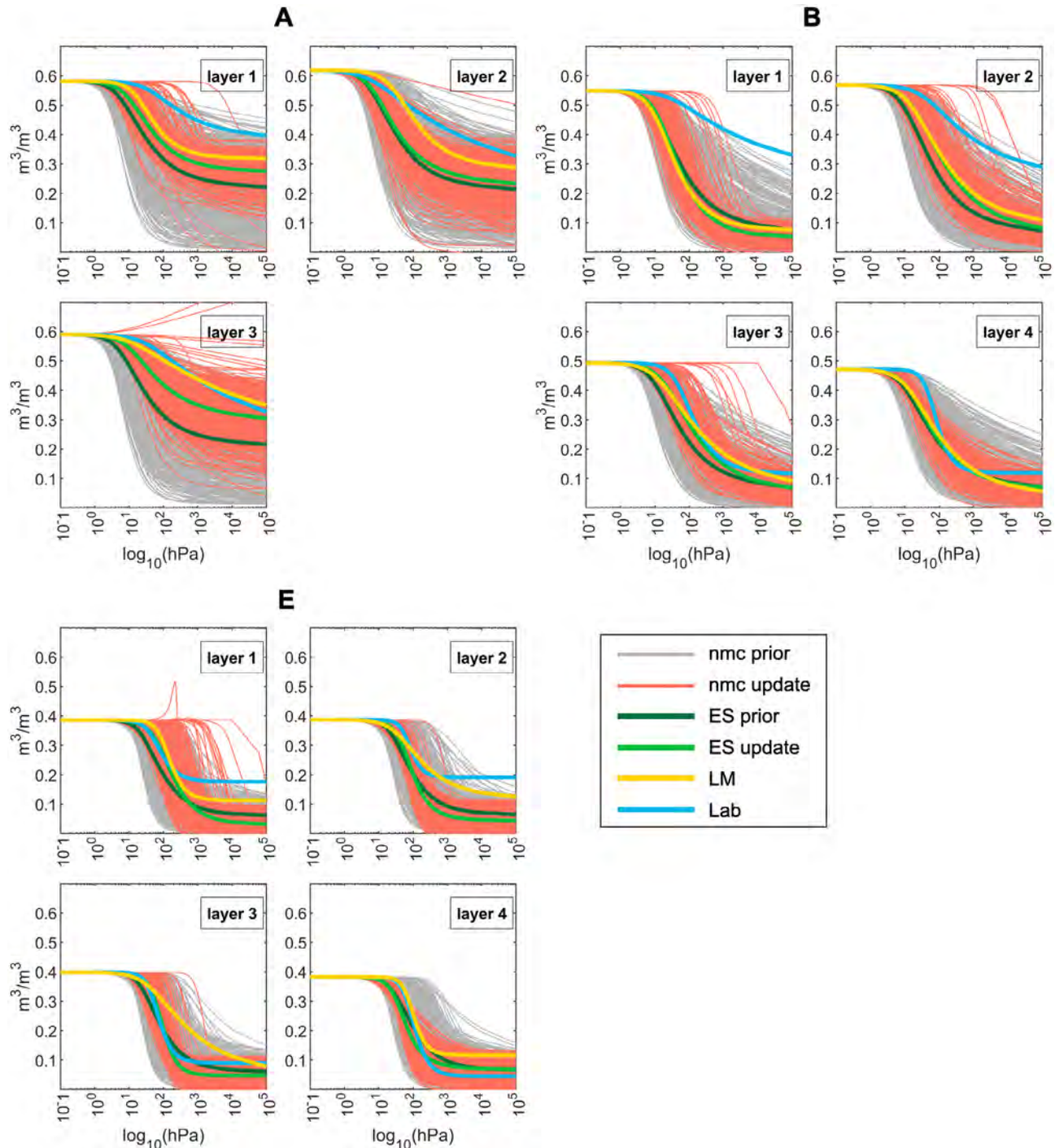


FIGURE 8 Soil-water retention curves obtained for the three monitoring sites with the prior (nmc prior) and the update (nmc update) ensemble parameters, their mean values (ES prior and ES update), the LM inversion algorithm (LM), and the laboratory parameters (lab)

those related to boundary conditions. Accurate estimates of crop evapotranspiration are fundamental to understand the hydrological dynamics in agricultural fields. In this work, the FAO method (Allen et al., 1998) was applied to calculate the maximum crop evapotranspiration (ET_c) that is the evapotranspiration under ideal conditions without considering spatial variability and crop stress. This approach could be improved by introducing an error in the boundary condition or by assimilating the actual crop evapotranspiration (ET_a) that reflects the real response of crop to stress (e.g., water and salt stress) and can be estimated, for example, from remotely sensed images. Its assimilation together with soil moisture data may improve the estimation of hydrological model states and parameters.

5 | CONCLUSIONS

The identification of vadose zone hydraulic properties in real field conditions is fundamental to efficiently manage the water resources, particularly in agricultural lands. With the aim of testing the ES and LM algorithm performances in reducing the uncertainty of the VGM parameters, three real tests were carried out which consisted on the assimilation of VWC observations collected in a highly heterogeneous agricultural field.

The use of the ES approach demonstrated the following advantages: (i) the simultaneous calibration of the VGM parameters (θ , α , n , and K_s) of all layers allows a strong reduction in the calibration time if compared with that required for the application of the LM inversion algorithm implemented in Hydrus-1D; (ii) the Bayesian approach reduces parameters uncertainty starting from several realizations randomly sampled from defined distributions. On the other hand, local search methodologies require an initial set of parameters and find a unique solution without uncertainty estimation and with a strong sensitivity to the starting point in the parameter space; (iii) the data assimilation approach demonstrated a greater efficiency in the peat soil for both parameters and state calibration; (iv) in addition to parameter calibration, the ES application allowed the quantification of SWRCs uncertainty; (v) data assimilation approaches can account for multiple uncertainties (e.g., on states, parameters, boundary, and forcing conditions) and this is fundamental when studying the hydraulic characteristics of soils in field conditions.

The comparison between ES SWRCs with those obtained in the lab and applying the LM inverse method implemented in Hydrus-1D highlights that in the shallowest layers the lab curves were wetter compared to the others. This was probably caused by scale discrepancies, hysteresis effects, the lack of field measurements near the saturation, or an insufficient range of matric heads used in the lab experiment. Despite the issues related to lab measurements, the prior knowledge on parameters was useful for the definition of parameter ranges.

Future works will focus on implementing multiple data assimilation algorithms (e.g., MDA) to overcome the issues related to the strong non-linearities of SWRCs, particularly in coarser soils.

Moreover, the application of data assimilation methods to reduce the uncertainty of VGM parameters in agricultural areas may be further improved by introducing additional uncertainties (e.g., in boundary conditions) or by assimilating additional measurements such as ET_a .

ACKNOWLEDGEMENTS

This research was funded by the contribution from the EU co-financing and the Interreg Italy–Croatia Cross Border Collaboration (CBC) Programme 2014–2020 (Priority Axes: Safety and Resilience) through the European Regional Development Fund as a part of the projects ‘Monitoring sea-water intrusion in coastal aquifers and testing pilot projects for its mitigation’ (MoST, AID: 10047742) and ‘Salt-water intrusion and climate change: monitoring, countermeasures and informed governance’ (SeCure, AID: 10419304).

DATA AVAILABILITY STATEMENT

Data and scripts used for this study are available from the corresponding author upon reasonable request.

ORCID

Ester Zancanaro  <https://orcid.org/0000-0002-4930-7287>

REFERENCES

- Abbasi, F., Feyen, J., & van Genuchten, M. T. (2004). Two-dimensional simulation of water flow and solute transport below furrows: Model calibration and validation. *Journal of Hydrology*, 290, 63–79.
- Abbasi, F., Jacques, D., Simunek, J., Feyen, J., & van Genuchten, M. T. (2003). Inverse estimation of soil hydraulic properties and solute transport parameters from transient field experiments: Heterogeneous soil. *Transactions of ASAE*, 46(4), 1097–1111.
- Abbasi, F., Jacques, D., Simunek, J., Feyen, J., van Genuchten, M. T., & Shouse, P. (2003). Simultaneous inverse estimation of soil hydraulic properties and solute transport parameters from transient field experiment. *Transactions of ASAE*, 46(4), 1085–1095.
- Allen, R. G., Pereira, L. S., Raes, D., & Smith, M. (1998). *Crop evapotranspiration. Guidelines for computing crop water requirements*; FAO irrigation and drainage paper no. 56. FAO.
- Alletto, L., Pot, V., Giuliano, S., Costes, M., Perdrioux, F., & Justes, E. (2015). Temporal variation in soil physical properties improves the water dynamics modeling in a conventionally-tilled soil. *Geoderma*, 243–244, 18–28.
- Bailey, R., & Baù, D. (2010). Ensemble smoother assimilation of hydraulic head and return flow data to estimate hydraulic conductivity. *Water Resources Research*, 46, W12543.
- Bevington, J., Piragnolo, D., Teatini, P., Vellidis, G., & Morari, F. (2016). On the spatial variability of soil hydraulic properties in a Holocene coastal farmland. *Geoderma*, 262, 294–305.
- Bevington, J., Scudiero, E., Teatini, P., Vellidis, G., & Morari, F. (2019). Factorial kriging analysis leverages soil physical properties and exhaustive data to predict distinguished zones of hydraulic properties. *Computers and Electronics in Agriculture*, 156, 426–438.
- Botto, A., Bellucco, E., & Camporese, M. (2018). Multi-source data assimilation for physically based hydrological modeling of an experimental hillslope. *Hydrology and Earth System Sciences*, 22, 4251–4266.
- Brandhorst, N., Erdal, D., & Neuweiler, I. (2017). Soil moisture prediction with ensemble Kalman filter: Handling uncertainty of soil hydraulic parameters. *Advances in Water Resources*, 110, 360–370.
- Brunetti, G., Simunek, J., & Piro, P. (2016). A comprehensive numerical analysis of the hydraulic behavior of a permeable pavement. *Journal of Hydrology*, 540, 1146–1161.

- Brunetti, G., Stumpp, C., & Simunek, J. (2022). Balancing exploitation and exploration: A novel hybrid-global optimization strategy for hydrological model calibration. *Environmental Modelling and Software*, 150(105341), 105341.
- Cao, Y., Zhang, H., Li, W., Zhou, M., Zhang, Y., & Chaovaitwongse, W. A. (2019). Comprehensive learning particle swarm optimization algorithm with local search for multimodal functions. *IEE Transactions on Evolutionary Computation*, 23(4), 718–731.
- Crestani, E., Camporese, M., Baú, D., & Salandin, P. (2013). Ensemble Kalman filter versus ensemble smoother for assessing hydraulic conductivity via tracer test data assimilation. *Hydrology and Earth System Sciences*, 17, 1517–1531.
- Cui, F., Bao, J., Cao, Z., Li, L., & Zheng, Q. (2020). Soil hydraulic parameters estimation using ground penetrating radar data via ensemble smoother with multiple data assimilation. *Journal of Hydrology*, 583, 124552.
- Dal Ferro, N., Sartori, L., Simonetti, G., Berti, A., & Morari, F. (2014). Soil macro- and microstructures as affected by different tillage systems and their effects on maize root growth. *Soil and Tillage Research*, 140, 55–65.
- Dane, T., & Topp, G. (Eds.). (2002). *SSSA book series no. 5, methods of soil analysis, part 4: Physical methods*. Soil Science Society of America.
- Dettmann, U., Bechtold, M., Viohl, T., Piayda, A., & Sokolowsky, L. (2019). Evaporation experiments for the determination of hydraulic properties of peat and other organic soils: An evaluation of methods based on a large dataset. *Journal of Hydrology*, 575, 933–944.
- Emerick, A. A., & Reynolds, A. C. (2013). Ensemble smoother with multiple data assimilation. *Computers and Geosciences*, 55, 3–15.
- Evensen, G. (1994). Sequential data assimilation with a nonlinear quasi-geostrophic model using Monte Carlo methods to forecast error statistics. *Journal of Geophysical Research*, 99(C5), 10143–10162.
- Evensen, G. (2003). The ensemble Kalman filter: Theoretical formulation and practical implementation. *Ocean Dynamics*, 53, 343–367.
- Evensen, G. (2009). *Data assimilation. The ensemble Kalman filter* (2nd ed.). Springer.
- FAO-UNESCO. (1989). *Soil map of the world, revised legend*. Food and Agriculture Organization of the United Nations.
- Feddes, R. A., Kowalik, P. J., & Zaradny, H. (1978). *Simulation of field water use and crop yield*. John Wiley & Sons.
- Gao, H., Zhang, J., Liu, C., Man, J., Chen, C., Wu, L., & Zeng, L. (2019). Efficient Bayesian inverse modeling of water infiltration in layered soils. *Vadose Zone Journal*, 18, 190029.
- Hoffman, G. J., & van Genuchten, M. T. (1983). Soil properties and efficient water use: Water management for salinity control. In H. M. Taylor, W. R. Jordan, & T. R. Sinclair (Eds.), *Limitations and efficient water use in crop production* (pp. 73–85). Am. Soc. of Agron.
- Hopmans, J. M., Simunek, J., Romano, N., & Durner, W. (2002). Inverse methods. In J. H. Dane & G. C. Topp (Eds.), *Methods of soil analysis, part 4: Physical methods*. Soil Science Society of America.
- Jacques, D., Simunek, J., Timmerman, A., & Feyen, J. (2002). Calibration of Richards' and convection-dispersion equations to field-scale water flow and solute transport under rainfall conditions. *Journal of Hydrology*, 259, 15–31.
- Jiang, Z., Huang, Q., Li, G., & Li, G. (2019). Parameters estimation and prediction of water movement and solute transport in layered, variably saturated soils using the ensemble Kalman filter. *Water*, 11, 1520.
- Kechavarzi, C., Dawson, Q., & Leeds-Harrison, P. B. (2010). Physical properties of low-lying agricultural peat soils in England. *Geoderma*, 154, 196–202.
- Li, C., & Ren, L. (2011). Estimation of unsaturated soil hydraulic parameters using the ensemble Kalman filter. *Vadose Zone Journal*, 10, 1205–1227.
- Li, N., McLaughlin, D., Kinzelbach, W., Li, W., & Dong, X. (2015). Using an ensemble smoother to evaluate parameter uncertainty of an integrated hydrological model of Yanqui basin. *Journal of Hydrology*, 529, 146–158.
- Marquardt, D. W. (1963). An algorithm for least-squares estimation of nonlinear parameters. *Journal of the Society for Industrial and Applied Mathematics*, 11, 431–441.
- Medina, H., Romano, N., & Chirico, G. B. (2014). Kalman filters for assimilating near-surface observations into Richards' equation – Part 2: A dual filter approach for simultaneous retrieval of states and parameters. *Hydrology and Earth System Sciences*, 18, 2521–2541.
- Menbreu, M. W., Marttila, H., Ronkanen, A.-K., Haghghi, A. T., & Kløve, B. (2021). Hydraulic and physical properties of managed and intact peatlands: Application of the Van Genuchten-Mualem models to peat soils. *Water Resources Research*, 57, e2020WR028624.
- Moradkhani, H., Sorooshian, S., Gupta, H. V., & Houser, P. R. (2005). Dual state-parameter estimation of hydrological models using ensemble Kalman filter. *Advances in Water Resources*, 28, 135–147.
- Moriasi, D. N., Arnold, J. G., Van Liew, M. V., Bingner, R. L., Harmel, L. D., & Veith, T. L. (2007). Model evaluation guidelines for systematic quantification of accuracy in watershed simulations. *Transactions of the ASABE*, 50(3), 885–900.
- Mualem, Y. (1976). A new model for predicting the hydraulic conductivity of unsaturated porous media. *Water Resources Research*, 12, 513–522.
- Narenda, N. D., & Mohanty, B. P. (2006). Root zone soil moisture Assessment using remote sensing and vadose zone modeling. *Vadose Zone Journal*, 5, 296–307.
- Nash, J. E., & Sutcliffe, J. V. (1970). River flow forecasting through conceptual models part I – A discussion of principles. *Journal of Hydrology*, 3, 282–290.
- Qu, W., Bogena, H. R., Hulsman, J. A., Martinez, G., Pachepsky, Y. A., & Vereecken, H. (2014). Effects of soil hydraulic properties on the spatial variability of soil water content: Evidence from sensor network data and inverse modeling. *Vadose Zone Journal*, 13(12), 1–12.
- Radcliffe, D. E., & Simunek, J. (2010). *Soil physics with Hydrus: Modeling and applications*. CRC Press, Taylor & Francis Group.
- Ramos, T. B., Goncalves, M. C., Martins, J. C., van Genuchten, M. T., & Pires, F. P. (2006). Estimation of soil hydraulic properties from numerical inversion of tension disk infiltrometer data. *Vadose Zone Journal*, 5, 684–696.
- Rasmussen, J., Madsen, H., Jensen, K. H., & Refsgaard, J. C. (2015). Data assimilation in integrated hydrological modeling using ensemble Kalman filtering: Evaluating the effect of ensemble size and localization on filter performance. *Hydrology and Earth System Sciences*, 19, 2999–3013.
- Rezanezhad, F., Price, J. S., Quinton, W. L., Lennartz, B., Milojevic, T., & Van Cappelen, P. (2016). Structure of peat soils and implications for water storage, flow and solute transport: A review update for geochemists. *Chemical Geology*, 429, 75–84.
- Schwärzel, K., Renger, M., Sauerbrey, R., & Wessolek, G. (2002). Soil physical characteristics of peat soils. *Journal of Plant Nutrition and Soil Science*, 165, 479–486.
- Scudiero, E., Berti, A., Teatini, P., & Morari, F. (2012). Simultaneous monitoring of soil water content and salinity with a low-cost capacitance-resistance probe. *Sensors*, 12, 17588–17607.
- Scudiero, E., Teatini, P., Corwin, D. L., Deiana, R., Berti, A., & Morari, F. (2013). Delineation of site-specific management units in a saline region at the Venice lagoon margin, Italy, using soil reflectance and apparent electrical conductivity. *Computers and Electronics in Agriculture*, 99, 54–64.
- Shi, L., Song, X., Tong, J., Zhu, Y., & Zhang, Q. (2015). Impacts of different types of measurements on estimating unsaturated flow parameters. *Journal of Hydrology*, 524, 549–561.
- Simunek, J., & Hopmans, J. W. (2002). Parameter optimization and nonlinear fitting. In J. H. Dane & G. C. Topp (Eds.), *Methods of soil analysis, part 4: Physical methods*. Soil Science Society of America.
- Simunek, J., Sejna, M., Saito, H., Sakai, M., & van Genuchten, M. T. (2015). *The HYDRUS-1D software package for simulating the one-dimensional movement of water, heat, and multiple solutes in variably-saturated*

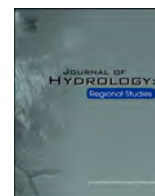
- media*, version 4.17. Department of Environmental Sciences, University of California Riverside.
- Simunek, J., van Genuchten, M. T., & Sejna, M. (2012). Hydrus: Model use, calibration, and validation. *Transactions of the ASABE*, 55(4), 1261–1274.
- Skjervheim, J. A., Evensen, J., Hove, J., & Vabø, J. G. (2011). An ensemble smoother for assisted history matching. In *Reservoir simulation symposium*. Society of Petroleum Engineers Inc..
- Song, X., Shi, L., Ye, M., Yang, J., & Navon, I. M. (2014). Numerical comparison of iterative ensemble Kalman filters for unsaturated flow inverse modeling. *Vadose Zone Journal*, 13(2), 1–12.
- Valdes-Abellan, J., Pachepsky, Y., & Martinez, G. (2018). Obtaining soil hydraulic parameters from soil water content data assimilation under different climatic/soil conditions. *Catena*, 163, 311–320.
- Vamerali, T., Bertocco, M., & Sartori, L. (2006). Effects of a new wide-sweep opener for no-till planter on seed zone properties and root establishment in maize (*Zea mays*, L.): A comparison with double-disk opener. *Soil and Tillage Research*, 89(2), 196–209.
- van Genuchten, M. T. (1980). A closed-form equation for predicting the hydraulic conductivity of unsaturated soils. *Soil Science Society of America Journal*, 44, 892–898.
- van Leeuwen, P. J. (2001). An ensemble smoother with error estimates. *Monthly Weather Review*, 129(4), 709–728.
- van Leeuwen, P. J., & Evensen, G. (1996). Data assimilation and inverse methods in terms of a probabilistic formulation. *Monthly Weather Review*, 124, 2898–2913.
- Vrugt, J. A., Robinson, B. A., & Vesselinov, V. V. (2005). Improved inverse modeling for flow and transport in subsurface media: Combined parameter and state estimation. *Geophysical Research Letters*, 32, L18408.
- Vrugt, J. A., Stauffer, P. H., Wohling, T., Robinson, B. A., & Vesselinov, V. V. (2008). Inverse modeling of subsurface flow and transport properties: A review with new developments. *Vadose Zone Journal*, 7, 843–864.
- Wesseling, J. G., Elbers, J. A., Kabat, P., & van den Broek, B. J. (1991). SWATRE: Instructions for input. Internal note. Winand Staring Centre.
- Wholing, T., Vrugt, J., & Barkle, G. (2008). Comparison of three multiobjective optimization algorithms for inverse modeling of vadose zone hydraulic properties. *Soil Science Society of America Journal*, 72(2), 305–319.
- Wosten, J. H. M., & van Genuchten, M. T. (1988). Using texture and other soil properties to predict the unsaturated soil hydraulic functions. *Soil Science Society of America Journal*, 52, 1762–1770.
- Zha, Y., Zhu, P., Zhang, Q., Mao, W., & Shi, L. (2019). Investigation of data assimilation methods for soil parameter estimation with different types of data. *Vadose Zone Journal*, 18, 190013.
- Zhang, D., Madsen, H., Ridler, M. E., Kidmose, J., Jensen, K. H., & Refsgaard, J. C. (2016). Multivariate hydrological data assimilation of soil moisture and groundwater head. *Hydrology and Earth System Sciences*, 20, 4341–4357.

SUPPORTING INFORMATION

Additional supporting information can be found online in the Supporting Information section at the end of this article.

How to cite this article: Zancanaro, E., Zoccarato, C., Morari, F., & Teatini, P. (2023). Estimation of hydraulic parameters in a heterogeneous low-lying farmland near Venice. *Hydrological Processes*, 37(1), e14791. <https://doi.org/10.1002/hyp.14791>

- Ivan Lovrinović I., Srzić V., & Aljinović I. (2023). Characterization of seawater intrusion dynamics under the influence of hydro-meteorological conditions, tidal oscillations and melioration system operative regimes to groundwater in Neretva valley coastal aquifer system, *Journal of Hydrology: Regional Studies*, 46, 101363, doi:10.1016/j.ejrh.2023.101363, 2023.



Characterization of seawater intrusion dynamics under the influence of hydro-meteorological conditions, tidal oscillations and melioration system operative regimes to groundwater in Neretva valley coastal aquifer system

Ivan Lovrinović^{a,*}, Veljko Srzić^b, Iva Aljinović^b

^a Department of Hydromechanics and Hydraulics, Faculty of Civil Engineering, Architecture and Geodesy, University of Split, Matice hrvatske 15, 21000 Split, Croatia

^b Department of Water Resources, Faculty of Civil Engineering, Architecture and Geodesy, University of Split, Matice hrvatske 15, 21000 Split, Croatia

ARTICLE INFO

Keywords:

River Neretva coastal system
Seawater intrusion
Groundwater dynamics
Coherence
Spectrogram

ABSTRACT

Study region: River Neretva coastal aquifer system located in the south eastern part of Croatia.

Study focus: The study is focused to determination of the seasonal and non-seasonal variations of the groundwater features, when influenced by external loadings found at the study area. Based on time series observed from the monitoring systems, in-situ profiling and observed external loadings, a spectrogram and coherence analysis is performed to detect the peculiarities of the groundwater regimes at three different subareas along the study area.

New hydrological insights for the region: By using several methodological approaches, this paper emphasizes the combined effects of precipitation, river Neretva hydrological regime, melioration system operational regimes and tidal effects to the groundwater regime during the dry and rain seasons. During the dry period groundwater regime is mainly influenced by the seawater intrusion directly from the sea and from the river Neretva bed. Rain periods are characterized by the increase of the Neretva discharge thus eliminating the seawater from the river bed. This scenario results in improved quality of the groundwater. While Diga subarea faces active seawater intrusion, Jasenska's unconfined aquifer is fed by seawater from the river Neretva during the dry season. Vidrice is the only area where groundwater quality decreases during rain season due to the presence of salinized springs and the fact the area is found below the mean sea level.

1. Introduction

Coastal aquifers worldwide are negatively affected by seawater intrusion (SWI) (Custodio, 2010; Mastrocicco and Colombani, 2021; Werner et al., 2013) which is reflected through the changes in groundwater quality and reduced crop productivity in agricultural areas. These changes are expected to increase significantly as the climate changes progress (Da et al., 2015; Ketabchi et al., 2016; Oude Essink et al., 2010; Racetin et al., 2020; Sithara et al., 2020).

Besides SWI, salinization of coastal aquifers can be caused by anthropogenic contamination (de Oliveira Gomes et al., 2019; Saidi

* Correspondence to: Faculty of Civil Engineering, Architecture and Geodesy, University of Split, Matice hrvatske 15, 21000 Split, Croatia.
E-mail address: ivan.lovrinovic@gradst.hr (I. Lovrinović).

et al., 2009), rock-water interactions (Kharroubi et al., 2012; Najib et al., 2017; Rosenthal et al., 2007) and by the flow of saline water from underlying adjacent aquifers upwards (Rosenthal et al., 2007). Coastal aquifers and aquifers further inland can be also salinized due to the presence of palaeo-seawater (Delsman et al., 2014; Petitta et al., 2011; Pilla and Torrese, 2022; Shi and Jiao, 2014). Following the evolution of coastal aquifers from the Holocene to the present, older groundwater is typically found in deeper coastal aquifers (Yecheili and Sivan, 2011). Consequently, palaeo-seawater intrusion typically occurs through the uprising from deeper aquifers into aquifers closer to the ground surface (Re and Zuppi, 2011). However, depending on the evolution of study area, sources of palaeo-seawater can also be found in the shallow aquifers (Carol et al., 2021; Vallejos et al., 2018). Standard techniques for identifying salinity sources in coastal aquifers rely on determining the relationship between major ions (Santucci et al., 2016). Since palaeo-seawater and present seawater can have similar geochemical properties, ion ratios cannot always be used to successfully identify palaeo-seawater intrusion (Frollini et al., 2022). Because of the distinct isotopic fingerprint between these two previously mentioned sources of salinity, environmental isotope analysis can be used to identify the presence of both palaeo-seawater and present seawater in groundwater (Argamasilla et al., 2017). Due to the fact the previously mentioned methods require sample collection and laboratory analysis, they are unsuitable for monitoring hourly and daily changes of surface and groundwater in the study area.

Up to date various approaches emerged to understand the transient nature of SWI. The impact of SWI can be predicted fairly accurate by using variable-density numerical models and laboratory experiments (Kuan et al., 2019; Levanon et al., 2019; Paldor et al., 2019; Stein et al., 2019; van Engelen et al., 2019; Xu et al., 2019). Geochemical analysis has been proven as a successful tool for identifying salinization processes in coastal areas (Behera et al., 2019; de Oliveira Gomes et al., 2019; Khan et al., 2020; Najib et al., 2017). In addition to the aforementioned approaches, time series analysis of data obtained from installed monitoring systems in coastal aquifers has been proven to be an efficient approach for determining hydrogeological parameters (Fuentes-Arreazola et al., 2018; Xia and Li, 2009) and identifying SWI processes and salinity regimes of the groundwater as found within the coastal aquifer systems (Vallejos et al., 2014; Wood and Harrington, 2015; Yang et al., 2020; Zhang et al., 2020).

SWI as found at specific coastal systems have been a research subject of multiple number of research groups during the ongoing decade. Numerical modelling approach has been used in the work by Dibaj et al. (2021) to investigate the peculiarities affecting SWI in Taiwan site. Australian national inventory of SWI has been elaborated within the work by Morgan and Werner (2015). Variable-density modelling has been shown as a useful tool for water management of coastal systems (Abd-Elaty and Zelenakova, 2022). This is especially helpful during SWI risk assessment analysis caused by the climate change projections. In a similar manner, zoning of coastal aquifer area based on TDS, salinity and geochemical features has been presented in study by Vahidipour et al. (2021).

The Kimje coastal area in Korea has been the subject of research by Kim et al. (2005), where the relationship between observed time series of seawater elevation (SWL) and groundwater level (GWL) versus electrical conductivity (EC) in piezometers has been established, leading to the conclusion the groundwater quality is subjected to tidal influence. Similar methodology has been used to demonstrate tides affect the movement of the saltwater-freshwater interface in Jeju Island, Korea (Kim et al., 2006). Jeju Island has been again the subject of a research by Kim et al. (2008a), who analysed the dynamic behaviour of saltwater-freshwater interaction at five different coastal zones. Results showed GWL, EC and temperature (T) have been affected by tidal variations and intensive precipitation. Monitoring systems have been proven as a tool with a capacity to capture for relevant information along the Venice coast in Italy, where SWI vulnerability has been assessed by taking into account EC, GWL and distance to saline and freshwater sources (Da et al., 2015). Lovrinović et al. (2021) investigated the capacity of two independent monitoring systems, one in Neretva Valley and the second in the Venice Lagoon in Italy, based on observed GWL, EC and T time series. Both monitoring systems have been found to be capable to offer necessary information for the identification of SWI processes.

Neretva Valley represents the largest agricultural area in the coastal area of Croatia. Conservation of the area means long-term sustainability of the population living in the valley, which further emphasises the need for the monitoring and understanding the transient nature of SWI present hereby. Previous studies in Neretva Valley have been conducted as a pre-project phases for water management infrastructure implementation. Hydrogeological characterization of Neretva Valley has been performed in the study of Srzić et al. (2020) while several studies dealt with SWI related problems in Neretva coastal system (Lovrinović et al., 2022, 2021; Racetin et al., 2020; Romić et al., 2020; Zovko et al., 2018).

In this paper, local responses of the shallow coastal aquifer groundwater features to different external loadings which are assumed to contribute the complexity of SWI are investigated relying on observed values of GWL, EC, T, water level from rivers Neretva and Mala Neretva and surface and groundwater profiling results. Each piezometer location represents a different microsite along the study area with different boundary conditions representing specific local conditions and dominant loadings influencing groundwater. The relationship between the loadings to the aquifer and the aquifer response is established by using spectrograms and coherence models based on the Discrete Fourier Transform (DFT). Even though DFT has found wide application in different scientific areas, to our best knowledge this is the first time spectrograms and coherence models based on DFT are being used for the analysis especially when influenced by SWI. Besides the methodological approach, the study enables the insight to up to date results and findings to not well explored case study of Neretva coastal aquifer located in the southeastern Croatia. Compared to previous publications being focused to this case study area, hereby we summarise main differences and novelties: i) this paper covers Neretva aquifer area, including Opuzen usce, Vidrice and Jasenska areas, thus increasing the generality of the findings, ii) the relevance of hydrometeorological conditions, tidal oscillations and melioration system operative regimes has been investigated separately for different subareas of the case study, iii) this study relies on whole 2019 year of data sets, thus enabling the insight to groundwater features phenomena at the time scale larger than seasonal characteristic, iv) applied methodology enables the insight to multiple external loadings impact simultaneously via the use of coherence model.

2. Study area

2.1. Historical overview and geographical settings

River Neretva Valley is located in the very southeastern part of Croatia (Fig. 1). Specific part of the valley located between the Adriatic Sea to the west and town Opuzen to the east, has been considered as an area of interest of this paper. Through the 20th century, the alluvial soil of the Lower Neretva valley has been identified as a highly potential agricultural area mainly by local population. Until the second half of 20th century, most of 4200 ha of the Neretva valley was mainly a marshland. Starting from 1960 s up to date, an infrastructural development led to the construction of embankment Diga creating a physical barrier between the study area and the Adriatic Sea (Fig. 1), melioration channels and pumping stations. With the implementation of, firstly melioration and later flood protection and partially irrigation systems, better agricultural conditions have been reached and kept up to date.

Study area is alluvial delta fed by the alluvium from river Neretva. It is surrounded by karstic hills to the north as well as to the south and southwest. Terrain elevation of the valley's central part ranges between – 2.50 to 2.00 m a.s.l. "Nula Trsta" vertical datum is used as reference for all elevation data along the paper as well for absolute piezometric head values used within the paper. While the embankment Diga (Fig. 1) is recognised as a border between Adriatic Sea and the inland to the west, river Neretva represents a natural boundary to the north while Mala Neretva mimics the border of the Opuzen usce area to the south. Opuzen usce area can be divided into two specific sub areas, respectively Jasenska and Crepina as seen in Fig. 1. Vidrice area is separated melioration subsystem located to the south from river Mala Neretva and is surrounded by karstic hills to the east, south and west. Along the Vidrice area, the terrain elevation ranges between – 1.50 and 1.00 m a.s.l.

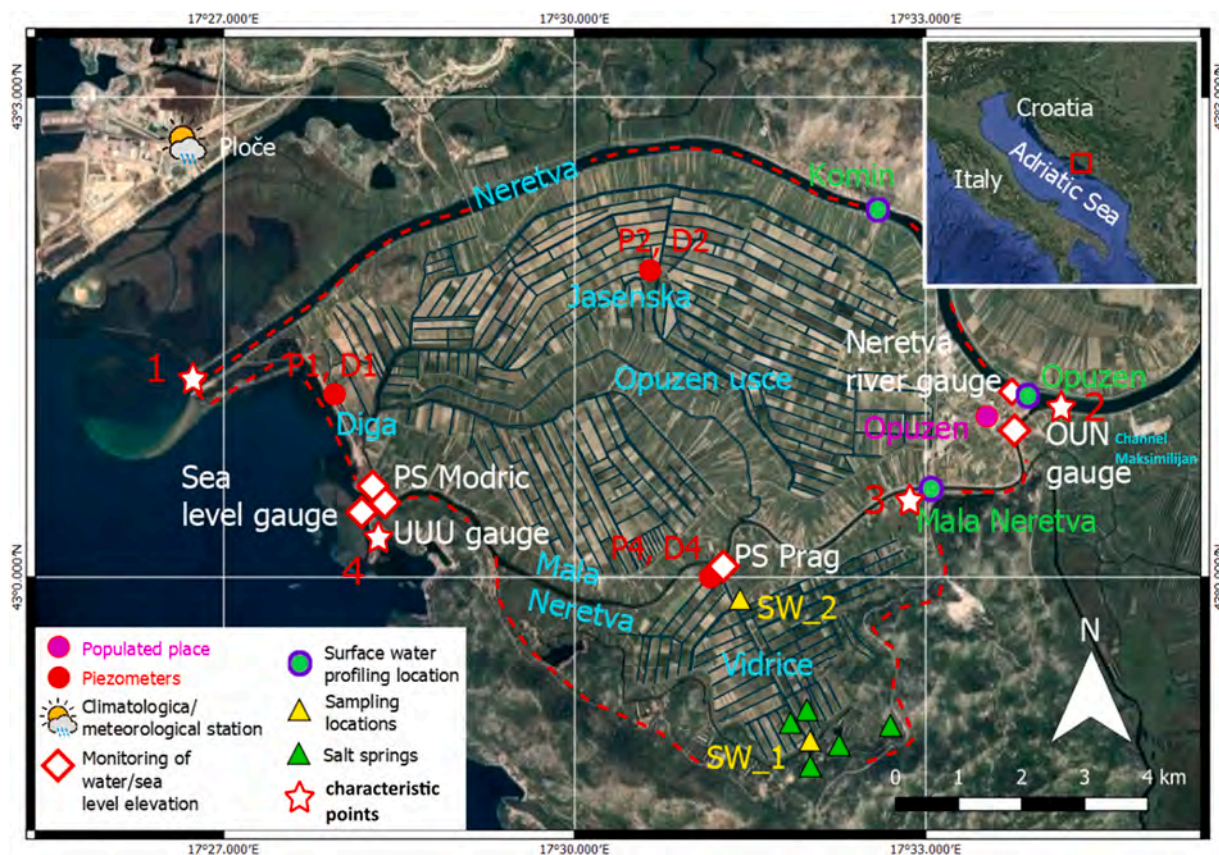


Fig. 1. Study area with the definition of monitoring infrastructure locations, melioration system infrastructure, meteorological station, gauges and profiling locations.

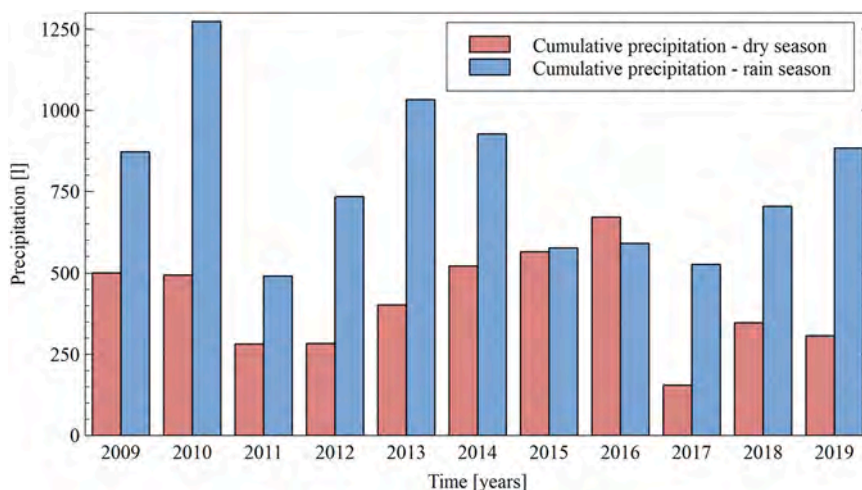


Fig. 2. Cumulative precipitation for dry and rain periods observed during 2009–2019 at Ploče meteorological station.

2.2. Climatological and meteorological conditions

Meteorological and climatological conditions along the study area have been provided by data sets observed at the meteorological station Ploče operated by Croatian Hydrometeorological Institute. Ploče station is located about 8 km to the west from the Opuzen town and 2 km to the north west from the Neretva mouth (Fig. 1).

During the reference period 2009–2019, cumulative annual precipitation ranged from 692.4 to 1768 mm year⁻¹. Through the hydrological year the area of interest is characterized by two main periods, rain season characterizing period from November to April dominantly recognised by frequent precipitation and low air T, and dry season which lasts from May to October with mainly sporadic precipitation occurrence and higher air T. During the period 2010–2019 rain season cumulative precipitation ranged between 491.2 mm and 1273.8 mm, while dry season cumulative precipitation ranged between 154.9 mm and 670.8 mm (Fig. 2).

2.3. Geological and hydrogeological settings

The geological definition of the study area has been determined by inspection and analysis of in situ geotechnical and geophysical investigations performed from 1906 s up to date (Elektrosond Zagreb, 1963, 1962; Geofizika Zagreb, 1966, 1962; Geoid-Beroš LTD, 2014; Geokon-Zagreb d.d, 2022, 2013, 2008, 2005; Institute IGH PLC, 2013, 2019). The upper layer representing unconfined aquifer unit consists of fine sands, with local presence of clay and silt. The thickness of clay and silt layers does not exceed 1 m thus representing local heterogeneities. The sand layer is found throughout the study area with a thickness ranging from 1 to 10 m depending on the location (Fig. 3). The GWL as found within the sand layer is kept below the sea level with mean annual value of -0.74 m a.s.l. for P1 location as obtained from 2019 observations, -1.93 m a.s.l. for P2 and -1.22 m a.s.l. for P4. Under the sand layer a low conductive layer of clay is found. The clay layer has a thickness of 10–12 m near the city of Opuzen and increases up to 25 m towards the sea. The further extension of this layer under the seabed from the coast to the offshore area is given as about 1400 m (Srzić et al., 2020). Beneath the clay layer a variable depth gravel layer is found. Confinement of this layer is confirmed in the study by Srzić et al. (2020). The depth of this layered roof is reported to be about 20 m in the east and up to 35 m in the west. In the central area of interest and in the northern and southern areas, a conglomerate layer is found at a depth of 40–45 m with a thickness of 1–3 m. The

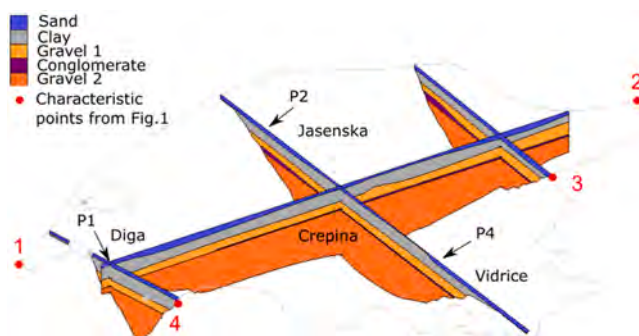


Fig. 3. Geological conceptualization of Neretva valley (study area from Fig. 1.).

discontinuity of this layer should be highlighted as this layer was not found in all available boreholes. Beneath the conglomerate layer is an expanse of gravel consisting mostly of fine and medium gravel. The mean annual value of GWL in the confined gravel layer is higher than the mean annual value of SWL (Faculty of Civil Engineering, 2019). The base of the area is defined with limestone bedrock. The bedrock was found to be zero on the edge of the Neretva valley, while in the central area, called Crepina, it reaches a depth of 165 m (Institute IGH PLC, 2013, 2019).

The determined values of hydraulic conductivity in the confined aquifer range from $7 \cdot 10^{-4}$ to $7.5 \cdot 10^{-3} \text{ m s}^{-1}$ (Srzić et al., 2020) across the entire study area with the effective porosity ranges from 0.15 to 0.25, while the values of specific storage range from 2.87 to $4.97 \cdot 10^{-6} \text{ m}^{-1}$ (Srzić et al., 2020). Confining geological unit made of clay is characterized by the hydraulic conductivity values ranging from $3.95 \cdot 10^{-12}$ to $9.66 \cdot 10^{-6} \text{ m s}^{-1}$ (Geokon-Zagreb d.d., 2022) On average values of hydraulic conductivity of unconfined aquifer have been determined from $1.15 \cdot 10^{-4}$ to $1.19 \cdot 10^{-4} \text{ (m s}^{-1}\text{)}$.

The issue of upstream boundary condition recharge of the upper unconfined aquifer of interest for this study has been shown to be of minor impact to local hydrogeological and salinity conditions as shown in work by Lovrinović et al. (2021). and Lovrinović et al. (2022). Instead, the operation of the melioration system has been shown to overcome local features and effects of precipitation, recharge either lateral inflows from the river Neretva and Mala Neretva.

2.4. Hydrological conditions

Two main processes, the amount of precipitation over the river basin and the operational regime of the Mostar Hydroelectric Power Plant, located upstream from town Mostar in Bosnia and Herzegovina, define the river Neretva discharge at the study area. From 2009–2019 discharge ranged from $40 \text{ m}^3 \text{ s}^{-1}$ to $2092 \text{ m}^3 \text{ s}^{-1}$. The amount of $40 \text{ m}^3 \text{ s}^{-1}$ represents the biological minimum of the Mostar Hydroelectric Power Plant. The Neretva River discharge shows significant seasonal fluctuations. During the dry season (from May to October) the discharge fluctuates between $40 \text{ m}^3 \text{ s}^{-1}$ and $250 \text{ m}^3 \text{ s}^{-1}$ with occasional peaks above $250 \text{ m}^3 \text{ s}^{-1}$, while rain season from November to April results with discharge values between $200 \text{ m}^3 \text{ s}^{-1}$ and $1700 \text{ m}^3 \text{ s}^{-1}$. Discharge values higher than $1700 \text{ m}^3 \text{ s}^{-1}$ corresponds to specific return periods and are adopted to specified occurrence probabilities (Hrvatske vode, 2014).

2.5. Tidal characteristics

The tides in the Adriatic Sea are of mixed diurnal-semidiurnal type (Janeković and Kuzmić, 2005; Srzić et al., 2020), with significant differences in amplitudes between neap and spring tides. The maximum amplitude of the tides in Adriatic Sea ranges from 15 cm in the southern part of the sea to 50 cm in the northern part (Janeković and Kuzmić, 2005). In a study by Srzić et al. (2020) for the period of August 2015, four dominant tidal constituents were identified within the sea level observations signature, namely O1 and K1 as diurnal constituents and M2 and S2 as semi-diurnal constituents.

2.6. Operative regimes

As already explained, Neretva valley is surrounded by rivers Neretva and Mala Neretva. Mala Neretva is a branch of Neretva river separated from the Neretva river by the gates marked as OUN and from the Adriatic Sea by the gates marked as UUU (Fig. 1). Mala Neretva system is initially designed to receive excess discharge from the Neretva River to protect the area from flooding. When the discharge of the Neretva river is greater than the capacity of the riverbed, both gates should be opened to evacuate water downstream to the Adriatic Sea. Nowadays, due to anthropogenic interventions in the area of the riverbed Mala Neretva, this system initially planned for flood protection does not fulfil its original purpose. Instead, it is used as a main source of freshwater during dry season, where water is dispersed from for purpose of irrigation.

To prevent seawater intrusion into Mala Neretva, UUU gates are regulated so the Mala Neretva water elevation is kept higher compared to the SWL. This gradient does not allow sea water cline intrude upstream from the Mala Neretva mouth. Contrary to the UUU, the OUN gates are opened rare, usually only when the water level in Mala Neretva is higher than in Neretva which happens during recession part of Neretva river hydrograph, after the occurrence of peak values. In this way, sea water cline from Neretva riverbed is not allowed to intrude Mala Neretva thus enabling the refreshment of the volume found within the Mala Neretva system. Besides the intermittent refreshment from Neretva riverbed, during dry period Mala Neretva is constantly fed by fresh water from the channel Maksimilijan whose intake is located upstream from Metković town (Fig. 1). This enables appropriate amount of fresh water which is used for irrigation of the central part of the area of interest, including Crepina area. Parallel to flood protection and irrigation systems, along the area of interest melioration system is put into operation to keep the groundwater surface elevation below the pedological layer and to enable agricultural production. In order to achieve the groundwater delineation, a system of melioration channels was built whose purpose is to bring water to pumping stations intake basins. The Modric pumping station (PS Modric) has an installed capacity of $19.6 \text{ m}^3 \text{ s}^{-1}$ and is located at the mouth of Mala Neretva. Following Fig. 1 it collects the water from Opuzen usce area and transfers it to the Adriatic Sea.

The Prag pumping station (PS Prag) has a capacity of $6.5 \text{ m}^3 \text{ s}^{-1}$ (Fig. 1) and is used for delineation of the water table within the

Vidrice area by pumping to the river Mala Neretva. Both pumping stations are turned on manually once a day during the night regime. Operation time is controlled by the supervisor of the pumping station and depends on local meteorological and hydrological conditions.

Regardless of the operational time the water level in the pumping station's intake basin is observed at the beginning and end of the working shift, normally at 10 PM and 8 AM, unless additional shifts are required during intensive precipitation events. Water level observations within the intake basins are available prior and post the pumping operation.

3. Methodology

3.1. Ground and surface water monitoring system and approaches

In the Lower Neretva Valley, a monitoring system has been installed to observe seawater intrusion parameters in piezometers (Fig. 1). These parameters include groundwater level (GWL), electrical conductivity (EC), and temperature (T). At four locations sea and rivers surface elevations were observed. Sea level (SWL) was measured near the mouth of river Mala Neretva, whereas river surface elevations (WL) were measured at two locations of Mala Neretva, one downstream from the gate in Opuzen city marked as OUN and the other (UUU) upstream from the gates near the mouth of the river. In the vicinity of the city of Opuzen, the surface elevation of the Neretva river has been observed. GWL, EC, and T in an unconfined aquifer were measured at three locations using piezometers P1, P2, and P4. All piezometers included in the study were drilled 10 m below ground level with a 12-centimeter-diameter hole. The bottom 9.5 m of the pipe's screen height have been perforated. Gauges are installed two meters up from the piezometer bottom. Following the GWL in each shallow piezometer in river Neretva coastal aquifer, only deepest 7–8 m of each piezometer screen is located below the GWL. Deep piezometers consist solely of perforations in a deep, confined aquifer, with total heights of up to 3 m, and are therefore considered as "short screened piezometers". Piezometers with similar perforation heights as used in this study have been successfully used for seawater origin determination (de Oliveira Gomes et al., 2019; Frollini et al., 2022; Pilla and Torrese, 2022; Santucci et al., 2016) and for identification of coastal aquifer external loadings and their influence to groundwater (Fadili et al., 2018; Shin and Hwang, 2020; Zhang et al., 2020).

Surface water monitoring locations are equipped with THALIMEDES OTT gauge with a sampling frequency of 1/hour, measuring range of ± 19.999 m, resolution of 0.001 m and accuracy of ± 0.002 m. OTT ORPHEUS MINI vented gauge was used in all piezometers to observe GWL and set up to sampling frequency of 1/hour with measuring range from 0 to 40 m and resolution of 0.001 m. A MANTA 2 40 + gauges were also installed in all piezometers to observe groundwater EC and T in piezometers. This gauge has a measuring range of 0–100 mS cm^{-1} with an accuracy of $\pm 1\%$ and 0.0001 mS cm^{-1} resolution for the EC standardized to 25 °C. The T sensors range is -5 °C to 50 °C with resolution of 0.01 °C and an accuracy of ± 0.1 °C. The timing of all gauges is synchronized. All gauges and probes used as a setup within the Neretva valley monitoring system are equipped with strain-gauge transducers for measuring the pressure of ground and surface water. The gauges and probes automatically convert pressure readings to a hydrostatic water pressure. In low-lying deltas, it is crucial to observe pressure rather than hydraulic head to avoid misinterpretations of groundwater fluxes' direction caused by fluids of variable density (Post et al., 2007). For the purpose of this research, time series obtained from the monitoring network during 2019. Sea and river gauges provide year-round data on the sea surface and river surface elevation, GWL, EC, and T from borehole P1, and GWL from boreholes P2 and P4. Due to malfunctioning probes, EC and T in boreholes P2 and P4 are available from January to November. The "Nula Trsta" vertical datum is used as a reference for all observed GWL, SWL, and WL values, just as it is for terrain elevation.

In order to gain insight into the vertical stratification of EC and T, six profilings were performed throughout the 2019. Profiling is performed on all piezometers and the Mala Neretva river. They are conducted primarily during the dry season, with the exception of the most recent profile, which was conducted in November and did not include Mala Neretva (Table 1). The SEBA KLL-Q-2 multi-parameter probe was used to record GWL and EC T values at various depths. The probe has the following measuring ranges: 0–500 m water column for pressure, -5 °C to 50 °C for T, and 0–200 mS cm^{-1} for EC.

Table 1
Locations, dates and time of profilings.

| Time and location of profiling | | | | | |
|--------------------------------|-------------|-------|-------|-------|-------|
| | Date | P1 | P2 | P4 | MN |
| 1 | 17.06.2019. | 11:30 | 10:28 | 09:50 | 08:00 |
| 2 | 17.07.2019. | 12:10 | 10:57 | 09:13 | 08:45 |
| 3 | 22.08.2019. | 10:45 | 09:55 | 08:15 | 08:00 |
| 4 | 18.09.2019. | 08:30 | 09:55 | 11:10 | 08:35 |
| 5 | 09.10.2019. | 11:10 | 10:15 | 09:30 | 08:35 |
| 6 | 25.11.2019. | 11:25 | 12:20 | 13:25 | - |

3.2. Time series spectrogram and coherence

Observed time series in boreholes, whether the groundwater head or EC, indicate the composition of various aquifer stresses. Each aquifer stress corresponds to a particular frequency or group of frequencies, with amplitude, period, and phase corresponding to each frequency (Dong et al., 2015). Every periodic and aperiodic function in time is decomposed by the Fourier transform into the sum of the sine and cosine functions (Proakis and Manolakis, 2006). Observed signals represent discrete time series, therefore the emphasis of Fourier Transform is on the discrete signals. The formula for Discrete Fourier Transform (DFT) (Cooley et al., 1969) is

$$X_k = \sum_{n=0}^{N-1} x_n e^{-\frac{j2\pi kn}{N}} \quad k = 0, \dots, N - 1 \tag{1}$$

Using Euler's formula Eq. 1 can be written as

$$X_k = \sum_{n=0}^{N-1} x_n \left[\cos\left(\frac{2\pi kn}{N}\right) - i \times \sin\left(\frac{2\pi kn}{N}\right) \right] \quad k = 0, \dots, N - 1 \tag{2}$$

or

$$X_k = A_k + iB_k \tag{3}$$

where X_k is the value of the k -th frequency in the frequency bin, k is the number of frequency in the frequency bin, N is the number of samples, x_n is the n -th sample value, and A_k and B_k are complex numbers. The frequency resolution of a plot or frequency bin is defined as the sampling frequency divided by the number of samples. The frequency of the k -th position in the frequency bin is defined as:

$$F_k = n \frac{f_s}{N} \tag{4}$$

where f_s is sampling frequency and n is the sample number. Plotting A_k and B_k in complex plane, magnitude (M) and phase (φ) of each frequency can be calculated.

$$M_k = \sqrt{A_k + B_k}; \varphi_k = \tan^{-1} \frac{B_k}{A_k} \tag{5}$$

Typically, DFT results are displayed as amplitude spectral density (ASD) or power spectral density (PSD). Normalizing the DFT results by the number of samples entered in DFT yields an ASD, and the squared value of the ASD's amplitude yields a PSD. The periods and amplitudes of each calculated frequency can be easily deduced from the amplitude spectrum (Fuentes-Arreazola et al., 2018; Srzić et al., 2020; Turnadge et al., 2019).

Stresses on the aquifer can be divided into periodic stresses such as tides, daily changes in atmospheric pressure, daily operating regime of pumping stations and non-periodic stresses, which are usually caused by a change in meteorological conditions or operating regime. In the case of non-periodic stresses, such as precipitation, the ASD of the aquifer response will have a range of frequencies with different amplitudes to mimic the non-periodic signal (Isermann and Münchhof, 2011) so a closer look at the time series in the frequency domain is necessary.

The coherence model was used to establish a measure of similarity as a function in phase shift between frequencies calculated from observed signals represent stresses on the aquifer and aquifer response signals. The following is the formula for magnitude square coherence:

$$r(k) = \frac{|G_{XY}(k, \varphi)|^2}{G_{XX}(k)G_{YY}(k)} \tag{6}$$

$G_{XY}(k)$ represents the cross power spectral density (CPSD), whereas $G_{XX}(f)$ and $G_{YY}(f)$ represent the PSD of signals. PSD can also be described as the Fourier transform of the auto-covariance function, while CPSD can be described as the Fourier transform of the cross-covariance function between two signals as a function of phase shift. Coherence values range from 0 to 1, with 1 indicating complete coherence and 0 indicating incoherence.

Since the coherence model does not include information about the amplitude size of the coherence frequencies, it is possible to have significant coherence between both frequencies of interest and noise. The Welch method (Welch, 1967) was used to avoid the interpretation of coherence between noise frequencies and to highlight the dominant frequencies. First, time series are partitioned into a finite number of smaller time series known as screens, and then the Welch method is applied to each screen. Moving a window over a data set on-screen and calculating the ASD or PSD each time the window is moved is required by the Welch method. The average of all ASDs in a screen is recorded, and all screens are combined to form a spectrogram, which is an image depicting the distribution of all ASDs. The spectrogram provides information about the spectrum's temporal evolution (Pérez-Gómez et al., 2016). To ensure calculation consistency, the Welch method was applied to the spectrogram with the same window shape, size, and overlap points as the coherence model. The results were calculated using modules from the SciPy library, which is integrated with Python 3.7. The coherence models and Welch's method Scipy modules are based on the same study (Welch, 1967).

Observed annual time series were divided into 24 periods (referred to as screens) with 15-day data for each screen (see A. Appendix). The coherence between two time series was calculated for each screen. Using a Tukey window with a shape parameter of 0.25

and a window length of 120 data (5 days), reliable monthly coherence results were determined. The Tukey window was shifted over 110 overlapping data points to generate 24 coherence models for each window. In the results, the mean value of all coherence models was interpreted.

4. Results

To identify and elaborate processes influencing SWI and its impact to groundwater dynamics within Neretva case study, we separately analyse three locations of interest along the study area. Those three locations correspond to fundamentally different areas respectively: i) Piezometer P1 at Diga area which is dominantly influenced by the SWI, ii) Piezometer P2 located at Jasenska area which is a part of river Neretva left bank area and iii) P4 piezometer which is representative for Vidrice melioration subsystem. The analysis has been performed based on: i) continuous data series of EC, T and GWL, ii) SWL and WL and iii) on groundwater and surface water profilings of T and EC performed six times during 2019.

4.1. Diga area

Fig. 4 demonstrates the correspondence of trends of GWL in P1 and SWL. Both trends imply the influence of atmospheric pressure, which can be seen by the increase in the atmospheric pressure and the decrease in GWL and SWL trends, and vice versa. The specific occurrence of such an inverse interdependence of these two variables of interest and the atmospheric pressure is especially evident during significant atmospheric pressure changes during late January, mid and late February, early April and May, mid and late October, and several changes during November and December 2019.

During 2019, PS Modric intake basin water elevation reflects the chainsaw feature which is a consequence of dominantly night operative regime (Fig. 4). Turbines are put into operation at the end of the day, usually between 8 and 10 PM, depending on local hydrological and meteorological conditions, while the turnoff is usually scheduled between 6 and 9 AM. This feature is noticeable by the inspection of spectrogram in Fig. 5b, where daily period is observed as present during the whole year of interest. Significant changes in the amplitude of the PS Modric intake basin water surface elevation are present for larger periods during January 2019 when significant decrease in atmospheric pressure and precipitation occurrence are present. The annual mean GWL at P1 equals to 1.09 m beneath than the mean SWL, indicating the presence of active seawater intrusion conditions (Badaruddin et al., 2017, 2015).

In the studies by Lovrinović et al. (2022, 2021) and Srzić et al. (2020), the tidal signal in the SWL characterizing study area is identified of a mixed type, with regular changes in the periods of spring and neap tides (Fig. 4). Observed dominant frequencies of GWL in P1 (Fig. 5c) correspond to the dominant frequencies of the sea level signal (Fig. 5a) with noticeable decrease in amplitudes due to the attenuation caused by the filtering effect of the aquifer media. The semidiurnal component in the SWL has a larger mean annual amplitude value (0.013 m) compared to diurnal component (0.11 m), while the opposite occurs in the P1 GWL, respectively, the semidiurnal component has a value of 0.028 m and the diurnal has a value of 0.03 m. This is expected since the tidal efficiency is dominantly influenced by the signal period rather than the amplitude (Erskine, 1991; Jiao and Tang, 1999). Specific yield in the

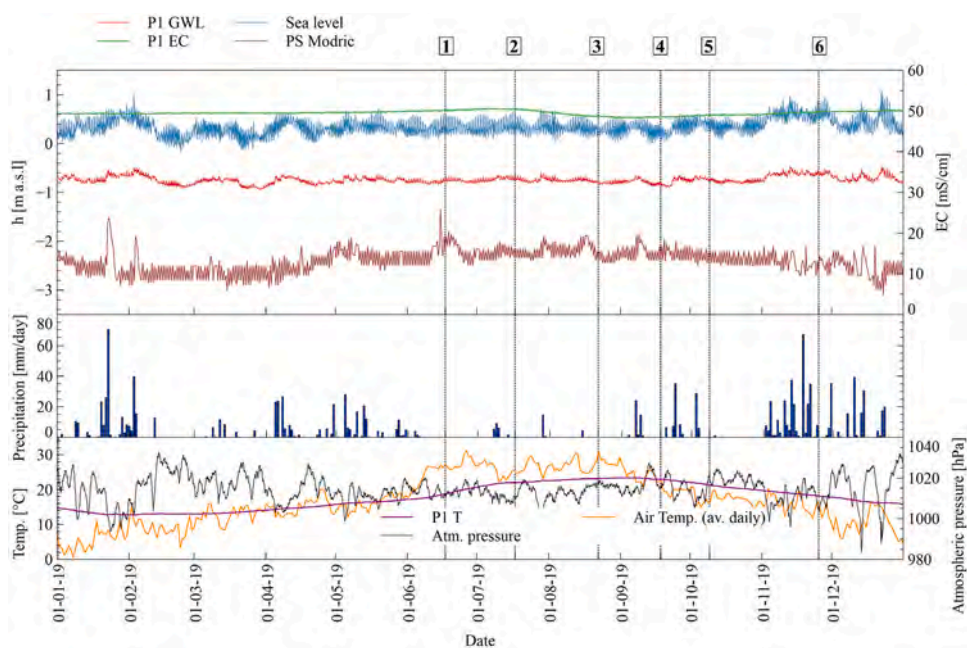


Fig. 4. Observed meteorological, hydrological and hydrogeological data, PS Modric intake basin WL, GWL, EC and T for the location P1 and profilings marked with numbers from 1 to 6, for 2019.

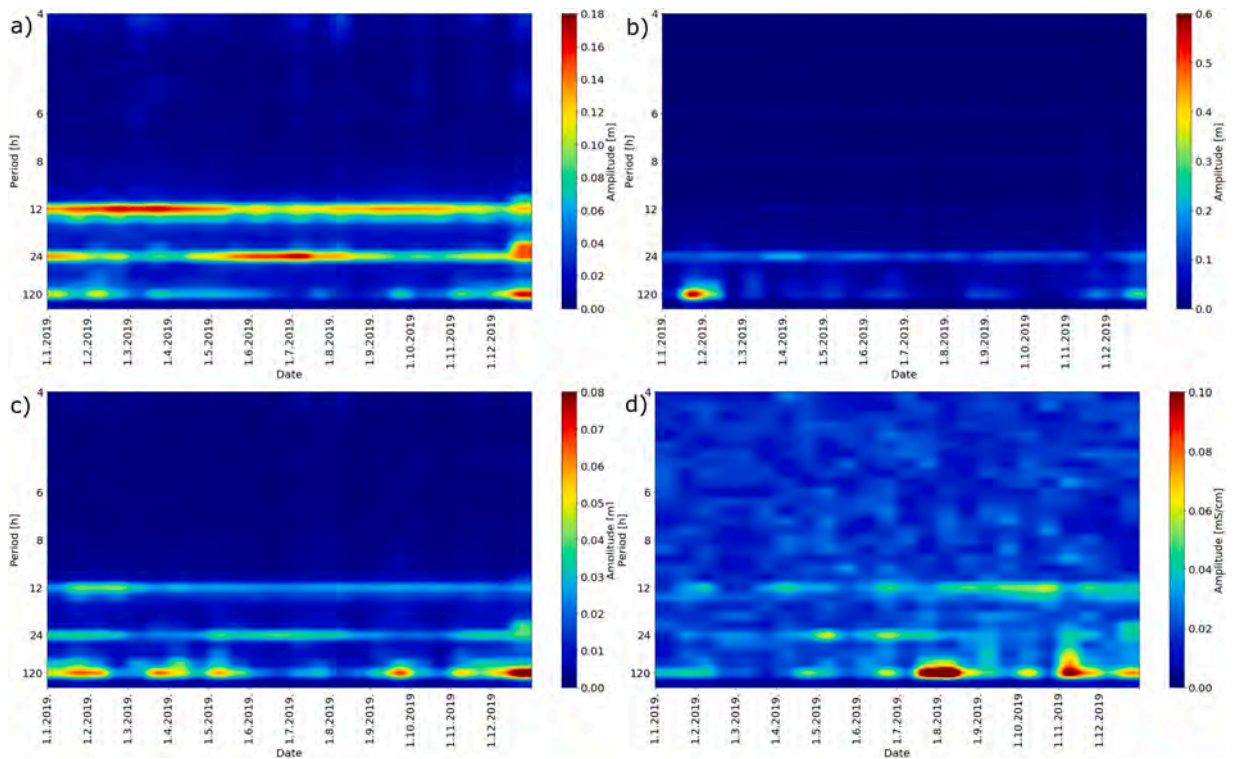


Fig. 5. ASD spectrograms representing: a) SWL, b) PS Modric water level, c) P1 GWL and d) P1 EC.

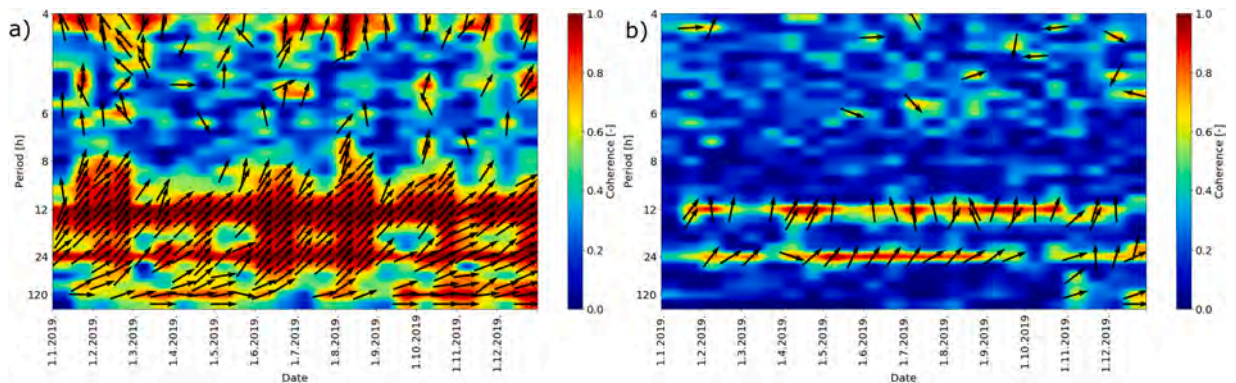


Fig. 6. Coherence model between a) SWL and P1 GWL and b) SWL and EC in P1.

unconfined aquifer can have several orders of magnitude higher values than the storativity in the confined aquifer and therefore the attenuation of sea level oscillations within the unconfined aquifer is larger (Guo et al., 2007; Ratner-Narovlansky et al., 2020) compared to confined aquifer conditions (Srzić et al., 2020). Studies (Teo et al., 2003; Yeh et al., 2010) have shown unconfined aquifers in coastal systems can be significantly affected by the SWL fluctuations supporting the similarity with P1 observed GWL.

Deeper inspection of the similarity between the P1 GWL and SWL time series has been derived from the spectrogram analysis as shown in Fig. 5a and c. Hereby, P1 GWL implies the similarity with SWL when analysed in frequency domain. Dominant amplitude spectrum values correspond to mixed tide periods as observed by Srzić et al. (2020) confirming the dominance of the SWL in the transient definition of P1 GWL. The latter is expected due the fact P1 is located 80 m from the coastline and is therefore directly affected by the SWL variations that couples the effect of the atmospheric pressure and tidal influence. Long-term changes in atmospheric pressure are also visible in the spectrogram of SWL and P1 GWL (Fig. 5a and c) for the frequencies corresponding to periods higher than daily. Highest amplitude values are present for the periods of January, mid and late February, early April and May, mid and late October, and several changes during November and December (Fig. 5c). Those periods emphasize the nature of the cause of atmospheric pressure which is explained as a consequence of the air front movement along the pathway over different geographic locations (Dong et al., 2015; Merritt, 2004). The latter is different and should be distinguished from the daily changes in atmospheric pressure, mostly caused by day-night regime of the T change.

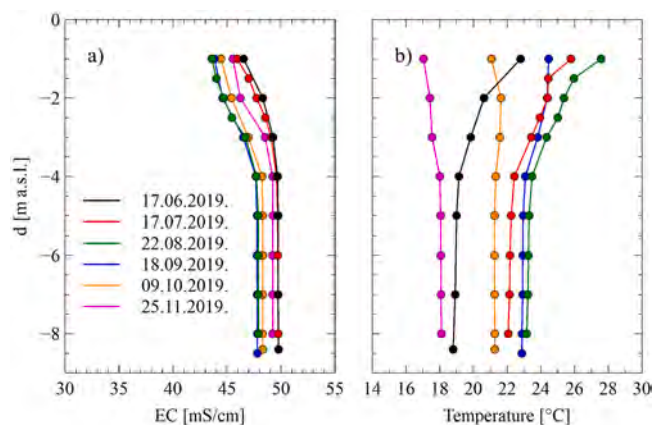


Fig. 7. Groundwater profiles in P1 performed six times during 2019: a) EC profiles and b) T profiles.

The values of the coherence model are shown in Fig. 6 with the colour bar, where total coherence is marked with red colour and no coherence with blue colour. Arrows indicate the phase in degrees between the same frequency in two signals with coherence determined as 0.6 or higher. An arrow pointing to the right denotes no time lag between two constituents of signals of interest while an arrow pointing to the left means opposite phases of the corresponding constituents. The arrow representation has been shown to be a suitable method for visualising time lags between frequencies in two signals (Briciu, 2019; Zhang et al., 2020). Also, frequencies with periods between 2 and 4 h were removed from the spectrogram and coherence results because they correspond to noise frequencies (Dong et al., 2015) and to improve the visibility of frequencies of interest. Mean annual coherence values of 0.95 and 0.99 have been determined between diurnal and semidiurnal frequencies corresponding to SWL and GWL in P1, with an annual mean time lag of 2.68 h and 0.77 h standard deviation for the diurnal, and a time lag of 1.58 h and 0.24 h standard deviation for the semidiurnal component. Fig. 6a indicates the SWL and GWL trends occur at the same time implying the cause different than tides.

Following the significant interconnection between SWL and P1 GWL we extend the analysis to EC, assuming the SWL as a driving force controlling the EC in P1. EC in P1 has a relatively constant value varying slightly between 48.16 mS cm^{-1} and 50.7 mS cm^{-1} throughout the year (Fig. 4). Coherence inspection between SWL and P1 EC reveals significant values for periods corresponding to the tidal constituents in Fig. 6b. Annual mean values of EC time lag relative to SWL corresponds to 2.49 h with coherence of 0.71 for diurnal constituent. Semidiurnal constituent corresponding time lag equals to 2.58 h with 0.73 coherence value. The standard deviation values of 1.71 h and 0.91 h have been determined for annual time lags of the diurnal and semidiurnal constituents.

Precipitation does not dominate the EC values in P1, compared to SWL influence as can be seen in Figs. 4 and 5d The latter is a consequence of several factors: i) the position of the probe below the transition zone in P1 (Fig. 7a), ii) proximity of the Adriatic Sea, and iii) precipitation occurred at the study area drains towards the melioration channel located 30 m inland from the P1.

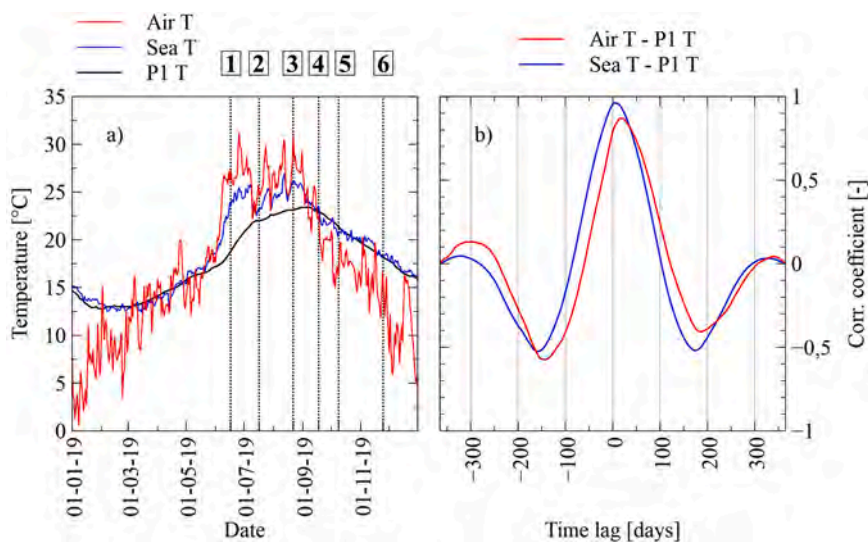


Fig. 8. a) Observed average daily T in P1, observed average daily sea T as observed at monitoring station Ploče and observed average daily air T as observed at meteorological station Ploče time series for 2019 and, b) Cross-correlation between air (T) and P1 (T), and sea (T) and P1 (T).

EC profiles (Fig. 7a) can be divided into two layers, the first layer (transition zone) from the surface to a depth of -4 m a.s.l. and the second layer from -4 m a.s.l. to the position of the piezometer probe at -9 m a.s.l. While EC profiles in unconfined aquifers in the seawater proximity usually show transition from freshwater to seawater in EC profiles (Kim et al., 2008b, 2006; Shin and Hwang, 2020), hereby the transition zone detectable from Fig. 7 has a transition zone with a maximum difference between upper and lower values of 4.13 mS cm^{-1} . By coupling the shape of the profiles of EC and the fact the GWL in P1 is found below SWL suggests active seawater intrusion conditions along the Diga area represented by P1 (Badaruddin et al., 2017, 2015). The layer below the transition zone does not show stratification in EC but vary up to maximum 1.96 mS cm^{-1} as observed between the first and fourth profiling.

The T profiles in P1 can be divided vertically into two sub layers, same as for the EC. The first layer up to a depth of 4 m shows vertically varying T, while the second layer below 4 m has relatively constant T (Fig. 7b) changing from 18° to 23°C . Highest observed T in upper layer are observed on July 17th and August 22nd during the peak of the summer season, while highest observed T in deeper layer are observed on August 22nd and September 18th. This indicates the upper layer responds faster to changes in air T than the deeper layer which is controlled by the Adriatic Sea T. P1 T increase from 18.80°C as observed on June 17th to maximum 23.10°C observed on August 22nd at the piezometer bottom is caused by its proximity to the Adriatic Sea and the influence of SWI. Similar effect but with decreasing trend has been observed during the profiling performed on September 18th, October 9th and finally November 25th when lowest observed T (18°C) has been observed.

The P1 piezometer is located approximately 80 m from the coastline and 30 m distance from the melioration channel converging the water towards the PS Modric intake basin. By comparing the mean annual values, the water level in the PS Modric intake basin is determined at 2.74 m below the sea level, indicating the presence of active seawater intrusion conditions within the area represented by P1. Uniquely, this causes a continuous inflow of seawater into the inland thus transferring the seawater inland. Active SWI results in the salinization of the entire water column and the absence of fresh groundwater discharge to the sea (Badaruddin et al., 2017, 2015). This is confirmed by both the EC and T profiles in P1 (Fig. 7a and b), which reveals the presence of seawater in P1. Assumption of the interdependence between P1 T and the Adriatic Sea T has been validated by use of available T time series. Unless the P1 T has been observed by the implemented monitoring system, Adriatic Sea T at the study area has been taken by the available web service (<https://seatemperature.info/hr/hrvatska/ploce-temperatura-vode.html>) (Fig. 8a and b). Although the a-priori dependence is clearly visible from Fig. 8a. Fig. 8b depicts a cross-correlation model that provides additional confirmation of this. The highest observed cross-correlation coefficient between average daily Adriatic Sea T and average daily P1 T is 0.96 with a time lag corresponding to 6 days implying the P1 T being late for the sea T. Similar finding valid for the EC and piezometric head but with different time scales has been evidenced in the work by Lovrinović et al. (2022) for the period of August-October 2021. Unless the interdependence of the P1 deeper water column T and the Adriatic Sea T, upper water column T (above -4 m a.s.l.) is dominantly influenced by the T changes induced by insolation from the air T. Observed cross-correlation coefficient between air T and P1 T corresponds to value of 0.86 with time lag of 18 days (Fig. 8b) demonstrating minor influence of air T to control the P1 T compared to sea T influence.

4.2. Jasenska area

Inspection of Fig. 9 initially emphasize interdependence between river Neretva discharge, PS Modric intake basin surface water elevation and GWL in P2. Following longer precipitation occurrence during rain season, river Neretva discharge is increased reflecting the P2 GWL increase. During the dry season, river Neretva discharge is observed mainly below $250 \text{ m}^3 \text{ s}^{-1}$ and GWL within the shallow aquifer follows the mean value of the surface water elevation observed in the PS Modric basin thus demonstrating the superiority of PS Modric operation in the definition of the groundwater regime as found along the whole Opuzen usce area and especially Jasenska sub area. It is important to note P2 is located only 75 m away from the channel Jasenska which strengthen the fact about the melioration system operative regime influence to P2 GWL.

The occurrence of precipitation is followed by an increase in P2 GWL (Figs. 9 and 10a). In the absence of precipitation during the dry period, the mean GWL in P2 corresponds to the mean water level elevation in PS Modric, emphasizing the influence of PS Modric's operational regime. Daily oscillations in P2 GWL are only detectable via the coherence model between the WL in PS Modric and the GWL in P2 (Fig. 11a). These daily oscillations correspond to the PS Modric's night and day operational schedule. Mean coherence values obtained between the PS Modric level and GWL in P2 equals to 0.84 and 0.65 respectively for diurnal and semi-diurnal frequencies during the dry period while precipitation reduces those values of 0.38 and 0.34 respectively (Fig. 11a). This difference distinguishes two periods with different factors controlling the P2 GWL. Unless the rain season causes the change in river Neretva hydrological regime which acts to dominate GWL in Jasenska shallow unconfined aquifer, it is the PS Modric driven melioration system which controls the GWL along the inland of Opuzen usce area during dry season. Inspection of time lags between the PS Modric water elevation induced by precipitation and P2 GWL from the coherence model shown in Fig. 11a reveals the simultaneous change in those variables during precipitation occurrence unless the P2 change driven by the PS Modric operation during dry season is characterised by time lag of 3.23 h for diurnal related frequency.

Transience of EC as observed at P2 shows different response to precipitation compared to GWL. While the P2 GWL is increased due to the precipitation, EC is reduced. This is especially visible after precipitation of 30 mm day^{-1} or greater. The highest drop in EC value has been observed between January 22nd and February 2nd, when EC decreased by 29.1 mS cm^{-1} to a final value of 13.63 mS cm^{-1} (Figs. 9 and 10b). A similar effect is observed in May after a precipitation of 28 mm day^{-1} but with a less pronounced drop in EC. Although notable amount of precipitation occurred during November and December, the response of EC values in P2 is missed due to probe malfunction during this period. After the precipitation ends, EC in Jasenska area shows exponential recovery feature which reflects slow but significant influence of the external stress controlling the EC rise at the probe depth.

During the dry season, when Neretva discharge falls below $250 \text{ m}^3 \text{ s}^{-1}$, EC values observed in P2 are usually above 50 mS cm^{-1}

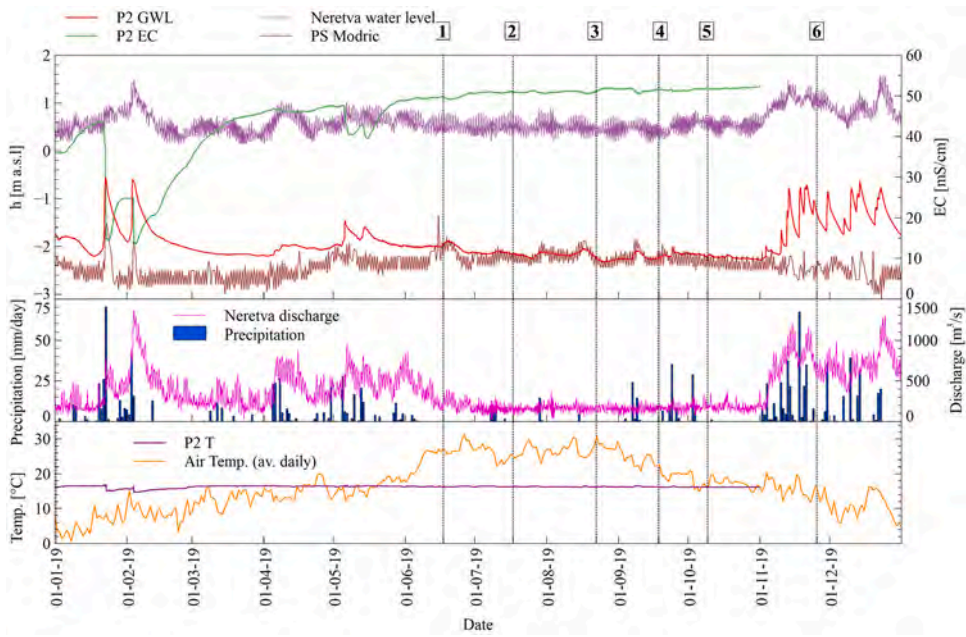


Fig. 9. Observed meteorological, hydrological and hydrogeological data, PS Modric intake basin WL, GWL, EC and T for the location P2 and profilings marked with numbers from 1 to 6, for 2019.

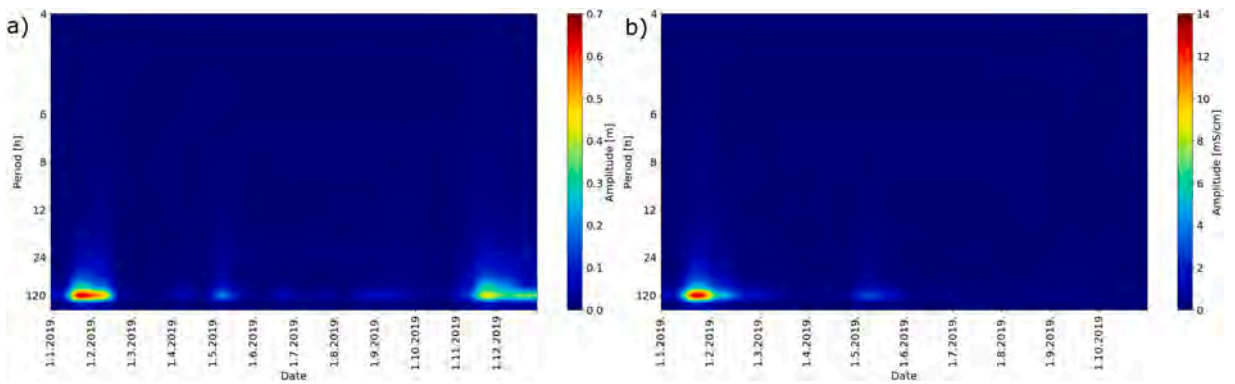


Fig. 10. ASD spectrograms representing: a) P2 GWL, b) P2 EC.

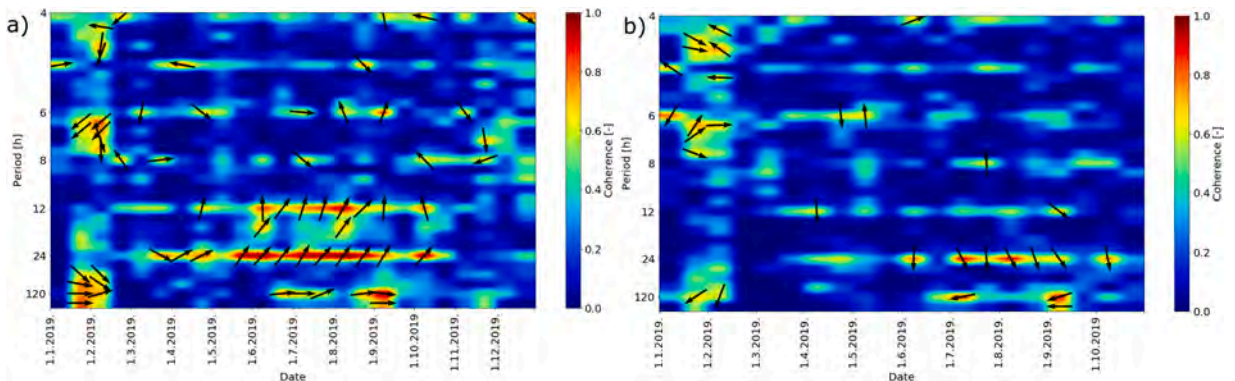


Fig. 11. Coherence model between a) PS Modric WL and P2 GWL and b) PS Modric WL and P2 EC.

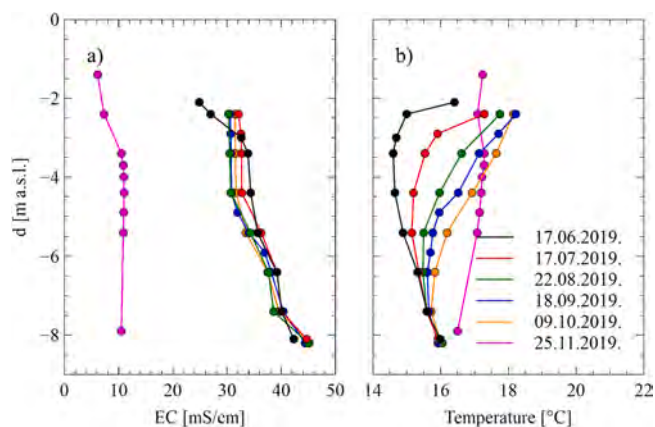


Fig. 12. Groundwater profiles in P2 performed six times during 2019: a) EC profiles and b) T profiles.

which is the evidence of significant volume of seawater affecting the radius of influence of the piezometer. Similar results were presented in the study by (Lovrinović et al., 2021).

Precipitation effects in EC can also be seen in the spectrogram as an increase in drops during late January, early February and early May (Fig. 10b). The coherence between PS Modric water level and P2 EC (Fig. 11b) reveals values higher than 0.60 for the frequencies corresponding to the precipitation occurrence during late January, early February, mid July and mid September, as well as for diurnal frequencies during summer. The latter implies the interplay of precipitation and PS Modric operative regime in EC control hereby. The frequencies corresponding to the precipitation occurrence show negative phase of P2 EC relative to PS Modric intake basin water elevation (Fig. 11b), which means the increase of the surface water elevation in the Jasenska channel due to the operating regime of PS Modric causes the decrease in P2 EC and vice versa.

The diurnal components of PS Modric water level and P2 EC possess maximum coherence values of 0.88 and 0.87 respectively during July and August, when the peak of the dry season occurs. Hereby the time lag of the EC relative to the cause of EC change equals to 15–17 h.

EC profiles (Fig. 12a) were obtained to a depth of – 8.3 m a.s.l. (due to the probe location in piezometer) with a maximum value of 45.16 mS cm^{-1} observed above the probe on October 9th (fifth profiling), while the minimum value above the probe has been observed on November 25th (sixth profiling) at 10.49 mS cm^{-1} . The profiling has been performed after long rain period with an average daily river Neretva discharge of $625 \text{ m}^3 \text{ s}^{-1}$ and minor stratification in P2 EC noticed. The profiling performed on June 17th show most significant EC values stratification. This difference is a consequence of the decrease of the Neretva discharge during the transition from rain to dry period, indicating the freshwater from the rainy period is still present in the upper layer of the unconfined aquifer. Four profiles obtained during the dry period show a negligible difference among themselves and a kind of stable groundwater column.

Contrary to EC and GWL, T in P2 shows stability with minor changes except two isolated rainfalls during January 22nd and February 2nd when small decrease in GWL T is noticed. For the same reason as mentioned for EC, T data series is not available during November and December. T profiles (Fig. 12b) correspond to the recharge type of T profile (Kayane et al., 1985) with constant T at the bottom and pronounced vertical stratification. The main processes of recharge, as seen in Figs. 9 and 12 are assumed as infiltration of precipitation into the aquifer and SWL. Surface to ground T may represent T over a time scale, with surface T referring to the effect of daily air T. T observed at final depth may represent the average annual T or the mean T of a longer period as seen in Fig. 9.

4.3. Vidrice area

P4 GWL has noticeable diurnal oscillations (Figs. 13 and 14c) with an increasing trend during precipitation events. The highest precipitation induced increase has been observed on January 23rd when a precipitation of 70.3 mm day^{-1} caused increase of P4 GWL of 0.87 m. Trends of GWL in P4 and PS Prag intake water elevation caused by precipitation during January, April, May and December coincide as shown in Figs. 13, 14b and c and 15c.

Diurnal oscillations of P4 GWL do not show transition between spring and neap tide (Fig. 13). Instead, regular alternation of one maximum and one minimum daily are observed which corresponds to the operating regime of PS Prag. Tidal efficiency of 0.76 has been identified during August between PS Prag surface water elevation and P4 GWL representing the dominance of the PS Prag operation in the P4 GWL definition. The coherence model applied to PS Prag water elevation and P4 GWL time series in Fig. 15c confirms corresponding diurnal variations with coherence value 0.99 and no time lag between during whole year since the distance in between is less than 20 m.

Additional inspection of the influences to P4 GWL has been focused to Mala Neretva water elevation represented by UUU. As explained within the chapter 2, Mala Neretva is closed system except during specific circumstances when OUN or UUU gates are opened. Unless no OUN manoeuvre has occurred during 2019, several opening manoeuvres of UUU have been captured based on the insight to UUU time series in Fig. 13. Since the gates opening, SWL becomes a boundary condition defining the Mala Neretva water elevation. Periods referring to the UUU opening correspond to late January and early February, early April and May as well as during

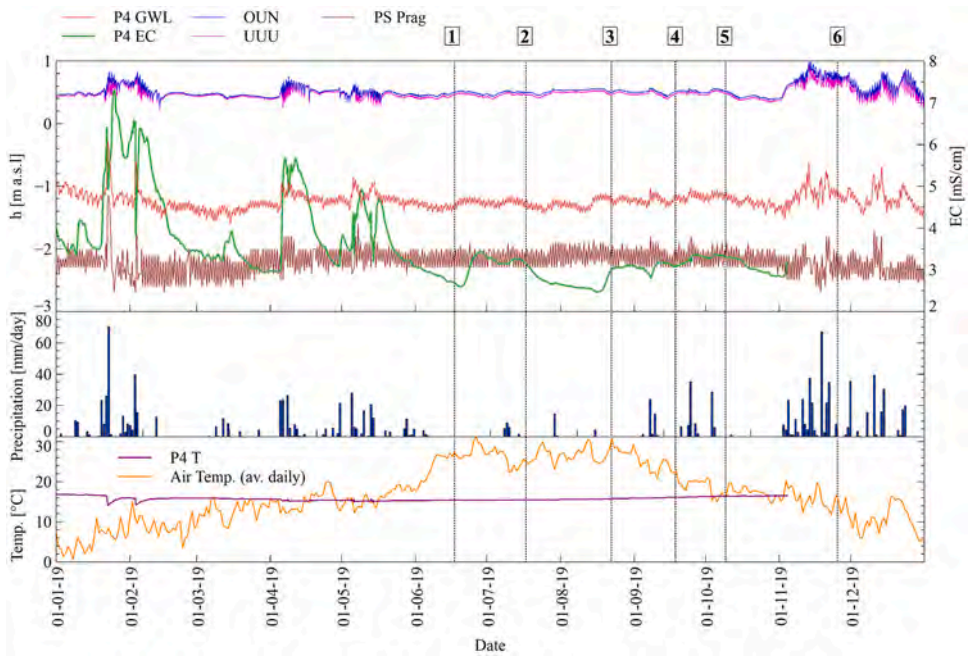


Fig. 13. Observed meteorological, hydrological and hydrogeological data, PS Prag intake basin WL, GWL, EC and T for the location P4 and profiles marked with numbers from 1 to 6, for 2019.

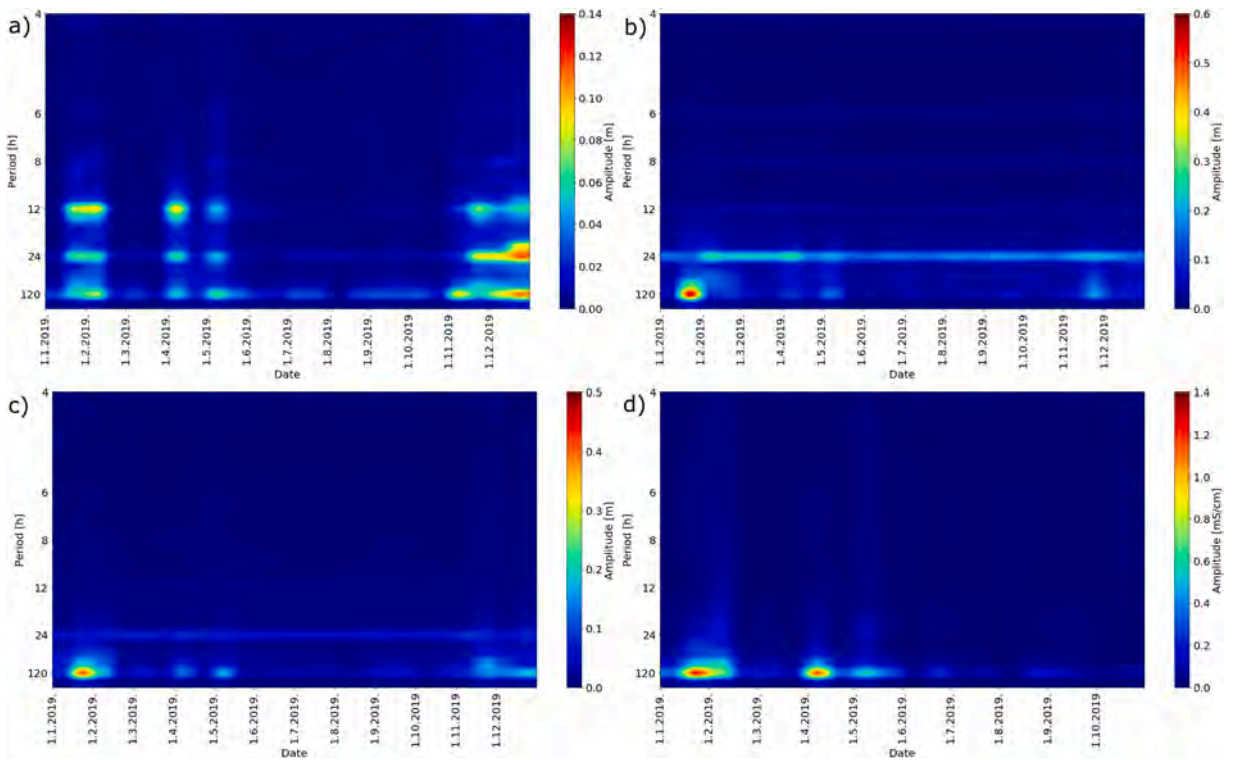


Fig. 14. ASD spectrograms representing: a) UUU, b) PS Prag WL, c) P4 GWL and d) P4 EC.

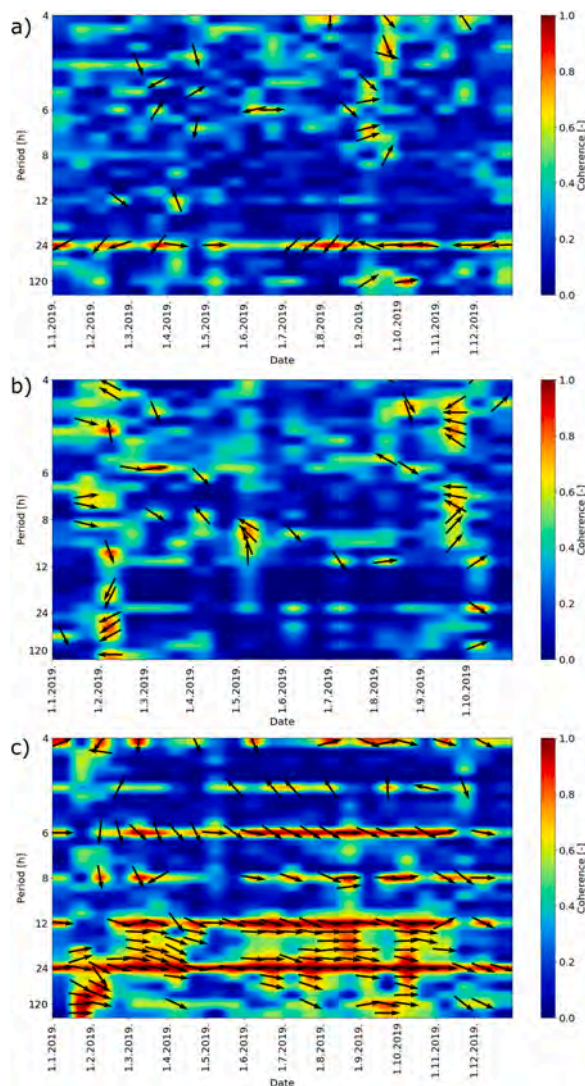


Fig. 15. Coherence model between a) UUU level and P4 GWL; b) P4 GWL and EC in P4 and c) PS Prag WL and P4 GWL.

November and December, as can be seen in Fig. 13 and Fig. 14a. Due to the connection with the Adriatic Sea, Mala Neretva water elevation shows presence of diurnal and semidiurnal components in its periodicity. The coherence between UUU water level and GWL in P4 has a mean value of 0.7 for the frequency with period of 24 h with varying phase between them (Fig. 15a). This can be explained by the fact both signals are influenced by daily changes in atmospheric pressure in addition to GWL oscillations in P4, where daily oscillations of PS Prag are detectable (Figs. 14b and 15c), thus creating different phases between these two signals.

Observed P4 EC values (Fig. 13) show P4 contains mostly brackish water. During the dry period, the EC values are mostly found below 3 mS cm^{-1} at the probe level, while the rain period leads to increase up to 7.31 mS cm^{-1} . From January 20th to January 22nd with on average daily precipitation of 19.1 mm day^{-1} , EC increased from 3.56 mS cm^{-1} to 6.42 mS cm^{-1} . EC reduction from 6.42 mS cm^{-1} to 4.93 mS cm^{-1} has been observed after the precipitation of 70.3 mm day^{-1} . Correspondence in the transient nature of P4 GWL and EC is supported by the spectrograms in Fig. 14c and d. A closer look at those correspondence events shows two phenomena of the behaviour of EC in P4: i) increase of EC occurs after the precipitation and ii) when the precipitation overcomes approximately 40 mm day^{-1} , EC decreases. Coherence evidences significant correlation between P4 GWL and EC especially during precipitation occurrence (Fig. 15b). Unless precipitation exceed 40 mm day^{-1} , the time lag shows EC change occurs with phase lag equals to half of the period corresponding to the frequency of interest. This means the increase in GWL leads to reduction in EC. The latter is shown to be sensitive to window size used during the coherence analysis performance.

The T time series in P4 show similar characteristics to the T observed at P2. The T shows mostly constant values throughout the year, with isolated drops in the T during precipitation periods. Highest T drops are observed after heavy precipitation in late January and early February. Besides those two events, the T in P4 ranges between $14.95 \text{ }^\circ\text{C}$ and $19.11 \text{ }^\circ\text{C}$ over the observed period. Inspection of EC and T profiles at P4 and Mala Neretva implies no interdependence (Figs. 16a and 16b). EC in P4 fluctuates from 2.40 to 3.15 mS

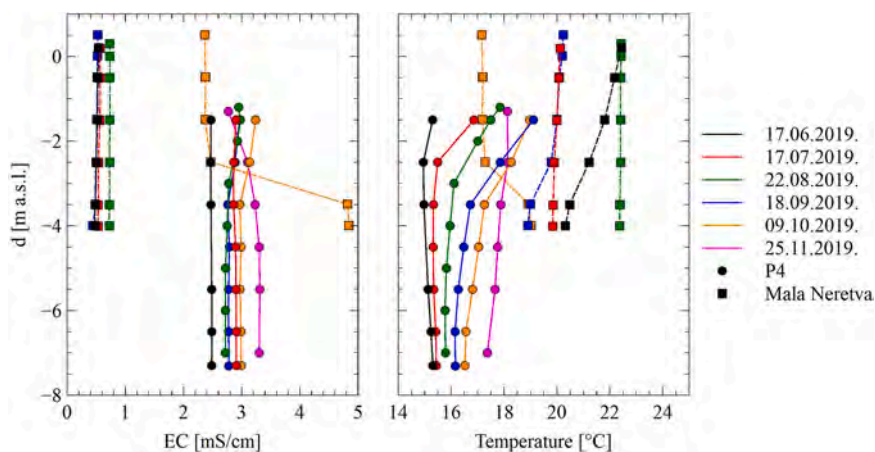


Fig. 16. Groundwater profiles in P4 and surface water profiles in Mala Neretva performed six times during 2019: a) EC profiles and b) T profiles.

cm^{-1} without the stratification in the unconfined aquifer. Highest T observed during profiling equals to $17.50\text{ }^{\circ}\text{C}$ and has been observed during sixth profiling performed on November 25th. Similar finding has been reported for Jasenska area and P2 piezometer. Previously analysed interdependence between Mala Neretva water elevation and P4 GWL did not show similarity. The inspection of EC profiles emphasizes almost freshwater as found along the Mala Neretva which supports the primary scope of Mala Neretva as a main source of fresh water suitable for irrigation of the area of interest.

5. Discussion

In this paper an analysis has been presented with a goal to understand factors controlling the groundwater parameters transient nature along the Neretva coastal aquifers system. Besides three fundamentally different subareas inspection as evidenced along the Results section, we extend the analysis to strengthen the findings up and empower their significance.

5.1. Active seawater intrusion conditions

Diga area has been determined as a main corridor for the inflow of seawater into the coastal aquifer system. Dominant controlling factors defining the groundwater quality within the shallow unconfined aquifer are the Adriatic Sea and melioration system channel parallel to the shoreline which converges towards the PS Modric intake basin. Insight to the Fig. 17 emphasizes different SWL

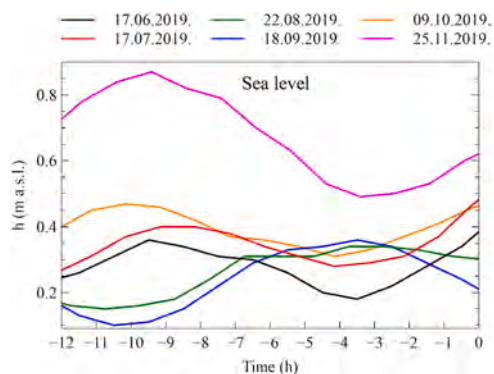


Fig. 17. Sea water level observations 12 h before each GW profile from Fig. 4.

conditions observed prior six in situ profiling performance, not only in the mean SWL but also in the tide occurrence referring to rising or falling tide. By coupling EC profiling results shown in Fig. 7 and SWL features in Fig. 17 it is evident highest EC values are observed during profiling done on June 17th and July 17th 2019 (first and second profiling). Lowest observed EC values at the probe elevation have been observed during September 18th (fourth profiling). Although highest mean SWL has been observed during November 25th (sixth profiling) the latter did not lead to highest observed EC in P1. Those features suggest it is not the mean SWL the factor which controls the EC at Diga groundwater in shallow aquifer. Although the micro tidal features characterizing the area of interest, tidal changes define the inflow of the seawater volume into the coastal system and thus define EC regime (Fadili et al., 2018; Levanon et al., 2017, 2013). During profiling on June 17th and July 17th 2019, a rising tide has been observed with start noticed 3–4 h prior profiling has been done. The time difference between the change of the tide from falling to rising and observed EC shows similarity with time lags observed from coherence analysis (Fig. 6b). Due to the relative ratio between Diga GWL and SWL in this area SWI is classified as the active (Badaruddin et al., 2017) emphasizing the role of SWL in the definition of GWL regime.

5.2. Benefits from frequency domain methods application

Although time-domain models such as the cross-correlation have been shown to be successful in identifying and interpreting processes controlling SWI (Miyakoshi et al., 2020; Vallejos et al., 2014; Zhang et al., 2020), observed time series containing noise can lead to incorrect conclusions. In Fig. 18 a cross-correlation model was applied to GWL and EC time series observed in P1 and SWL time series. To perform a cross-correlation analysis, observed time series are divided into four day periods. For each four day period, pre assumed dependent time series are shifted for one hour repeatedly unless maximum cross-correlation value and appropriate time lag are determined. Signal with enhanced periodicity and low noise (GWL in P1) showed significant cross-correlation with SWL being late between 1 and 3 h, which is consistent with the coherence model results. Signal characterized by high noise (EC) showed negligible correlation with SWL. In addition, the cross-correlation between EC in P1 and SWL showed the time lag varied strongly compared to the coherence model obtained time lag of EC relative to SWL. Hereby, the capacity of the frequency domain methods or strictly the coherence is shown to be superior over time-domain methods in the time lag definition between two observed signals.

Main potential limitation hereby stems from the methodological approach used. Since the presented method based on DFT necessitates division of obtained time series into a finite number of screens and windows, it is unsuitable for analysing short time series. In this study, the screen and window sizes are determined by the characteristics and lengths of the obtained time series. In order to apply this methodology to a different region and different signals, a screen and window size analysis must be performed and selected based on the observed signals' characteristics and lengths (A. Appendix).

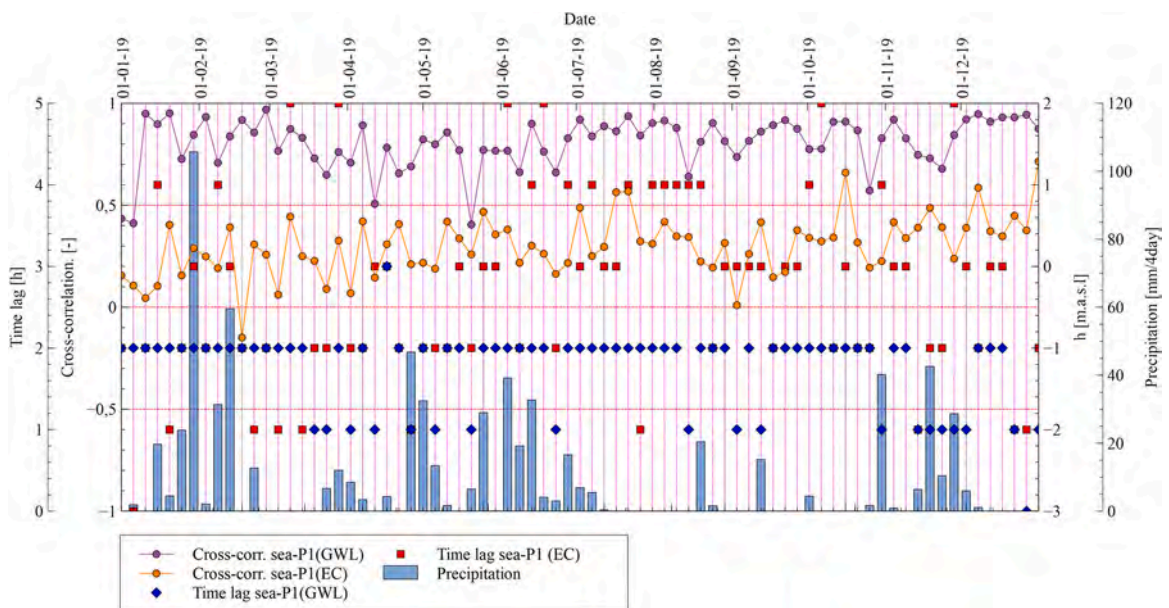


Fig. 18. Cross-correlation analysis of four day periods over the year 2019.

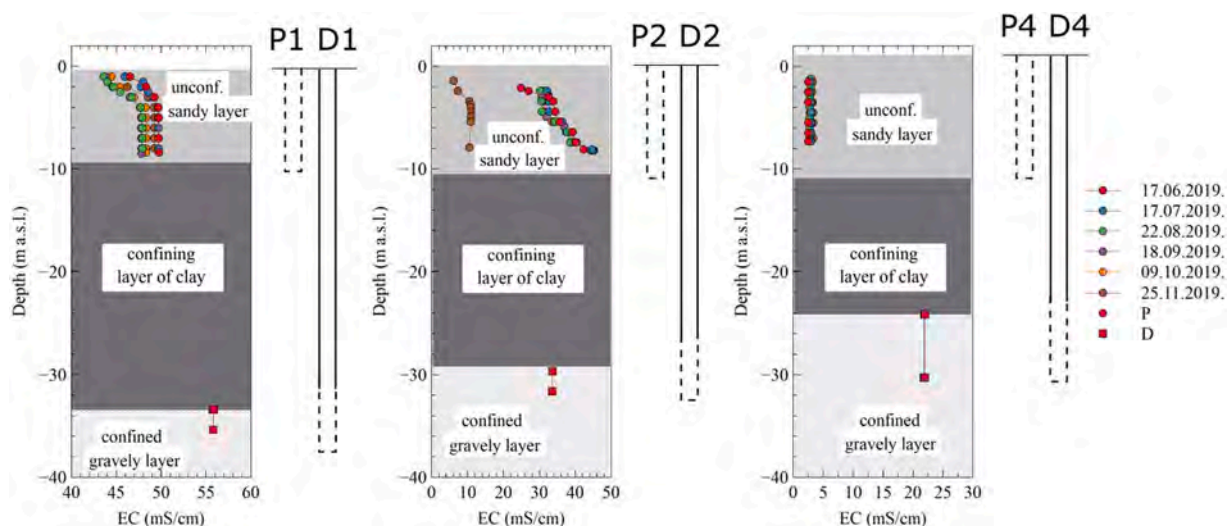


Fig. 19. EC profiling results observed during 2019. for unconfined and confined aquifers at the location of piezometers P1, P2 and P4 and D1, D2 and D4.

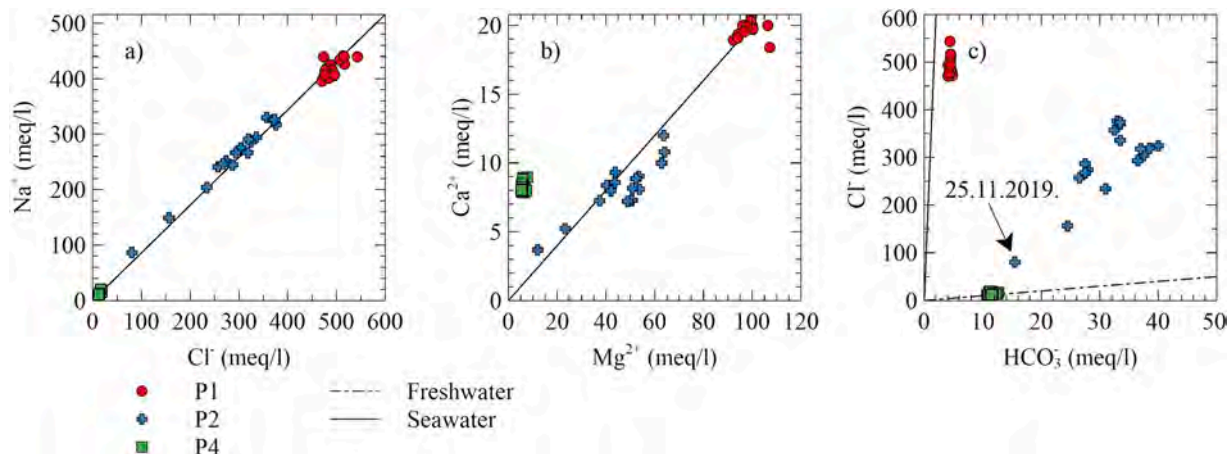


Fig. 20. Relationship (ionic ratio) between a) concentrations of Na and Cl, b) Ca and Mg and c) Cl and HCO₃ for the studied water samples in P1, P2 and P4. Freshwater and seawater theoretical mixing lines are theoretical lines used to explain the relation of the groundwater chemistry to surface water origins.

Table 2
Average ionic ratio of all groundwater samples from boreholes P1, P2 and P4 for the period from 2019–2021.

| | P1 | P2 | P4 |
|---------------------|--------|------|------|
| Na/Cl | 0.85 | 0.90 | 0.87 |
| Ca/Mg | 0.20 | 0.19 | 1.42 |
| Cl/HCO ₃ | 110.96 | 9.09 | 1.20 |

5.3. The source of seawater in an unconfined aquifer

To distinguish the confined aquifer as a source of SWI through the leakage we follow the outcomes of work by Srzić et al. (2020). Hydrogeological characterization of the area of interest lead towards negligible leakage between confined and unconfined layers based on Tidal methods application. Application of method by (Rahi and Halihan, 2013) confirmed the confinement of deep aquifer following the ratio of amplitude spectrum of diurnal and semidiurnal lunar and solar constituents. First order data to confirm the existence of compact clay layer have been performed from the borehole drilled during 2022 at the Opuzen use area. The clay layer has been evidenced with overall depth of 14 m and average hydraulic conductivity equals to $3.36 \cdot 10^{-10} \text{ m s}^{-1}$ (Geokon-Zagreb d.d.,

Table 3

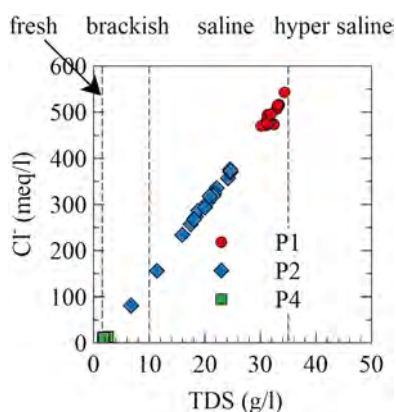
Pearson correlation coefficients of major parameters in groundwater samples as taken from D1, D2 and D4.

| | Na ⁺ | K ⁺ | Mg ²⁺ | Ca ²⁺ | Cl ⁻ | HCO ₃ | SO ₄ ²⁻ | EC | TDS |
|-------------------------------|-----------------|----------------|------------------|------------------|-----------------|------------------|-------------------------------|-------|-------|
| Na ⁺ | 1,000 | | | | | | | | |
| K ⁺ | 0,997 | 1,000 | | | | | | | |
| Mg ²⁺ | 0,982 | 0,981 | 1,000 | | | | | | |
| Ca ²⁺ | 0,808 | 0,807 | 0,898 | 1,000 | | | | | |
| Cl ⁻ | 0,998 | 0,996 | 0,987 | 0,828 | 1,000 | | | | |
| HCO ₃ | -0,078 | -0,081 | -0,247 | -0,617 | -0,108 | 1,000 | | | |
| SO ₄ ²⁻ | 0,811 | 0,818 | 0,899 | 0,964 | 0,826 | -0,622 | 1,000 | | |
| EC | 0,999 | 0,998 | 0,982 | 0,807 | 0,998 | -0,074 | 0,811 | 1,000 | |
| TDS | 0,999 | 0,997 | 0,989 | 0,832 | 0,999 | -0,117 | 0,834 | 0,998 | 1,000 |

Table 4

Pearson correlation coefficients of major parameters in groundwater samples as taken from P1, P2 and P4.

| | Na ⁺ | K ⁺ | Mg ²⁺ | Ca ²⁺ | Cl ⁻ | HCO ₃ | SO ₄ ²⁻ | EC | TDS |
|-------------------------------|-----------------|----------------|------------------|------------------|-----------------|------------------|-------------------------------|-------|-------|
| Na ⁺ | 1,000 | | | | | | | | |
| K ⁺ | 0,980 | 1,000 | | | | | | | |
| Mg ²⁺ | 0,927 | 0,868 | 1,000 | | | | | | |
| Ca ²⁺ | 0,955 | 0,905 | 0,985 | 1,000 | | | | | |
| Cl ⁻ | 0,992 | 0,970 | 0,943 | 0,966 | 1,000 | | | | |
| HCO ₃ | -0,745 | -0,780 | -0,533 | -0,650 | -0,727 | 1,000 | | | |
| SO ₄ ²⁻ | 0,910 | 0,860 | 0,974 | 0,978 | 0,933 | -0,601 | 1,000 | | |
| EC | 0,994 | 0,974 | 0,943 | 0,966 | 0,998 | -0,730 | 0,930 | 1,000 | |
| TDS | 0,993 | 0,964 | 0,960 | 0,978 | 0,997 | -0,704 | 0,947 | 0,997 | 1,000 |

**Fig. 21.** Relationship (ratio) between concentrations of Cl and TDS for the studied water samples in P1, P2 and P4.

2022). Inspection of EC profiling as observed within D2 (33.62 mS cm⁻¹) and P2 (44.30 mS cm⁻¹) piezometers reflects higher EC values within P2 during dry period (Fig. 19). The only difference from the latter is observed during rain period, as a result of profiling performed on November 25th.

As presented from the work by (Krvavica et al., 2021; Krvavica and Ružić, 2020), river Neretva discharge plays dominant role in the definition of the river water column salinity distribution. Unless during dry season, when the discharge takes values usually less than 200 m³ s⁻¹, river Neretva shows stratification in the salinity, increase in the discharge leads towards the salinity stratification diminishing. Taking into consideration discharge values during the period prior the profiling on November 25th has been performed, one can see the discharge value exceeded 1100 m³ s⁻¹ (Fig. 9) which means river Neretva was represented as a fresh water boundary condition which caused the refreshment of the aquifer.

To gain a deeper understanding of the salinization processes in an unconfined aquifer a total of 17 samples have been taken per piezometer from 2019 to 2021 from the depth of approximately 9 m beneath the ground level. Samples have been taken from piezometer with SEBA KLL water sampler. In all samples, the concentration of major ions is determined in the laboratory, and the values of each major ion are expressed in meq l⁻¹. Each sample's ionic charge balance error is less than five percent, which is considered an acceptable error level (Najib et al., 2017). The ionic ratios of borehole samples are plotted in Fig. 20a-c. Also the average ratio between the ions presented in Fig. 20a-c is calculated for each piezometer (Table 2).

The Na/Cl ratios are close to 0.86 in all three piezometers (Table 2), and the ratios of Na/Cl from all samples are located on the standard seawater-freshwater mixing line (Fig. 20a) indicating the dominance of SWI (Jiao and Post, 2019). The similarity between P1

and P2's Ca/Mg ratios, 0.19 and 0.20 (Table 2, Fig. 20b), can be explained by the presence of seawater. Since the Ca/Mg ratio in seawater ranges from just below 0.2 up to 0.22 (Jiao and Post, 2019), the lower Ca/Mg ratio in P1 and P2 in some water samples can be attributed to evaporation (Jiao and Post, 2019). The Ca/Mg ratio in P4 is 1.42 (Table 2), which is the typical value of Ca/Mg in limestone aquifers (Jiao and Post, 2019). The Cl/HCO₃ is often used as indicator of groundwater contamination with seawater (Al-Khatib and Al-Najar, 2011). The Cl/HCO₃ ratio (Fig. 20c, Table 2) indicate Diga and Jasenska area are strongly affected by SWI (Cl/HCO₃ > 6.6), while Vidrice area is moderately affected by SWI (6.6 > Cl/HCO₃ > 0.5) (Al-Khatib and Al-Najar, 2011; Jiao and Post, 2019). It is also important to notice lowest Cl/HCO₃ ratio in P2 is observed on November 25th 2019 (Fig. 20c) after the significant precipitation occurred indicating the refreshment of the Jasenska area.

Additionally, separate correlation matrices are computed for unconfined and confined aquifers. Except for HCO₃, there is a significant correlation between all major ions in both tables, indicating both unconfined and confined aquifers derive their salinity from the same source (Bouderbala, 2015). The significant correlation between Cl⁻ and Na⁺, K⁺, Mg²⁺, and Ca²⁺ suggests seawater is the primary source of salinization in both aquifers (Kharroubi et al., 2012; Qin et al., 2013). Tables 3 and 4.

Given the palaeo-seawater can significantly salinize coastal aquifers as it has been evidenced worldwide (Carol et al., 2021; Dang et al., 2022; Delsman et al., 2014; Giambastiani et al., 2013; Goebel et al., 2017; Shi and Jiao, 2014; Vallejos et al., 2018; van Engelen et al., 2018), potential sources of seawater as found along the coastal aquifer systems are crucial to be distinguished and identified.

The identification of palaeo-seawater can be determined by developing a palaeo numerical model of the study area with variable boundary conditions that follow marine transgression and regression during the past (Delsman et al., 2014; van Engelen et al., 2018), by geophysical investigations (Goebel et al., 2017) and by hydrogeochemical and isotopic analysis of groundwater samples (Dang et al., 2022; Frollini et al., 2022; Giambastiani et al., 2013). Very often, the palaeo-seawater shows hypersalinity compared to present seawater (Chang et al., 2022; Dang et al., 2022; Giambastiani et al., 2013; Jiao and Post, 2019; Vallejos et al., 2018) which makes them easily identified.

Cl⁻ and TDS values for each groundwater sample from the Neretva valley unconfined aquifer are plotted in Fig. 21. According to the TDS values, four classifications of samples were made: i) freshwater with TDS values between 0 and 1.5 g l⁻¹, ii) brackish water with TDS values between 1.5 and 10 g l⁻¹, iii) saline water with TDS values between 10 and 35 g l⁻¹, and iv) hypersaline water with TDS values greater than 35 g l⁻¹. The upper limit of 35 g l⁻¹ for saline water is taken as present seawater has TDS value around 35 g l⁻¹ (Giambastiani et al., 2013). Groundwater samples from P4 correspond to brackish water with TDS values between 1.62 and 2.57 g l⁻¹, while samples from P2 correspond to brackish and saline water with TDS values between 6.71 and 24.63 g l⁻¹ (Fig. 21). All samples from the P1 piezometer correspond to the saline water with TDS values between 30.14 and 34.33 g l⁻¹ (Fig. 21). Two potential facts can explain the absence of hypersaline water in a Neretva system unconfined aquifer (Fig. 21): first, potential palaeo-seawater has been washed out from the aquifer, and second, groundwater samples contain a mixture of different sources of salinity and freshwater, thus leading the TDS concentration to be below the present seawater.

The identification of palaeo-seawater has been the subject of research at numerous coastal aquifer locations (Carol et al., 2021; Delsman et al., 2014; Giambastiani et al., 2013; Goebel et al., 2017; Vallejos et al., 2018). Delsman et al. (2014) emphasized the significance of using a palaeo-hydrogeological model to determine the present salinity of a coastal aquifer, as opposed to a steady-state model with present-day boundary conditions. Goebel et al. (2017) demonstrated the ability of electrical resistivity tomography to identify palaeo-seawater in the deeper aquifer along the coast of Monterey. The studies based on isotopic analysis (Carol et al., 2021; Giambastiani et al., 2013; Vallejos et al., 2018) demonstrated the paleo-seawater has a substantial impact on the salinization of coastal aquifers. Same studies demonstrated groundwater samples are frequently a mixture of different salinity and freshwater sources, leading to the fact paleo-seawater can be present in both shallow and deep aquifers.

Compared to the evidence of Holocene paleo-seawater found within the shallow aquifer in the study by Vallejos et al. (2018), no deterministic evidence of the palaeo-seawater has been determined in the Neretva system shallow aquifer. As a dominant source of P2 EC change (e.g. salinity), hereby we highlight the interplay between the river Neretva salinity regime and channel Jasenska regime (Lovrinović et al., 2022). The main contributing factor relies in the decrease of the EC as observed within the P2 on November 25th 2019, induced by rapid increase in the river Neretva discharge and thus freshening of the Neretva water column (Fig. 12a). The latter implies lateral seawater inflow as a mechanism contributing to the groundwater salinity, rather than the Holocene palaeo-seawater.

However, to fully understand the processes and sources of salinization of groundwater found within the shallow aquifer, as well as the potential sources of palaeo-seawater, interplay and contribution to observed salinity in the entire Neretva valley coastal aquifer, a comprehensive geochemical and isotopic analysis of groundwater samples are necessary and deserves further investigation.

5.4. Salinization of melioration sub system Vidrice

In the geological research performed along this area (Geokon-Zagreb d.d., 2022), several upcoming salt springs have been found. Therefore, with the occurrence of precipitation, firstly the brackish water from the springs is washed out towards PS Prag basin, as it is the converging point of the area driven by the low water level induced by PS Prag operative regime, which consequently leads to EC increase in P4. A similar phenomenon has been observed in the study of Yang et al. (2020), where EC in one of the piezometers increased with precipitation. The coherence results do not suggest EC in P4 is influenced by either the operating regime of PS Prag or the Mala Neretva water elevation although the proximity to both.

Indicative confirmation of springs contribution to increased EC in P4 especially during precipitation occurrence has been reached through the profiling and sampling of surface water at predetermined locations along the intake channel of the PS Prag. Subsequent determination of the EC has been performed in-situ and under controlled environment laboratory conditions. During dry and rain

Table 5

EC values obtained in laboratory conditions from surface water samples taken along the Vidrice area.

| Date | 25.05.2021. | 29.06.2021. | 09.11.2021. | 15.12.2021. |
|-----------------------------|-------------|-------------|-------------|-------------|
| SW_1 (mS cm ⁻¹) | 9.53 | 6.7 | 11.22 | 9.06 |
| SW_2 (mS cm ⁻¹) | 4.6 | 3.2 | 6.02 | 4.95 |

periods, four surface water samples are collected during 2021. Inspection of EC values shown in Table 5, discover greater EC values as obtained from the samples taken near the upcoming springs (SW_1) than near the PS Prag (SW_2) during both dry and rain periods. It is also important to note EC values are higher during the rain season than during the dry season.

6. Conclusions

This paper deals with the definition of the external parameters and mechanisms influencing SWI and defining groundwater parameters, respectively GWL, EC and T in river Neretva coastal aquifer system consisted of shallow unconfined aquifer, confining clay layer and confined aquifer. The work relies on three sources: i) time series observed through the implemented monitoring system and ii) profilings performed in-situ, their analysis by application of DFT spectrogram and coherence features analysis and iii) major ion geochemical analysis and indicators. Besides the general conclusion, three different sub areas along the melioration systems Opuzen usce and Vidrice show fundamentally different conditions and circumstances, below we highlight main findings arose from the presented work:

- Diga area representing the embankment delineating Opuzen usce area and the Adriatic Sea represent main corridor for the SWI penetrating Neretva coastal system. Due to the operation of the melioration system, mean groundwater level as found within the shallow unconfined aquifer is found below the mean SWL. This uniquely leads to active SWI conditions resulting in continuous inflow of the seawater to the inland. This 2200 m long barrier between mouth of river Neretva and river Mala Neretva presents a long term corridor for the SWI occurrence into the Neretva coastal system.
- Jasenska area GWL and EC regimes are fundamentally different and should be considered separately. Unless the GWL is balanced by river Neretva water elevation and PS Modric operative regime, EC shows changes reflected on a larger temporal scale. Although the changes in GWL are relatively fast, acting as a response to precipitation induced recharge and the regime of Jasenska melioration channel water elevation, EC shows slower response time scales. Although located 1200 m away from the river Neretva left bed, stratification of the salinity within the Neretva river water column induces the lateral SWI to the inland.
- GWL in P4 characterizing Vidrice melioration subsystem is shown to be fully determined by the operative regime of PS Prag. Although the GWL regime is driven in this way, EC is driven by the features of brackish upcoming springs found along the southern border of the Vidrice area where karstic hills exceed ground level. Due to the fact the ground level found along this area is strictly beneath the mean sea level and fractured karstic massive found between the Adriatic Sea and Vidrice area, pathways for the seawater to feed the springs are enabled.
- Inspection of major ion geochemical analysis leads towards the conclusion the origin of the salinity of the GW within the shallow unconfined aquifer stems from the SWI. The latter is also supported by the fact of active SWI presence due to the lower GWL relative to mean sea level.
- Unless the features of groundwater as found within the shallow unconfined aquifer show sensitivity to external loadings and local circumstances referring to hydrological conditions, tidal features and pumping stations operative regimes, confined aquifer shows stability in EC. The latter is evidenced through similar result obtained in different periods of the hydrological year. Although the piezometric head of the confined aquifer is shown to be dominantly determined by the SWL (Srzić et al., 2020) EC does not behave in the same manner as evidenced from our study.

Funding

This research is funded by the contribution from the EU co-financing and the Interreg Italy-Croatia CBC Programme 2014–2020 Restricted call (Priority Axes: Safety and Resilience) through the European Regional Development Fund as a part of project Saltwater intrusion and climate change: monitoring, countermeasures and informed governance (SeCure) (PID: 10419304). Furthermore, this research is partially supported through project KK.01.1.1.02.0027, a project co-financed by the Croatian Government and the European Union through the European Regional Development Fund–the Competitiveness and Cohesion Operational Programme, contract number: KK.01.1.1.02.0027.

CRedit authorship contribution statement

Ivan Lovrinović: Data curation, Formal analysis, Investigation, Methodology, Visualization, Validation, Conceptualization, Writing - original draft, Writing - review & editing. **Veljko Srzić:** Funding acquisition, Investigation, Methodology, Supervision, Validation, Conceptualization, Data curation, Writing - original draft, Writing - review & editing. **Iva Aljinović:** Data curation, Formal analysis, Investigation, Validation, Methodology, Visualization, Writing - review & editing.

Declaration of Competing Interest

The authors declare that they have no known competing financial interests or personal relationships that could have appeared to influence the work reported in this paper.

Data availability

Field data, including time series and profiling data input files are available on request.

Appendix A

To ensure the relevance of the results arose from the spectrogram and coherence analysis, an additional screen size and window size sensitivity analysis has been performed. As a representative, PS Prag water level and P4 GWL were selected for further analysis because the fact the GWL in P4 contains periodic oscillations from PS Prag and non-periodic oscillations caused by precipitation.

The sensitivity of spectrograms and coherence models to window size is shown in Fig. A1. The screen size of 30 days is used in all spectrograms and coherence models shown in Fig. A1. Window sizes of 5, 10, 15, and 20 days, respectively, were used to demonstrate the effect of window size on the results. It can be seen that the window size affects the spectrogram and coherence results differently. Increasing the window size results in sharper spectrograms. Welch’s method has been shown to compute ASD effectively even when

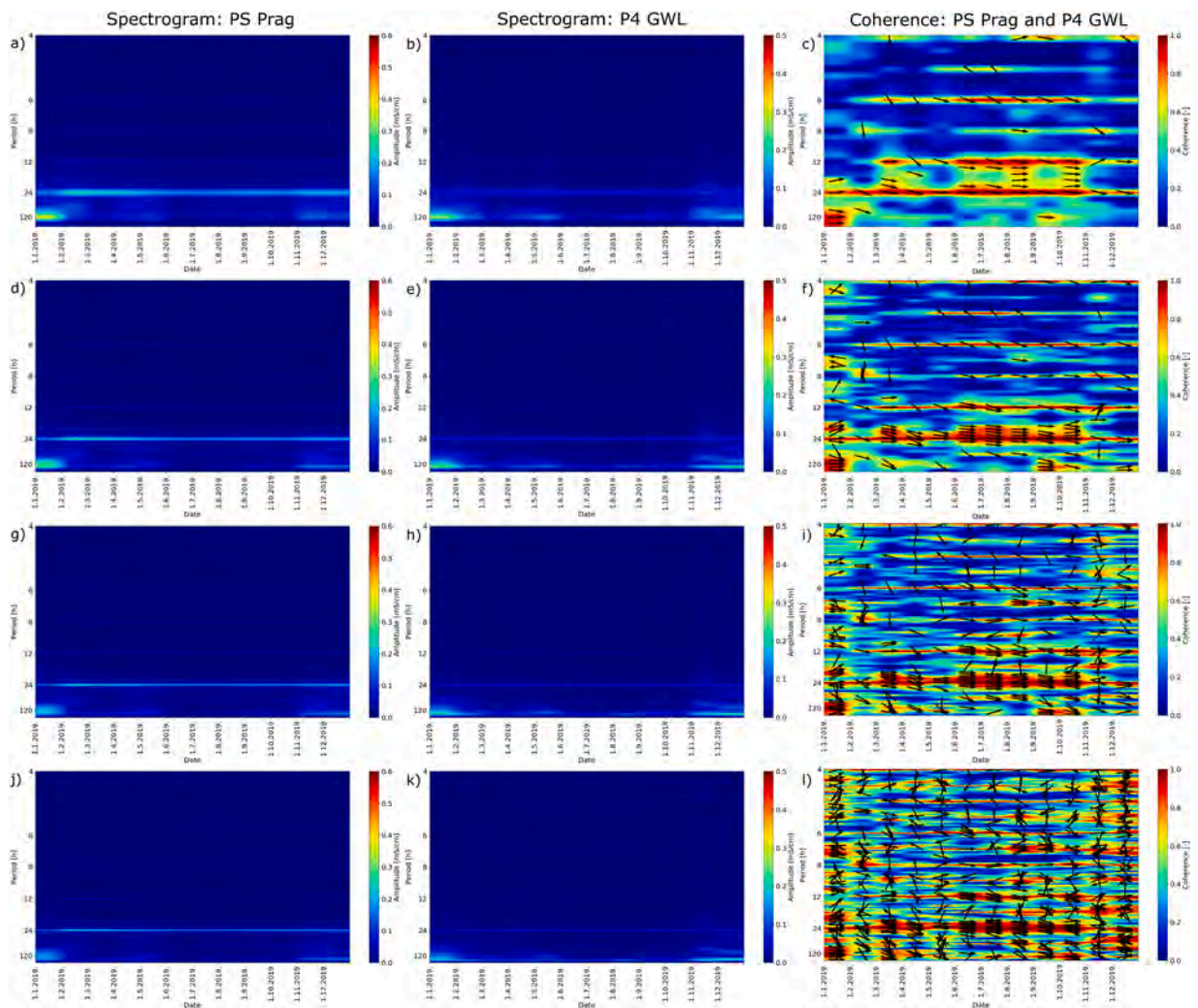


Fig. A1. Spectrogram of PS Prag with a) screen 30d, window 5d; d) screen 30d, window 10d; g) screen 30d, window 15d; j) screen 30d, window 20d; Spectrogram of P4 GWL with b) screen 30d, window 5d; e) screen 30d, window 10d; h) screen 30d, window 15d; k) screen 30d, window 20d; Coherence model between PS Prag and P4 GWL with c) screen 30d, window 5d; f) screen 30d, window 10d; i) screen 30d, window 15d; l) screen 30d, window 20d.

Table A1

Overview of the screen and window size taken into consideration for sensitivity analysis.

| Screen and window size | Number of data in window | number of screens during year | window overlap size | Number of windows in screen |
|------------------------|--------------------------|-------------------------------|---------------------|-----------------------------|
| 30[d] 5[d] | 120 | 12 | 110 | 60 |
| 30[d] 10[d] | 240 | 12 | 220 | 24 |
| 30[d] 15[d] | 360 | 12 | 330 | 12 |
| 30[d] 20[d] | 480 | 12 | 440 | 6 |
| 20[d] 5[d] | 120 | 18 | 110 | 36 |
| 15[d] 5[d] | 120 | 24 | 110 | 24 |
| 10[d] 5[d] | 120 | 36 | 110 | 12 |

the number of windows in the screen is reduced to 6 (Fig. A1j and k). As mentioned earlier, increasing the window size increases the number of frequencies in the frequency domain. These frequencies represent usually noise, while the number of frequencies with significant amplitude increases slightly e.g. diurnal constituent in sea level with the increase of window size will separate to lunar diurnal constituents K1 and O1. Increasing the window size also results in the window being placed over a screen less often. Therefore, for a screen size of 30 days and a window size of 5 days, 60 times CPSD is calculated for each frequency. For a screen size of 30 days and a window size of 20 days, CPSD is calculated only 6 times (Table A1), which shows the interpretation reliability of the coherence results decreases as the window size increases. For window sizes of 15 and 20 days, the number of noise frequencies at which significant coherence is calculated increases as CPSD is calculated less often.

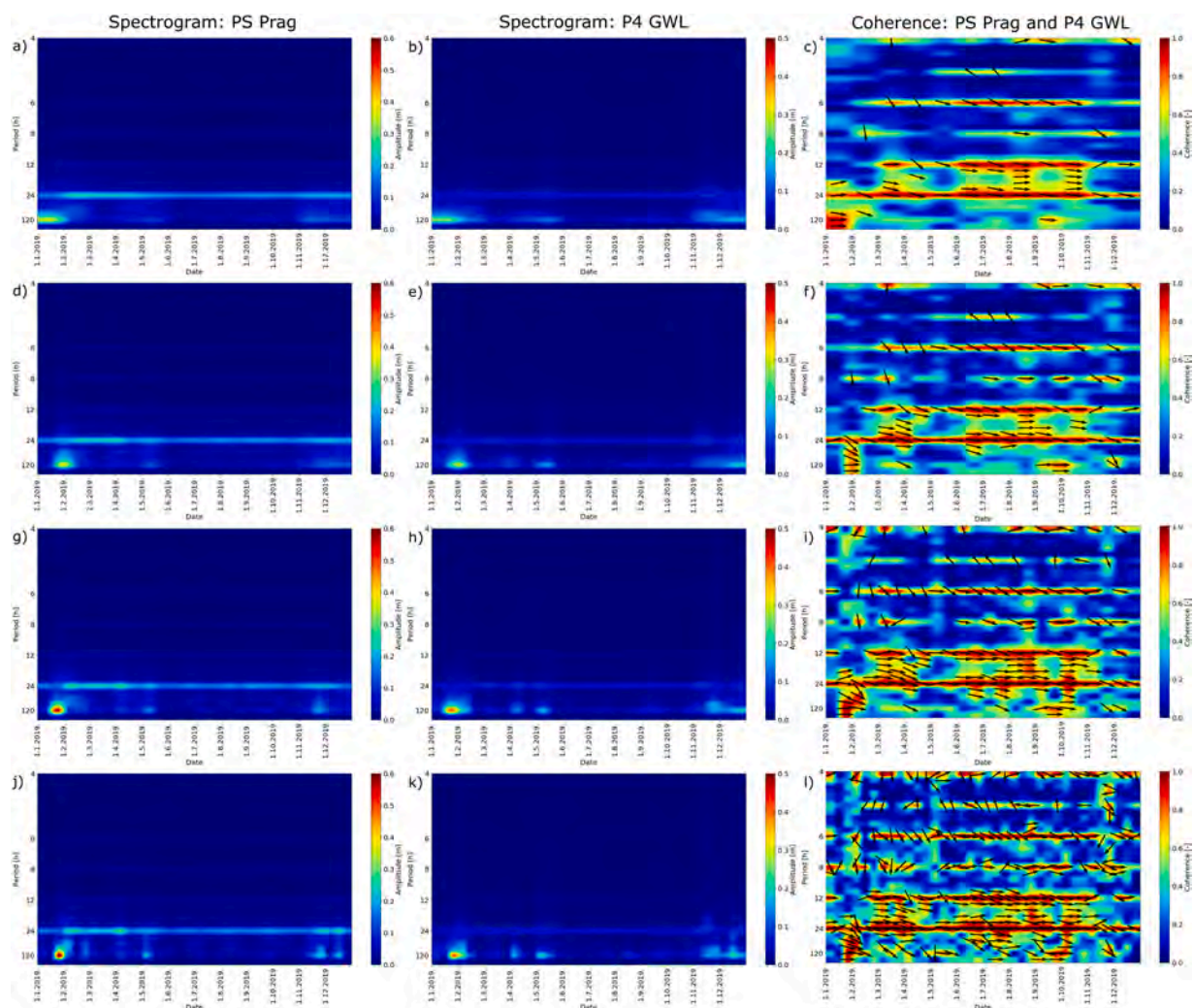


Fig. A2. Spectrogram of PS Prag with a) screen 30d, window 5d; d) screen 20d, window 5d; g) screen 15d, window 5d; j) screen 10d, window 5d; Spectrogram of P4 GWL with b) screen 30d, window 5d; e) screen 20d, window 5d; h) screen 15d, window 5d; k) screen 10d, window 5d; Coherence model between P4 GWL and PS Prag with c) screen 30d, window 5d; f) screen 20d, window 5d; i) screen 15d, window 5d; l) screen 10d, window 5d.

Additional clarification of spectrogram and coherence model results was tested with different screen sizes, 10, 15, 20, and 30 days respectively, while the window size was set constant (5 days). The variation in screen size means that the number of times ASD is recorded in the spectrogram changes over analysed period. For example, a screen size of 30 days has 12 periods when ASD is recorded, while the screen size of 10 days has 36 periods when ASD or coherence is recorded (Table A1). The smaller the difference between screen size and window size is, the less reliable the coherence results will be. Spectrograms with larger screen size have lower ability to detect non-periodic events of precipitation because these events last for a day or more and do not occur in every window found within larger screens. Fig. A2 a and b with a screen size of 30 days show no precipitation effect in May, while with the reduction of the screen amplitudes corresponding to the precipitation effect start to dominate. The same effect is seen for all periods with precipitation occurrence. Spectrograms with screen sizes of 10 and 15 days show higher amplitudes in the frequencies corresponding to the trend change due to precipitation than spectrograms with screen size of 20 and 30 days. A similar effect of precipitation is seen in the coherence models in Fig. A2 where the coherence model with a screen size of 30 days (Fig. A2 c) has the lowest ability to capture non-periodic events. Fig. A2l, where the screen size is 10 days, has shown the highest ability to describe non-periodic events. The coherence model with a screen size of 10 days has only 12 windows per screen, which also makes it the lowest reliable among the models examined in Fig. A2.

Taking into account above mentioned effects of screen and window sizes on the spectrogram and coherence model results, and considering the reliability of the coherence results due to the number of calculated CPSD in the coherence, a screen size of 15 days and a window size of 5 days were selected as relevant for the purpose of this paper.

Appendix B. Supporting information

Supplementary data associated with this article can be found in the online version at [doi:10.1016/j.ejrh.2023.101363](https://doi.org/10.1016/j.ejrh.2023.101363).

References

- Abd-Elaty, I., Zelenakova, M., 2022. Saltwater intrusion management in shallow and deep coastal aquifers for high aridity regions. *J. Hydrol. Reg. Stud.* 40, 101026 <https://doi.org/10.1016/j.ejrh.2022.101026>.
- Al-Khatib, M., Al-Najar, H., 2011. Hydro-geochemical characteristics of groundwater beneath the Gaza Strip. *J. Water Resour. Prot.* 3, 341–348. <https://doi.org/10.4236/jwarp.2011.35043>.
- Argamasilla, M., Barberá, J.A., Andreo, B., 2017. Factors controlling groundwater salinization and hydrogeochemical processes in coastal aquifers from southern Spain. *Sci. Total Environ.* 580, 50–68. <https://doi.org/10.1016/j.scitotenv.2016.11.173>.
- Badaruddin, S., Werner, A.D., Morgan, L.K., 2015. Water table salinization due to seawater intrusion. *Water Resour. Res.* 51, 8397–8408. <https://doi.org/10.1002/2015WR017098>.
- Badaruddin, S., Werner, A.D., Morgan, L.K., 2017. Characteristics of active seawater intrusion. *J. Hydrol.* 551, 632–647. <https://doi.org/10.1016/j.jhydrol.2017.04.031>.
- Behera, A.K., Chakrapani, G.J., Kumar, S., Rai, N., 2019. Identification of seawater intrusion signatures through geochemical evolution of groundwater: a case study based on coastal region of the Mahanadi delta, Bay of Bengal, India. *Nat. Hazards* 97, 1209–1230. <https://doi.org/10.1007/s11069-019-03700-6>.
- Bouderbala, A., 2015. Groundwater salinization in semi-arid zones: an example from Nador plain (Tipaza, Algeria). *Environ. Earth Sci.* 73, 5479–5496. <https://doi.org/10.1007/s12665-014-3801-9>.
- Briciu, A.E., 2019. Changes in physical properties of inland streamwaters induced by earth and atmospheric tides. *Water* 11. <https://doi.org/10.3390/w1122533>.
- Carol, E., Perdomo, S., Álvarez, M.D., Tanjal, C., Bouza, P., 2021. Hydrochemical, isotopic, and geophysical studies applied to the evaluation of groundwater salinization processes in quaternary beach ridges in a semiarid coastal area of Northern Patagonia, Argentina. *Water* 13. <https://doi.org/10.3390/w13243509>.
- Chang, Y., Chen, X., Guan, Q., Tian, C., Liu, D., Xu, D., 2022. Study on the sources of salinity of groundwater in holocene and late pleistocene sediments based on hydrochemical and isotopic methods in Southern Laizhou Bay. *Water* 14. <https://doi.org/10.3390/w14172761>.
- Cooley, J.W., Lewis, P.A.W., Welch, P.D., 1969. The fast Fourier transform and its applications. *IEEE Trans. Educ.* 12, 27–34. <https://doi.org/10.1109/TE.1969.4320436>.
- Custodio, E., 2010. Coastal aquifers of Europe: an overview. *Hydrogeol. J.* 18, 269–280. <https://doi.org/10.1007/s10040-009-0496-1>.
- Da, C., Carol, E., Kruse, E., Teatini, P., Tosi, L., Da Lio, C., Carol, E., Kruse, E., Teatini, P., Tosi, L., 2015. Saltwater contamination in the managed low-lying farmland of the Venice coast, Italy: an assessment of vulnerability. *Sci. Total Environ.* 533, 356–369. <https://doi.org/10.1016/j.scitotenv.2015.07.013>.
- Dang, X., Gao, M., Wen, Z., Hou, G., Jakada, H., Ayejoto, D., Sun, Q., 2022. Saline groundwater evolution in the Luanhe River delta (China) during the Holocene: hydrochemical, isotopic, and sedimentary evidence. *Hydrol. Earth Syst. Sci.* 26, 1341–1356. <https://doi.org/10.5194/hess-26-1341-2022>.
- Delsman, J.R., Hu-a-ng, K.R.M., Vos, P.C., de Louw, P.G.B., Oude Essink, G.H.P., Stuyfzand, P.J., Bierkens, M.F.P., 2014. Paleo-modeling of coastal saltwater intrusion during the Holocene: an application to the Netherlands. *Hydrol. Earth Syst. Sci.* 18, 3891–3905. <https://doi.org/10.5194/hess-18-3891-2014>.
- de Oliveira Gomes, O.V., Marques, E.D., Kütter, V.T., Aires, J.R., Travi, Y., Silva-Filho, E.V., Gomes, O.V.O.O., Marques, E.D., Kütter, V.T., Aires, J.R., Travi, Y., Silva-Filho, E.V., 2019. Origin of salinity and hydrogeochemical features of porous aquifers from northeastern Guanabara Bay, Rio de Janeiro, SE - Brazil. *J. Hydrol. Reg. Stud.* 22, 100601 <https://doi.org/10.1016/j.ejrh.2019.100601>.
- Dibaj, M., Javadi, A.A., Akrami, M., Ke, K.-Y., Farmani, R., Tan, Y.-C., Chen, A.S., 2021. Coupled three-dimensional modelling of groundwater-surface water interactions for management of seawater intrusion in Pingtung Plain, Taiwan. *J. Hydrol. Reg. Stud.* 36, 100850 <https://doi.org/10.1016/j.ejrh.2021.100850>.
- Dong, L., Shimada, J., Kagabu, M., Yang, H., 2015. Barometric and tidal-induced aquifer water level fluctuation near the Ariake Sea. *Environ. Monit. Assess.* 187. <https://doi.org/10.1007/s10661-014-4187-6>.
- Elektrosond Zagreb, 1962. Grain-size Distribution Curves Opuzen - Mouth of Neretva.
- Elektrosond Zagreb, 1963. Hydrogeological Investigation Works Opuzen - Mouth of Neretva.
- Erskine, A.D., 1991. The effect of tidal fluctuation on a coastal aquifer in the UK. *Groundwater* 29, 556–562. <https://doi.org/10.1111/j.1745-6584.1991.tb00547.x>.
- Faculty of Civil Engineering, Geodesy and architecture, 2019. Salinity Monitoring at Lower Neretva Area —Report for the year 2019, University of Split.
- Fadili, A., Malaurent, P., Najib, S., Mehdi, K., Riss, J., Makan, A., 2018. Groundwater hydrodynamics and salinity response to oceanic tide in coastal aquifers: case study of Sahel Doukkala, Morocco. *Hydrogeol. J.* 26, 2459–2473. <https://doi.org/10.1007/s10040-018-1812-4>.
- Frollini, E., Parrone, D., Ghergo, S., Masciale, R., Passarella, G., Pennisi, M., Salvadori, M., Preziosi, E., 2022. An integrated approach for investigating the salinity evolution in a Mediterranean Coastal Karst Aquifer. *Water*. <https://doi.org/10.3390/w14111725>.
- Fuentes-Arreazola, M.A., Ramírez-Hernández, J., Vázquez-González, R., 2018. Hydrogeological properties estimation from groundwater level natural fluctuations analysis as a low-cost tool for the Mexicali Valley Aquifer. *Water* 10. <https://doi.org/10.3390/w10050586>.

- Geofizika Zagreb, 1962. Geophysical Investigations /Geoelectrical and Seismic/ at Opuzen - Mouth of Neretva.
- Geofizika Zagreb, 1966. Water Investigation Works at Opuzen – Setka.
- Geoid-Beroš LTD, 2014. Piezometer Drilling for Purpose of Groundwater Monitoring System.
- Geokon-Zagreb d.d, 2005. Drilling Report of Two Pairs of Piezometers Downstream of the Neretva River.
- Geokon-Zagreb d.d, 2008. Geotechnical Investigation Works for Irrigation System Conceptual Design Downstream of the Neretva River.
- Geokon-Zagreb d.d, 2013. Geotechnical Investigation Works for Siphon Below Mala Neretva at the Pumping Station Prag (Vidrice).
- Geokon-Zagreb d.d, 2022. Field and laboratory research service in the Lower Neretva area for the needs of the Project „Monitoring Sea-water intrusion in coastal aquifers and Testing pilot projects for its mitigation. Zagreb.
- Giambastiani, B.M.S., Colombani, N., Mastrocicco, M., Fidelibus, M.D., 2013. Characterization of the lowland coastal aquifer of Comacchio (Ferrara, Italy): hydrology, hydrochemistry and evolution of the system. *J. Hydrol.* 501, 35–44. <https://doi.org/10.1016/j.jhydrol.2013.07.037>.
- Goebel, M., Pidlisecky, A., Knight, R., 2017. Resistivity imaging reveals complex pattern of saltwater intrusion along Monterey coast. *J. Hydrol.* 551, 746–755. <https://doi.org/10.1016/j.jhydrol.2017.02.037>.
- Guo, Q., Li, H., Boufadel, M.C., Xia, Y., Li, G., 2007. Tide-induced groundwater head fluctuation in coastal multi-layered aquifer systems with a submarine outlet-capping. *Adv. Water Resour.* 30, 1746–1755. <https://doi.org/10.1016/j.adwatres.2007.01.003>.
- Hrvatske vode, 2014. Provedbeni plan obrane od poplava branjenog područja sektor f – Južni Jadran branjeno područje 32: područja malih slivova Neretva - Korčula i Dubrovačko primorje i otoci.
- Institute IGH PLC, 2013. Geotechnical Study for Irrigation System Subsystem Opuzen (Phases A and J).
- Institute IGH PLC, 2019. Monitoring Sea-Water Intrusion in Coastal Aquifers and Testing Pilot Projects for its Mitigation, Geophysical Investigation Report.
- Isermann, R., Münchhof, M., 2011. Spectral Analysis Methods for Periodic and Non-Periodic Signals.
- Janeković, I., Kuzmić, M., 2005. Numerical simulation of the Adriatic Sea principal tidal constituents. *Ann. Geophys.* 23, 3207–3218. <https://doi.org/10.5194/angeo-23-3207-2005>.
- Jiao, J., Post, V., 2019. Coastal Hydrogeology. Cambridge University Press, Cambridge. <https://doi.org/10.1017/9781139344142>.
- Jiao, J.J., Tang, Z., 1999. An analytical solution of groundwater response to tidal fluctuation in a leaky confined aquifer. *Water Resour. Res.* 35, 747–751. <https://doi.org/10.1029/1998WR900075>.
- Kayane, I., Taniguchi, M., Sanjo, K., 1985. Alteration of the groundwater thermal regime caused by advection. *Hydrol. Sci. J.* 30, 343–360. <https://doi.org/10.1080/02626668509490998>.
- Ketabchi, H., Mahmoodzadeh, D., Ataie-Ashtiani, B., Simmons, C.T., 2016. Sea-level rise impacts on seawater intrusion in coastal aquifers: review and integration. *J. Hydrol.* 535, 235–255. <https://doi.org/10.1016/j.jhydrol.2016.01.083>.
- Khan, A.F., Srinivasamoorthy, K., Prakash, R., Rabina, C., 2020. Hydrochemical and statistical techniques to decode groundwater geochemical interactions and saline water intrusion along the coastal regions of Tamil Nadu and Puducherry. *India Environ. Geochem. Health* 0. <https://doi.org/10.1007/s10653-020-00713-0>.
- Kharroubi, A., Gzam, M., Jedoui, Y., 2012. Anthropogenic and natural effects on the water and sediments qualities of coastal lagoons: case of the Boughrara Lagoon (Southeast Tunisia). *Environ. Earth Sci.* 67, 1061–1067. <https://doi.org/10.1007/s12665-012-1551-0>.
- Kim, J.H., Lee, J., Cheong, T.J., Kim, R.H., Koh, D.C., Ryu, J.S., Chang, H.W., 2005. Use of time series analysis for the identification of tidal effect on groundwater in the coastal area of Kimje, Korea. *J. Hydrol.* 300, 188–198. <https://doi.org/10.1016/j.jhydrol.2004.06.004>.
- Kim, K.-Y., Chon, C.-M., Park, K.-H., Park, Y.-S., Woo, N.-C., 2008a. Multi-depth monitoring of electrical conductivity and temperature of groundwater at a multi-layered coastal aquifer: Jeju Island, Korea. *Hydrol. Process.* 22, 3724–3733. <https://doi.org/10.1002/hyp.6976>.
- Kim, K.-Y., Chon, C.-M., Park, K.-H., Park, Y.-S., Woo, N.-C., Kue-Young, K., Chul-Min, C., Ki-Hwa, P., Yun-Seok, P., Nam-Chil, W., 2008b. Multi-depth monitoring of electrical conductivity and temperature of groundwater at a multilayered coastal aquifer: Jeju Island, Korea. *Hydrol. Process.* 22, 3724–3733. <https://doi.org/10.1002/hyp.6976>.
- Kim, K.-Y.Y., Seong, H., Kim, T., Park, K.-H.H., Woo, N.-C.C., Park, Y.-S.S., Koh, G.-W.W., Park, W.-B.B., 2006. Tidal effects on variations of fresh–saltwater interface and groundwater flow in a multilayered coastal aquifer on a volcanic island (Jeju Island, Korea). *J. Hydrol.* 330, 525–542. <https://doi.org/10.1016/j.jhydrol.2006.04.022>.
- Krvavica, N., Ružić, I., 2020. Assessment of sea-level rise impacts on salt-wedge intrusion in idealized and Neretva River Estuary. *Estuar. Coast. Shelf Sci.* 234, 106638. <https://doi.org/10.1016/j.ecss.2020.106638>.
- Krvavica, N., Gotovac, H., Lončar, G., 2021. Salt-wedge dynamics in microtidal Neretva River estuary. *Reg. Stud. Mar. Sci.* 43, 101713. <https://doi.org/10.1016/j.rsm.2021.101713>.
- Kuan, W.K., Xin, P., Jin, G., Robinson, C.E., Gibbs, B., Li, L., 2019. Combined effect of tides and varying inland groundwater input on flow and salinity distribution in unconfined coastal aquifers. *Water Resour. Res.* 55, 8864–8880. <https://doi.org/10.1029/2018WR024492>.
- Levanon, E., Gvirtzman, H., Yechieli, Y., Oz, I., Ben-Zur, E., Shalev, E., 2019. The dynamics of sea tide-induced fluctuations of groundwater level and freshwater-saltwater interface in coastal aquifers: laboratory experiments and numerical modeling. *Geofluids* 2019. <https://doi.org/10.1155/2019/6193134>.
- Levanon, E., Yechieli, Y., Gvirtzman, H., Shalev, E., 2017. Tide-induced fluctuations of salinity and groundwater level in unconfined aquifers – Field measurements and numerical model. *J. Hydrol.* 551, 665–675. <https://doi.org/10.1016/j.jhydrol.2016.12.045>.
- Levanon, E., Yechieli, Y., Shalev, E., Friedman, V., Gvirtzman, H., 2013. Reliable monitoring of the transition zone between fresh and saline waters in coastal aquifers. *Groundw. Monit. Remediat.* 33, 101–110. <https://doi.org/10.1111/gwmr.12020>.
- Lovrinović, I., Bergamasco, A., Srzić, V., Cavallina, C., Holjević, D., Donnici, S., Erceg, J., Zaggia, L., Tosi, L., 2021. Groundwater monitoring systems to understand sea water intrusion dynamics in the Mediterranean: the Neretva Valley and the Southern Venice coastal aquifers case studies. *Water* 13. <https://doi.org/10.3390/w13040561>.
- Lovrinović, I., Srzić, V., Matić, I., Brkić, M., 2022. Combined multilevel monitoring and wavelet transform analysis approach for the inspection of ground and surface water dynamics in shallow coastal aquifer. *Water*. <https://doi.org/10.3390/w14040656>.
- Mastrocicco, M., Colombani, N., 2021. The issue of groundwater salinization in coastal areas of the Mediterranean region: a review. *Water* 13. <https://doi.org/10.3390/w13010090>.
- Merritt, M.L., 2004. Estimating hydraulic properties of the Floridan Aquifer System by analysis of earth-tide, ocean-tide, and barometric effects, Collier and Hendry Counties, Florida. *Water Resour. Investig. Rep.* <https://doi.org/10.3133/wri034267>.
- Miyakoshi, A., Taniguchi, M., Ide, K., Kagabu, M., Hosono, T., Shimada, J., 2020. Identification of changes in subsurface temperature and groundwater flow after the 2016 Kumamoto earthquake using long-term well temperature–depth profiles. *J. Hydrol.* 582, 124530. <https://doi.org/10.1016/j.jhydrol.2019.124530>.
- Morgan, L.K., Werner, A.D., 2015. A national inventory of seawater intrusion vulnerability for Australia. *J. Hydrol. Reg. Stud.* 4, 686–698. <https://doi.org/10.1016/j.ejrh.2015.10.005>.
- Najib, S., Fadili, A., Mehdi, K., Riss, J., Makan, A., 2017. Contribution of hydrochemical and geoelectrical approaches to investigate salinization process and seawater intrusion in the coastal aquifers of Chaouia, Morocco. *J. Contam. Hydrol.* 198, 24–36. <https://doi.org/10.1016/j.jconhyd.2017.01.003>.
- Oude Essink, G.H.P., van Baaren, E.S., de Louw, P.G.B., 2010. Effects of climate change on coastal groundwater systems: a modeling study in the Netherlands. *Water Resour. Res.* 46. <https://doi.org/10.1029/2009WR008719>.
- Paldor, A., Shalev, E., Katz, O., Aharonov, E., 2019. Dynamics of saltwater intrusion and submarine groundwater discharge in confined coastal aquifers: a case study in northern Israel. *Hydrogeol. J.* 27, 1611–1625. <https://doi.org/10.1007/s10040-019-01958-5>.
- Pérez-Gómez, B., Manzano, F., Alvarez-Fanjul, E., González, C., Cantavella, J.V., Schindelé, F., 2016. Lessons derived from two high-frequency sea level events in the Atlantic: implications for coastal risk analysis and Tsunami detection. *Front. Mar. Sci.* 3. <https://doi.org/10.3389/fmars.2016.00206>.
- Petitta, M., Primavera, P., Tuccimei, P., Aravena, R., 2011. Interaction between deep and shallow groundwater systems in areas affected by Quaternary tectonics (Central Italy): a geochemical and isotope approach. *Environ. Earth Sci.* 63, 11–30.
- Pilla, G., Torrese, P., 2022. Hydrochemical-geophysical study of saline paleo-water contamination in alluvial aquifers. *Hydrogeol. J.* 30, 511–532. <https://doi.org/10.1007/s10040-021-02446-5>.

- Post, V., Kooi, H., Simmons, C., 2007. Using hydraulic head measurements in variable-density ground water flow analyses. *Ground Water* 45, 664–671. <https://doi.org/10.1111/j.1745-6584.2007.00339.x>.
- Proakis, J. g, Manolakis, D.G., 2006. Digital signal processing, Fourth Ed. ed, Journal of Chemical Information and Modeling. Prentice-Hall, Inc. Division of Simon and Schuster One Lake Street Upper Saddle River, NJUnited States.
- Qin, R., Wu, Y., Xu, Z., Xie, D., Zhang, C., 2013. Assessing the impact of natural and anthropogenic activities on groundwater quality in coastal alluvial aquifers of the lower Liaohe River Plain, NE China. *Appl. Geochem.* 31, 142–158. <https://doi.org/10.1016/j.apgeochem.2013.01.001>.
- Racetin, I., Krtalic, A., Srzic, V., Zovko, M., 2020. Characterization of short-term salinity fluctuations in the Neretva River Delta situated in the southern Adriatic Croatia using Landsat-5 TM. *Ecol. Indic.* 110, 105924 <https://doi.org/10.1016/j.ecolind.2019.105924>.
- Rahi, K.A., Halihan, T., 2013. Identifying aquifer type in fractured rock aquifers using harmonic analysis. *GroundWater* 51, 76–82. <https://doi.org/10.1111/j.1745-6584.2012.00925.x>.
- Ratner-Narovlansky, Y., Weinstein, Y., Yechieli, Y., 2020. Tidal fluctuations in a multi-unit coastal aquifer. *J. Hydrol.* 580, 124222 <https://doi.org/10.1016/j.jhydrol.2019.124222>.
- Re, V., Zuppi, G.M., 2011. Influence of precipitation and deep saline groundwater on the hydrological systems of Mediterranean coastal plains: a general overview. *Hydrol. Sci. J.* 56, 966–980. <https://doi.org/10.1080/02626667.2011.597355>.
- Romić, D., Castrignanò, A., Romić, M., Buttafuoco, G., Bubalo Kovačić, M., Ondrašek, G., Zovko, M., 2020. Modelling spatial and temporal variability of water quality from different monitoring stations using mixed effects model theory. *Sci. Total Environ.* 704, 135875 <https://doi.org/10.1016/j.scitotenv.2019.135875>.
- Rosenthal, E., Zilberbrand, M., Livshitz, Y., 2007. The hydrochemical evolution of brackish groundwater in central and northern Sinai (Egypt) and in the western Negev (Israel). *J. Hydrol.* 337, 294–314. <https://doi.org/10.1016/j.jhydrol.2007.01.042>.
- Saidi, S., Bourl, S., Ben Dhia, H., Anselme, B., 2009. A GIS-based susceptibility indexing method for irrigation and drinking water management planning: Application to Chebba–Mellouleche Aquifer, Tunisia. *Agric. Water Manag.* 96, 1683–1690. <https://doi.org/10.1016/j.agwat.2009.07.005>.
- Santucci, L., Carol, E., Kruse, E., 2016. Identification of palaeo-seawater intrusion in groundwater using minor ions in a semi-confined aquifer of the Río de la Plata littoral (Argentina). *Sci. Total Environ.* 566–567, 1640–1648. <https://doi.org/10.1016/j.scitotenv.2016.06.066>.
- Shi, L., Jiao, J.J., 2014. Seawater intrusion and coastal aquifer management in China: a review. *Environ. Earth Sci.* 72, 2811–2819. <https://doi.org/10.1007/s12665-014-3186-9>.
- Shin, J., Hwang, S., 2020. A borehole-based approach for seawater intrusion in heterogeneous coastal aquifers, eastern part of Jeju Island, Korea. *Water* 12. <https://doi.org/10.3390/w12020609>.
- Sithara, S., Pramada, S.K., Thampi, S.G., 2020. Impact of projected climate change on seawater intrusion on a regional coastal aquifer. *J. Earth Syst. Sci.* 129. <https://doi.org/10.1007/s12040-020-01485-y>.
- Srzic, V., Lovrinović, I., Racetin, I., Pletikosić, F., 2020. Hydrogeological characterization of coastal aquifer on the basis of observed sea level and groundwater level fluctuations: Neretva Valley Aquifer, Croatia. *Water* 12, 348. <https://doi.org/10.3390/w12020348>.
- Stein, S., Yechieli, Y., Shalev, E., Kasher, R., Sivan, O., 2019. The effect of pumping saline groundwater for desalination on the fresh-saline water interface dynamics. *Water Res.* 156, 46–57. <https://doi.org/10.1016/j.watres.2019.03.003>.
- Teo, H.T., Jeng, D.S., Seymour, B.R., Barry, D.A., Li, L., 2003. A new analytical solution for water table fluctuations in coastal aquifers with sloping beaches. *Adv. Water Resour.* 26, 1239–1247. <https://doi.org/10.1016/j.advwatres.2003.08.004>.
- Turnadge, C., Crosbie, R.S., Barron, O., Rau, G.C., 2019. Comparing methods of barometric efficiency characterization for specific storage estimation. *Groundwater* 57, 844–859. <https://doi.org/10.1111/gwat.12923>.
- Vahidipour, M., Raeisi, E., van der Zee, S.E.A.T.M., 2021. Active saltwater intrusion of shrinking Bakhtegan -Thask Lakes in South Iran threatens the freshwater resources of coastal aquifers. *J. Hydrol. Reg. Stud.* 34, 100790 <https://doi.org/10.1016/j.ejrh.2021.100790>.
- Vallejos, A., Sola, F., Pulido-Bosch, A., 2014. Processes influencing groundwater level and the freshwater-saltwater interface in a coastal aquifer. *Water Resour. Manag.* 29, 679–697. <https://doi.org/10.1007/s11269-014-0621-3>.
- Vallejos, A., Sola, F., Yechieli, Y., Pulido-Bosch, A., 2018. Influence of the paleogeographic evolution on the groundwater salinity in a coastal aquifer. Cabo de Gata aquifer, SE Spain. *J. Hydrol.* 557, 55–66. <https://doi.org/10.1016/j.jhydrol.2017.12.027>.
- van Engelen, J., Oude Essink, G.H.P., Kooi, H., Bierkens, M.F.P., 2018. On the origins of hypersaline groundwater in the Nile Delta aquifer. *J. Hydrol.* 560, 301–317. <https://doi.org/10.1016/j.jhydrol.2018.03.029>.
- van Engelen, J., Verkaik, J., King, J., Nofal, E.R., Bierkens, M.F.P., Oude Essink, G.H.P., Engelen, Joeri Van, Verkaik, J., King, J., Nofal, E.R., Bierkens, M.F.P., 2019. A three-dimensional palaeohydrogeological reconstruction of the groundwater salinity distribution in the Nile Delta Aquifer. *Hydrol. Earth Syst. Sci.* 23, 5175–5198. <https://doi.org/10.5194/hess-23-5175-2019>.
- Welch, P.D., 1967. The use of fast Fourier transform for the estimation of power spectra: a method based on time averaging over short, modified periodograms. *IEEE Trans. Audio Electro* 15, 70–73.
- Werner, A.D., Bakker, M., Post, V.E.A., Vandenbohede, A., Lu, C., Ataie-Ashtiani, B., Simmons, C.T., Barry, D.A., 2013. Seawater intrusion processes, investigation and management: recent advances and future challenges. *Adv. Water Resour.* 51, 3–26. <https://doi.org/10.1016/j.advwatres.2012.03.004>.
- Wood, C., Harrington, G.A., 2015. Influence of seasonal variations in sea level on the salinity regime of a coastal groundwater-fed wetland. *Groundwater* 53, 90–98. <https://doi.org/10.1111/gwat.12168>.
- Xia, Y., Li, H., 2009. The estimation of aquifer parameters using tidal effect in a coastal aquifer: a case study in Beihai Peninsula. *Dixue Qianyan Earth Sci. Front* 16, 276–281. [https://doi.org/10.1016/S1872-5791\(08\)60121-9](https://doi.org/10.1016/S1872-5791(08)60121-9).
- Xu, Zhongyuan, Hu, B.X., Xu, Zexuan, Wu, X., 2019. Numerical study of groundwater flow cycling controlled by seawater/freshwater interaction in Woodville Karst Plain. *J. Hydrol.* 579, 124171 <https://doi.org/10.1016/j.jhydrol.2019.124171>.
- Yang, H., Shimada, J., Shibata, T., Okumura, A., Pinti, D.L., 2020. Freshwater lens oscillation induced by sea tides and variable rainfall at the uplifted atoll island of Minami-Daito, Japan. *Hydrogeol. J.* 28, 2105–2114. <https://doi.org/10.1007/s10040-020-02185-z>.
- Yechieli, Y., Sivan, O., 2011. The distribution of saline groundwater and its relation to the hydraulic conditions of aquifers and aquitards: examples from Israel. *Hydrogeol. J.* 19, 71–81. <https://doi.org/10.1007/s10040-010-0646-5>.
- Yeh, H.D., Huang, C.S., Chang, Y.C., Jeng, D.S., 2010. An analytical solution for tidal fluctuations in unconfined aquifers with a vertical beach. *Water Resour. Res.* 46. <https://doi.org/10.1029/2009WR008746>.
- Zhang, X., Dong, F., Dai, H., Hu, B.X., Qin, G., Li, D., Lv, X., Dai, Z., Soltanian, M.R., 2020. Influence of lunar semidiurnal tides on groundwater dynamics in estuarine aquifers. *Hydrogeol. J.* 28, 1419–1429. <https://doi.org/10.1007/s10040-020-02136-8>.
- Zovko, M., Romić, D., Colombo, C., Di Iorio, E., Romić, M., Buttafuoco, G., Castrignanò, A., 2018. A geostatistical Vis-NIR spectroscopy index to assess the incipient soil salinization in the Neretva River valley. *Croat. Geoderma* 332, 60–72. <https://doi.org/10.1016/j.geoderma.2018.07.005>.

- Alessandrino L., Gaiolini M., Cellone F. A., Colombani N., Mastrocicco M., Cosma M., Da Lio C., Donnici S., & Tosi L. (2023). Salinity origin in the coastal aquifer of the Southern Venice lowland, *Science of The Total Environment*, 167058, doi:10.1016/j.scitotenv.2023.167058, 2023.

Journal Pre-proof

Salinity origin in the coastal aquifer of the Southern Venice lowland

Luigi Alessandrino, Mattia Gaiolini, Francisco Aldo Cellone, Nicolò Colombani, Micòl Mastrocicco, Marta Cosma, Cristina Da Lio, Sandra Donnici, Luigi Tosi



PII: S0048-9697(23)05685-1

DOI: <https://doi.org/10.1016/j.scitotenv.2023.167058>

Reference: STOTEN 167058

To appear in: *Science of the Total Environment*

Received date: 11 June 2023

Revised date: 10 September 2023

Accepted date: 11 September 2023

Please cite this article as: L. Alessandrino, M. Gaiolini, F.A. Cellone, et al., Salinity origin in the coastal aquifer of the Southern Venice lowland, *Science of the Total Environment* (2023), <https://doi.org/10.1016/j.scitotenv.2023.167058>

This is a PDF file of an article that has undergone enhancements after acceptance, such as the addition of a cover page and metadata, and formatting for readability, but it is not yet the definitive version of record. This version will undergo additional copyediting, typesetting and review before it is published in its final form, but we are providing this version to give early visibility of the article. Please note that, during the production process, errors may be discovered which could affect the content, and all legal disclaimers that apply to the journal pertain.

© 2023 Published by Elsevier B.V.

Salinity origin in the coastal aquifer of the Southern Venice lowland

Luigi Alessandrino¹, Mattia Gaiolini², Francisco Aldo Cellone^{3,4}, Nicolò Colombani^{2*}, Micòl Mastrocicco¹, Marta Cosma³, Cristina Da Lio³, Sandra Donnici³, Luigi Tosi³

¹ DiSTABiF - Department of Environmental, Biological and Pharmaceutical Sciences and Technologies, Campania University “Luigi Vanvitelli”, Via Vivaldi 43, 81100 Caserta, Italy.

² SIMAU - Department of Materials, Environmental Sciences and Urban Planning, Marche Polytechnic University, Via Breccie Bianche 12, 60131 Ancona, Italy.

³ IGG - Institute of Geosciences and Earth Resources, National Research Council, Via G. Gradenigo 6, 35131 Padova, Italy.

⁴ Centro de Investigaciones del Medio Ambiente Consejo Nacional de Investigaciones Científicas y Técnicas, Universidad Nacional de La Plata (CIM-UNLP-CONICET), Buenos Aires, Argentina.

* Correspondence: n.colombani@univpm.it

Abstract

Groundwater salinization can be natural and anthropogenic in origin, although it often results from a combination of both, especially in low-lying coastal regions that are hydraulically controlled. This study proposes a method to assess the origin of salinity using environmental tracers in porewater, like Cl^- and Br^- , combined with depositional facies associations detected in sediment cores. Such integrated approach was tested in a target area south of the Venice Lagoon (Italy), where groundwater salinization is triggered by multiple mechanisms due to the complexity of the hydro-geomorphological environment. Batch tests were performed on sediment core samples from boreholes to quantify major anions and total inorganic N. Cl^- and Br^- porewater concentrations coupled with sedimentary facies association provided insights into the

origin of groundwater salinity from a variety of sources, including past and present seawater intrusion, agricultural leaching, and evaporites. The strengths and limitations of the integrated approach are discussed to provide a pathway for improving water resource management and planning measures to prevent groundwater salinization in coastal areas.

Keywords: Cl^-/Br^- molar ratio; sediment porewater; aquifer salinization; depositional environments.

1. Introduction

One of the most widespread and alarming phenomena affecting coastal areas is the progressive salinization of freshwater resources (Li et al., 2020). Groundwater salinization occurs at local and regional scales and may have diverse origins (Maniannan and Elango, 2019; Wen et al., 2005). In many cases, it is plausible to assume that seawater intrusion is involved, especially in lowland coastal areas because of small head gradients combined with drainage management. In addition, groundwater depletion where human activities are concentrated (Ashraf et al., 2017; Wu et al., 2013) and climate change, such as sea level rise (Da Lio and Tosi, 2019) and extended periods of below-average rainfall (Mastrocicco and Colombani, 2021), are exacerbating groundwater salinization. However, other natural salt sources or human activities may cause groundwater salinization (Cartwright et al., 2004). Evaporation, evaporite leaching, mobilization of salts stored in the unsaturated zone, infiltration of sewage polluted surface waters, slow-moving saline/salt waters of marine origin, highly mineralized waters from geothermal fields, sea spray, hyper-filtration from aquitards, and agricultural practices are the most significant salt sources/processes globally recognized (Barbecot et al., 2000; Li et al., 2020). Paleo-seawater is also common in coastal plains, both in confined aquifers (Barbecot et al., 2000; Montety et al., 2008) and, at least at patches, in shallow Holocene aquifers (Caschetto et al., 2016; Giambastiani

et al., 2021; Kuang et al., 2015; Tran et al., 2012).

For cost-effective management of water resources, it is important to understand the mechanisms that control the exchange of fresh and salt waters, including the vertical variability of groundwater salinity, to calculate the amount and the direction of saline groundwater seepage in lowland coastal areas (de Louw et al., 2010). To monitor the variability of the saltwater-freshwater interface in unconfined aquifers, the profiling of electrical conductivity (EC) recorded using data loggers in fully screened wells is a widespread practice. Nevertheless, this technique has some drawbacks due to intraborehole mixing processes that could alter the saltwater-freshwater interface and redox gradients (Mastrocicco et al., 2012; Shalev et al., 2009). As recently shown by Cavallina et al. (2022), the morpho-stratigraphic variability of the Venice coastal plain can be a key factor in the distribution of groundwater salinity. Here, small lithological variabilities were found to constrain the groundwater dynamics, affecting the freshwater-saltwater exchange. The same results were found in the southern portion of the Po Delta (Italy), where back barrier depositional facies were linked to a significant increase of groundwater salinity at shallow depths (Colombani et al., 2017; Di Giuseppe et al., 2014). In absence of dedicated multi-level samplers, to prove the concept expressed by Cavallina et al. (2022), a viable technique is the porewater extraction from sediment cores via batch experiments (Jiao et al., 2010). Batch experiments can be used to investigate the origin of groundwater salinity, especially analyzing non-reactive species such as chloride (Cl^-) and bromide (Br^-) that are not involved in redox reactions and thus could be considered environmental tracers (Cook and Herczeg, 2012).

The aim of this study is to highlight the strengths and weaknesses of porewater extraction as a method to assess the origin of salinity in coastal aquifers. This is a pivotal step since a correct

understanding of the different sources of salinity may lead to a well-balanced water resources management in coastal aquifers, while often only actual seawater salinity is considered in management strategies (Hussain et al., 2019). The southern coastal area of the Venice Lagoon (Italy) was selected to test the proposed approach. For this purpose, sediment samples were collected at different depths and locations in the study area and the results from solute release in batch experiments were validated through sedimentary facies associations and hydrogeological information to unravel the salinity origin and the morpho-stratigraphic control on groundwater circulation.

2. Study Area

The study area is located in the northern Adriatic coastal plain at the southern edge of the Venice Lagoon (Italy), in a low-lying agricultural region immediately south of the lower Brenta and Bacchiglione rivers (Fig. 1). The physiographic features of this region are the result of a combination of natural processes and human interventions, including land subsidence (Tosi et al., 2016), river diversions (Ferrinello et al., 2021; Bondesan and Furlanetto, 2012), and hydraulic land reclamation carried out in the first three decades of the last century (Frascaroli et al., 2021). Due to the severe land subsidence associated with the oxidation of peat deposits (Gambolati et al., 2005), land elevations are now between -4 and -1 m above sea level (a.s.l.). Only the riverbanks of watercourses connected to the sea are a few meters a.s.l.. The elevation differences in the area, originally due to the morphology of ancient marshes, lagoons, channel systems, coastal ridges, and coastal dunes before hydraulic land reclamation (Rizzetto et al., 2003), have been exacerbated in the last century by different land subsidence (Tosi et al., 2016). This critical Polder-like morphology represents a major hydrogeological hazard, especially for

flooding and groundwater salinization (Da Lio et al., 2015; Tosi et al., 2022), with serious environmental and economic consequences (Torresan et al., 2012).

The water table is kept below sea level by a network of reclamation canals connected to pumping stations that drain the excess water into the lagoon, rivers, and sea. The water table fluctuates seasonally between 0.4 and 0.8 m below ground surface (i.e., between -2.4 and -2.8 m a.s.l.), depending on agricultural activities. The aquifer shows background values of EC ranging from 45 to 25 mS/cm, which decrease with increasing distance from the lagoon southward (Lovrinović et al., 2021). Precipitation significantly mitigates the high background levels of saline water in shallow unconfined aquifers, especially in the upper part of the aquifer associated with the paleochannel and coastal paleoridge systems. The influence of daily tidal variations on groundwater salinity is negligible, as is the influence on the water table since this is regulated by pumping stations. Contra wise, the influence of the Brenta, Bacchiglione, and Canal Morto rivers is evident during prolonged drought and high rainfall periods, with seawater ingression during droughts and freshwater flushing in wet periods.

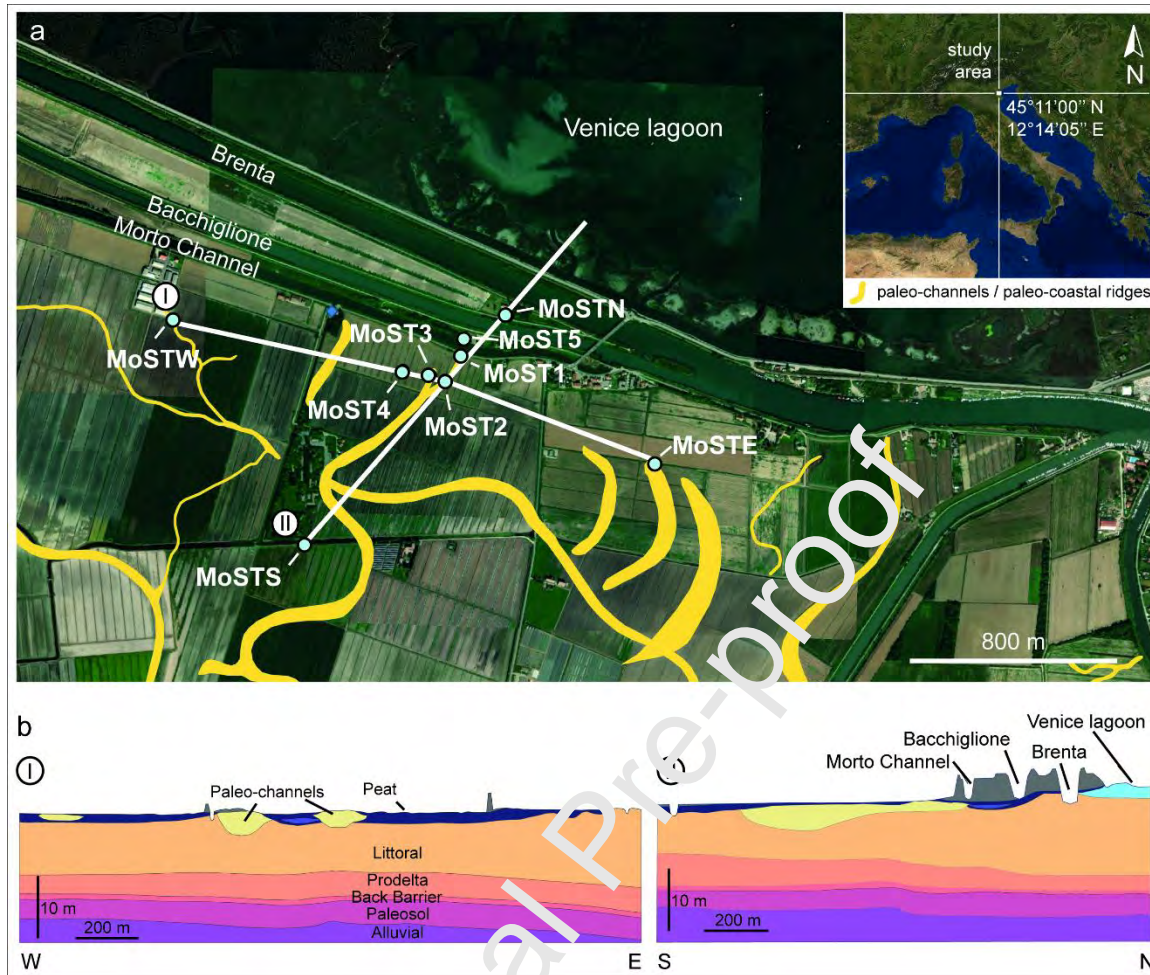


Figure 1. (a) Satellite image of the study area showing the locations of MoST wells and sediment cores. The main sandy geomorphological structures are highlighted in yellow. (b) Geological cross-sections showing depositional units.

The hydro-stratigraphic architecture in the study area is made up of sedimentary deposits of Late Pleistocene and Holocene age. The relationship between the subsurface architecture and the near-surface portion of the aquifer system is shown in Figure 1. The Pleistocene sedimentary sequence is associated with the sea-level lowstand and consists of alluvial sands, silts, and clays deposited during the Last Glacial Maximum (LGM) (Donnici et al., 2012) when sea level was roughly 110-120 m lower than today (Storms et al., 2008). The uppermost Pleistocene aquifer

consists of fluvial sands bounded above by a regionally extensive aquiclude of overconsolidated clayey deposits, a paleosol called *Caranto* (Donnici et al., 2011). The Holocene depositional units comprise a thin sedimentary sequence related to marine transgression, consisting of back barrier deposits, which is overlaid by the marine highstand sedimentary sequence. This sequence is related to the progradation of fluvio-deltaic systems, and consists of prodelta, delta front /littoral and delta plain/lagoon deposits (Zecchin et al., 2009; Tosi et al., 2009). The most important phreatic aquifer is associated to the littoral deposits, which extend on a regional scale. Other aquifers of local extent are associated to paleochannel systems and ancient littoral ridges.

3. Materials and methods

Nine sediment cores (MoST1, MoST2, MoST3, MoST4, MoST5, MoSTN, MoSTS, MoSTE, MoSTW) were provided by the EU projects MoST and SeCure. The locations of the cores were chosen to capture the variability of the subsurface on a local scale, including the paleochannels and interbasins shown in figure 1. The selection of samples for each core was done in the field, collecting a sample at each macroscopic change in grain size, color, or presence of fragments (shells and/or vegetation).

Analysis of sedimentary cores in terms of lithology, grain size, sedimentary structures, color, and sorting as well as the presence of fossils, vegetal remains, and bioturbation, allowed the identification of facies associations (FA), each revealing different paleoenvironments (Cavallina et al., 2022). For the purposes of this paper, the facies associations described by Cavallina et al. (2022) have been grouped into the units U1, U2, U3 and U4 (Table 1). This simplification allowed a statistical representativeness of the data per unit, while maintaining the overall significance of the depositional environments where sediments were settled.

Table 1. Correspondences between the facies associations of Cavallina et al. (2022) and the unit associations used in the present work, with the number of samples collected.

| Facies association from Cavallina et al., 2022 | Description | Units in the present work and number of samples |
|---|--|--|
| Fa7 | Peat and peaty clay layers of wetland areas. Back-barrier deposits | U1 (25) |
| Fa6 | Medium to fine sand, laminated, containing shell fragments and plant remains, with a lenticular geometry base. Lagoonal (tidal) channel deposits | |
| Fa5 | Well sorted, fine to medium sand, with abundant shells. Littoral deposits | U2 (37) |
| Fa4 | Alternation of clayey and sandy silt with thin layers of fine laminated sand, with sparse mollusk shells. Prodelta deposits | U3 (32) |
| Fa3 | Silt to silty sand deposits with coarse-grained sediments and shell fragments above the erosive base. Transgressive back barrier deposits | |
| Fa2 | Clay to silty clay layers showing evident signs of pedogenesis. Alluvial pedogenized deposits referable to the <i>Coranto</i> paleosol | U4 (9) |
| Fa1 | Medium beds of micaceous silty sand alternate with silt with vegetal remains and roots. Alluvial deposits | |

Sediment samples for the batch experiments were selected along cores to represent the stratigraphic distribution of the subsurface. They were stored in sediment boxes and subsampled in the field at each relevant macroscopic change in grain size, and then transported in the laboratory for analyses.

Batch leaching experiments were performed using the saturation soil extraction (SSE) method described by Schuwirth and Hofmann (2006) using deionized water (EC $10 \pm 2 \mu\text{S}/\text{cm}$, pH 6.5 ± 0.01 , ORP $150 \pm 10 \text{ mV}$) as liquid phase, while samples from sediment cores were used as solid phase. Batches were performed with a liquid/solid (L/S) ratio of 5:1 and the contact time was set at 80 days to allow the solid matrix to reach equilibrium with the liquid phase. Each

batch was carried out in a Kartell container with a rectangular bottom (3.9 cm x 4.5 cm) and a height of 8.5 cm, which had a double stopper to seal off its content from the outside. To prevent algal growth, batches were kept in the dark, and in a temperature-controlled environment ($25^{\circ}\text{C}\pm 1^{\circ}\text{C}$) and not stirred to mimic aquifer conditions.

TDS and pH (Supplementary dataset) were monitored each week using a HANNA multiparametric probe (HI98194) to check when equilibrium among solid and liquid phases was reached. The probe was calibrated before each measurement set for EC, pH and ORP using HANNA solution standards and the conversion factor among EC and TDS was 0.66 (APHA, 2017). While TDS or salinity are affected by reactions like mineral dissolution or organic matter oxidation, Cl^- and Br^- ions can be used as tracers to determine: i) the source of salinity in groundwater (Lorenzen et al., 2012; Park et al., 2015), ii) the genesis of deep saline waters, and iii) the degree of deep brines development (Slober and Bucher, 1999). Cl^- and Br^- are typically non-reactive ions because neither redox reactions nor low solubility minerals affect their contents. Consequently, the Cl^-/Br^- ratio must remain constant when Cl^- and Br^- originate from the same source (Alcalà and Custodio, 2008). This may help to distinguish between anthropogenic and natural causes of salinization (Hudak, 2003). After 80 days, water samples were collected from the batches and filtered to be analyzed for F^- , Cl^- , Br^- , NO_3^- , NO_2^- , SO_4^{2-} , and PO_4^{3-} with an ICS-1000 Dionex-ThermoFisher ion chromatography system equipped with an isocratic dual pump, an IonPac AS14A 4x250 mm column, an AG14A 4x50mm pre-column, and an ASRS-Ultra 4-mm self-suppressor for anions. NH_4^+ was quantified via Pharmacia 300 UV/VIS spectrophotometer with a Nessler reagent (Hach-Lange, UK). Mineral N was calculated summing the concentrations of NO_3^- , NO_2^- , and NH_4^+ . Quality control (QC) samples were run every ten samples. The standard deviation for all QC samples run was better than 4%, whereas

the accuracy which was 5% for anions and 3% for NH_4^+ , reported as the average of the relative differences between the measured and known standards.

Porewater concentrations C_{pw} were calculated using the following formula:

$$C_{pw} = d * C \left(\frac{\rho_b}{n} \right) \quad (1)$$

where d is the dilution factor due to the batch L/S; C is the concentration of the analyzed species in the liquid phase, ρ_b is the dry bulk density of the sample, and n is the total porosity of the sample. To assess the HI98194 probe stability, every ten measurements in batches the probe was immersed in a calibration solution for QC. The accuracy of the batch measurements was $\pm 1\%$ of reading for TDS, ± 0.02 for pH and ± 1.0 mV for ORP. The accuracy of d , ρ_b and n parameters was approximately $\pm 1\%$ each, thus the overall uncertainty never exceeded $\pm 5\%$ of the reported values for TDS, pH and ORP and never exceeded $\pm 3\%$ for the C_{pw} . The end-members of non-reactive freshwater-saltwater mixing were the chemical composition of the Po River, Adige River, Venice Lagoon, and Adriatic seawater sourced from Colombani et al. (2017) and Gattacceca et al. (2009), which were used to infer different salinization mechanisms. The Cl^-/Br^- evaporation line was derived via linear interpolation over rain samples and U3 samples.

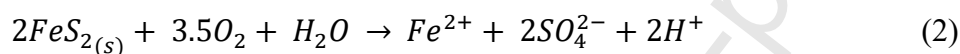
4. Results and discussion

4.1 Monitoring of TDS and pH

Equilibrium between the solid and liquid phases was achieved after 40 days, as testified by the negligible variations in TDS C_{pw} and pH values (Fig. 2). The TDS C_{pw} and pH values during the monitoring period are shown in Figure 2a for the samples with the highest SO_4^{2-} and in Figure 2b for the samples with peat content. Despite here only few samples are shown, all the others behaved in a very similar way, with a sharp TDS increase at the beginning followed by a plateau.

All the data are reported in the supplementary dataset.

In Figure 2a, the samples show a similar decreasing pH trend and a corresponding increase of TDS due to the SO_4^{2-} released by mineral phases, like pyrite or gypsum. Pyrite is the main candidate for SO_4^{2-} release since it is largely present in the *Caranto* paleosol (Donnici et al., 2011) and ubiquitous in subsurface organic sediments of the Po plain (Amorosi et al., 2002; Di Giuseppe et al., 2014), while gypsum is seldom found in such depositional environments (Amorosi et al., 2002). In fact, pyrite oxidation was enhanced by the following reaction under basic conditions (Bonnissel-Gissinger et al., 1998), since pH values of the batches were generally between 7.5 and 8.5 during the monitoring period:



From day 40 to 60, pH showed a slight increase due to the buffering effect of the *Caranto* paleosol (Donnici et al., 2011).

The peat samples have extremely low pH values (Fig. 2b), which can be attributed to the release of volatile and organic acids (Shetye, 1988). Accordingly, the release occurred during the first days of monitoring after which TDS reached equilibrium values. The high release of SO_4^{2-} in these samples was due to the batch oxidative environment. In fact, besides triggering pyrite oxidation, the biodegradation of phenolic compounds present in the peaty horizons may have been accelerated by the presence of oxygen (Freeman et al., 2004). Through this process, SO_4^{2-} esters present in the peat matrix and bound to humic molecules can be converted into SO_4^{2-} (Chapman and Davidson, 2001).

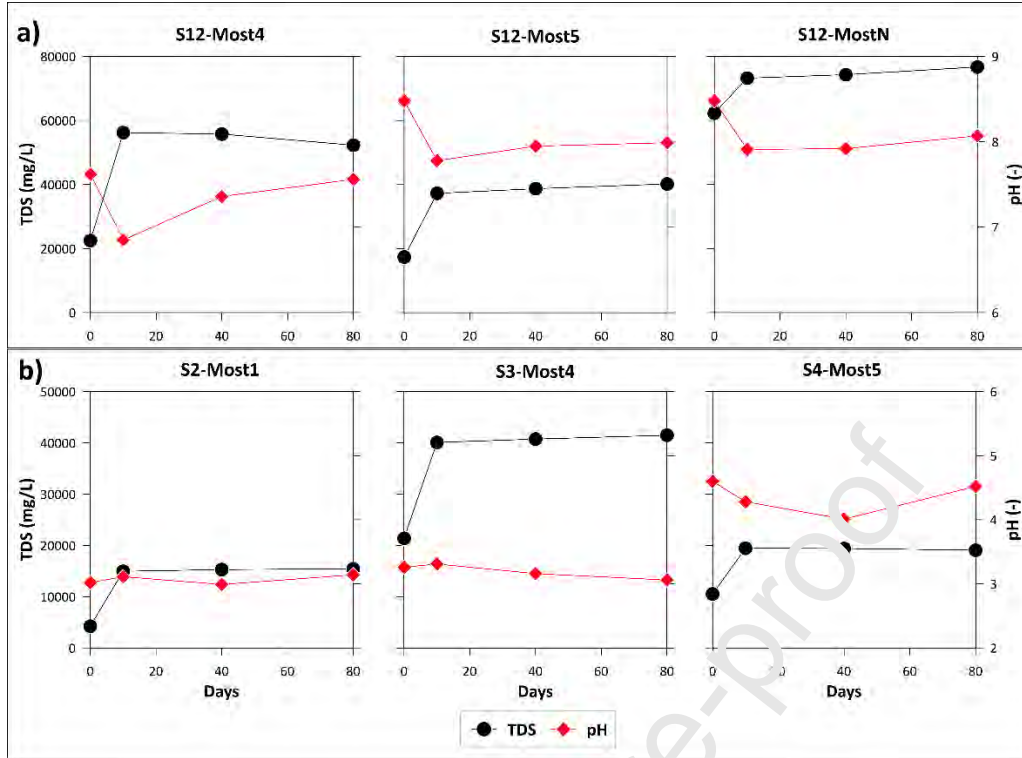


Figure 2. TDS (mg/L) and pH trends of selected samples during the monitoring period: a) Samples with the highest SO_4^{2-} collected from -14 to -21 m a.s.l. and b) Peat samples collected from -2.5 to -5.0 m a.s.l..

4.2 Salinity origins

TDS values much higher than the actual mean Adriatic seawater salinity (i.e., 35,190 mg/L as reported by Grilli et al., 2020) have been measured for many samples even at shallow depths of about -4.0 m a.s.l. While $\text{Cl}^- C_{pw}$ are generally lower than those of the actual mean Adriatic seawater (19,800 mg/L as reported by Colombani et al., 2017), and consistent with the mean Cl^- concentration of Mediterranean Sea (Khaska et al., 2013).

According to the relationship between TDS and Cl^- (Fig. 3a), the samples are not aligned along the sea-lagoon-freshwater mixing line, but they are all shifted above it, except for few cases. This means that TDS is not always related to chlorinity. The relationship between TDS and SO_4^{2-}

(Fig. 3b) is a further confirmation of this finding, as the samples are almost entirely distributed below the freshwater-seawater mixing line. Here, the far higher than expected SO_4^{2-} C_{pw} are due to the pyrite and organic matter oxidation that occurred in the oxidative environment of the batch experiments. Thus, the major limitation of simply using TDS values derived from the porewater to distinguish among actual and paleoseawater or evapoconcentrated waters is the possible oxidation of organic materials that could bias the results in batch experiments.

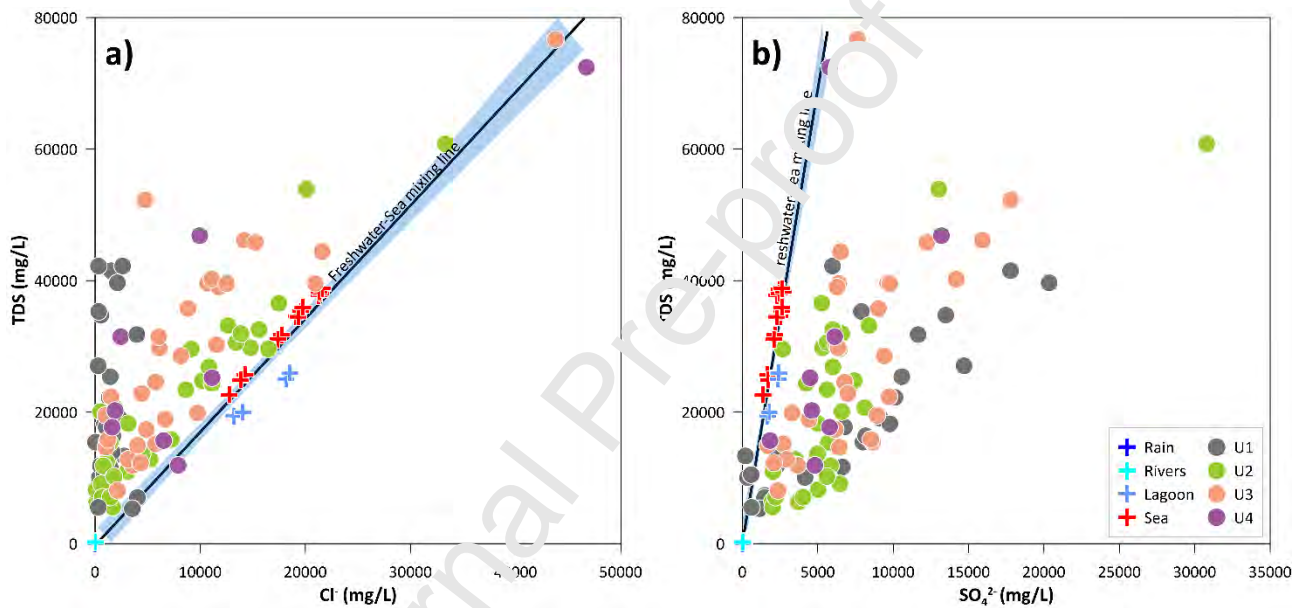


Figure 3. Batches' water samples. a) TDS (mg/L) vs Cl^- (mg/l); b) TDS (mg/L) vs SO_4^{2-} (mg/l). The black dotted lines indicate the Sea-Lagoon-Freshwater mixing lines, and the blue areas indicate a 95% confidence interval.

The most superficial samples, related to delta plain/lagoon deposits, have higher Br^- and lower Cl^- values than the actual Adriatic Sea-Freshwater mixing line (U1 in Fig. 4a); therefore, the origin of Br^- is not marine but agriculturally derived (Samantara et al., 2015). In addition, most of the deep samples fall within the evaporation line rather than falling along the actual Adriatic Sea-Freshwater mixing line. This suggests that actual seawater intrusion is not the major driver of

groundwater salinization, while other processes play a non-negligible role.

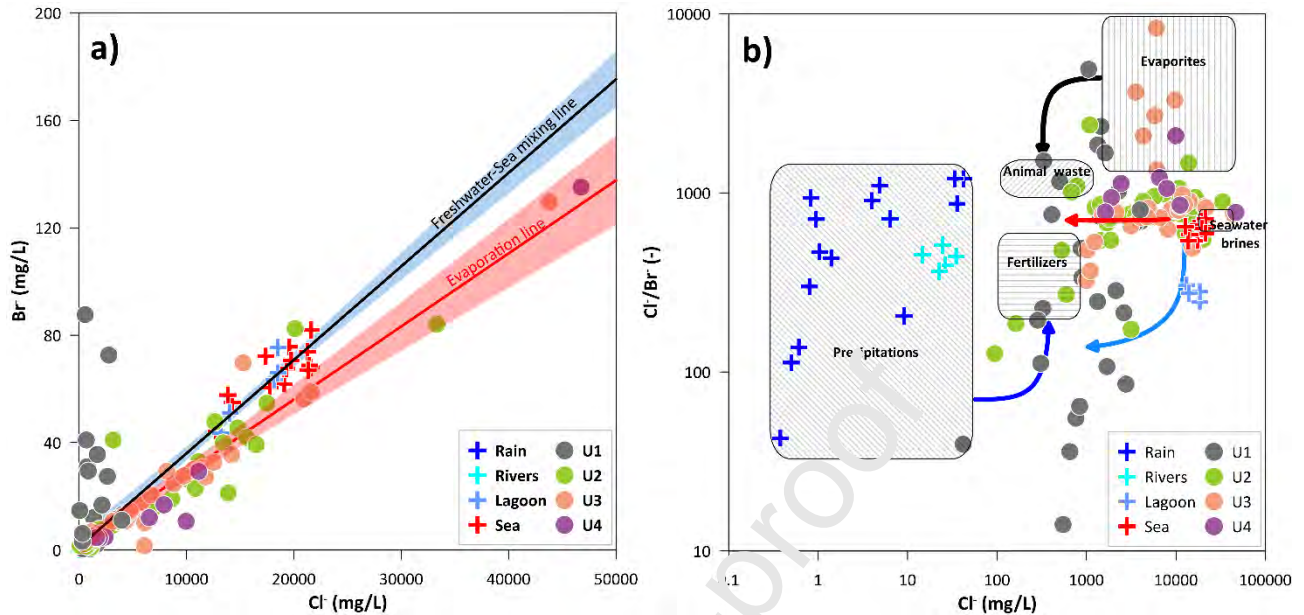


Figure 4. Batches' water samples: a) Br⁻ (mg/L) vs Cl⁻ (mg/l). The black line indicates the Sea-Lagoon-Rivers-Rain mixing line and the blue area indicates a 95% confidence interval. The red line indicates the evaporation line, and the pink area indicates a 95% confidence interval. b) Cl⁻/Br⁻ molar ratio (-) vs Cl⁻ (mg/l). The arrows indicate the different mixing lines among endmembers. Rectangular boxes are reported merging Alcalà and Custodio (2008), Panno et al. (2005), and Sun et al. (2019).

To identify the different endmembers and to disentangle the various mixing processes, the classical plots of Cl⁻/Br⁻ vs Cl⁻, and Br⁻ vs Br⁻ × 10³/Cl⁻ have been used. The Cl⁻/Br⁻ molar ratio of the Adriatic seawater samples (red crosses in Fig. 4b) is relatively scattered compared to the oceanic mean seawater of 655, due to the Po River's seasonal freshwater discharge that smooths the salinity of the Adriatic Sea close to the Po River delta (Artefiani et al., 1997). Only a few samples in this study had Cl⁻/Br⁻ ratio values attributable to the seawater or lagoon water intrusion and their mixing with freshwater endmembers (highlighted by the red arrow in Fig. 4).

The deeper samples associated with LGM deposits (U4) and prodelta Holocene deposits (U3) are aligned at Cl^-/Br^- 900 ± 80 (Fig. 4b), as previously noted by Colombani et al. (2017), which has been related to the intrusion of paleo-seawater and mixing with evaporitic layers. Those with an extremely low Cl^-/Br^- ratio are instead linked to recharge of agricultural leaching, as attested by their shallow depth and the association to the youngest unit of the delta plain/lagoon deposits, while a few shallow samples encompassed high evaporation and are mixed with manure (U1 in Fig. 4b). These results are consistent with the management of this land that has been intensively cultivated since the late 1970s (Cavallina et al., 2022). Samples with extremely high Cl^-/Br^- ratio found in U4 were linked to halite dissolution, very poor in Br^- (Herrmann, 1972), formerly precipitated in lagoonal and marsh environments characterized by shallow ponds in a drier than actual climate, plausibly during the post LGM marine transgression. Mixing processes have then diluted the original hypersaline waters with recharge waters. In fact, most samples are located between the evaporites leaching box and the Adriatic seawater samples (Fig. 4b).

Further validation that most of the salinity do not originate from actual seawater intrusion and not even from recently evaporated waters from the Venice lagoon but is rather due to paleosalinity (for the deepest samples) and mixing of different sources (for the shallow samples) is provided in Figure 5a. In the Br^- vs $\text{Br}^- \times 10^3 / \text{Cl}^-$ plot, the samples are not aligned along the halite-seawater line experiment carried out by Sun et al. (2019), which depicts the actual seawater evaporation trend. Instead, they exhibited evapoconcentration trends like those found for seawater evaporation, but starting from continental water (Zhang et al., 2018). Since continental waters have much lower Br^- content respect to seawater and higher $\text{Br}^- \times 10^3 / \text{Cl}^-$, they are aligned in a shifted line respect to the actual seawater evaporation line. From Figure 5b, it is evident that the $\text{Br}^- \times 10^3 / \text{Cl}^-$ molar ratio increased in the shallower facies U1 compared to the

deeper facies due to the anthropogenic input from agricultural activities, with a broad range of scattered values. In contrast, in the deeper depositional facies U4 the values are much less scattered, while facies U2 and U3 are also affected by mixing with actual seawater.

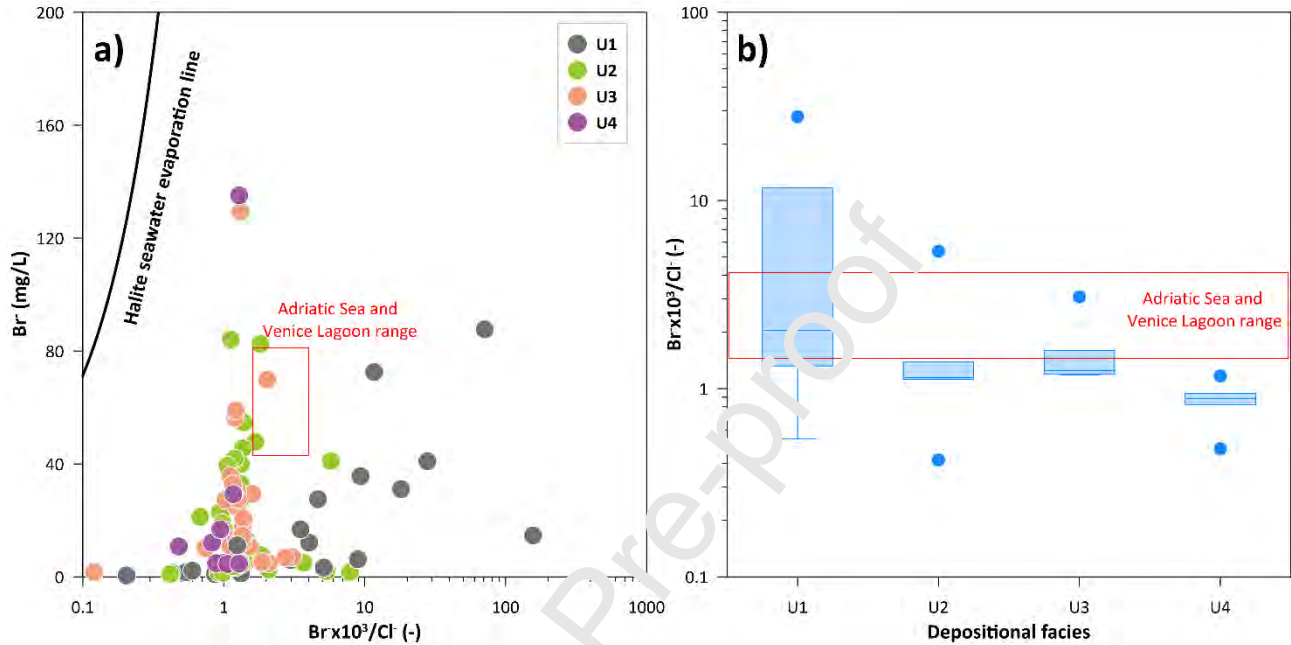


Figure 5. a) Plot of Br^- (mg/l) vs $\text{Br}^- \times 10^3 / \text{Cl}^-$ molar ratio (-) for the different depositional facies. The black line indicates the fitted line of a halite-seawater experiment reported by Sun et al. (2019) and the red rectangles indicate the ranges in actual sea and lagoon. b) Box-Whisker plot of $\text{Br}^- \times 10^3 / \text{Cl}^-$ molar ratio (-) for each depositional facies, with blue dots highlighting outliers.

4.3 Hydro-stratigraphic model paired with salt origin

The $\text{Cl}^- C_{pw}$ and $\text{Cl}^- / \text{Br}^-$ values have been analyzed in relation to subsurface depth and facies units (Fig. 6) to depict a simple conceptual model of freshwater-saltwater exchange coupled with groundwater salinity origins. This conceptual model is also discussed to highlight the strengths and limitations of sediment core batch analysis.

The shallowest facies associated with reworked deposits and the superficial facies of the

morpho-stratigraphic sequence characterized by peat and clays (lagoon/delta plain deposits of U1) show the lowest values of $\text{Cl}^- C_{pw}$ (Fig. 6), due to the infiltrating freshwater from canals and rainwater. The sandy deposits with medium-high permeability (littoral and delta front deposits of U2) are instead characterized by high variability, with increasing $\text{Cl}^- C_{pw}$ downward. Moving downward, the alternation of clayey and sandy silt with thin layers of fine laminated sand with low permeability (mostly prodelta deposits of U3) exhibited some peaks in $\text{Cl}^- C_{pw}$, considering the trends of the overlying layer. The silty and sandy deposits topped by overconsolidated clay deposits with extremely low permeability (the alluvial LGM deposits of U4), again showed a decrease in $\text{Cl}^- C_{pw}$ compared to U3.

The Cl^-/Br^- values show a more homogeneous trend along the core profiles with respect to Cl^- , with values around 900 as previously described, except for the samples from the evaporitic layers, which show remarkably high values. The recently recharged waters of agricultural origin are located in the upper part of the aquifer and do not exceed -8 m a.s.l. Below the shallow (recent) groundwater lies a thin wedge of actual seawater intruded in the most permeable layers at elevation among -8 and -12 m a.s.l. Below this thin layer a mixing between actual and paleo-seawater is present, while at the base of this lens can be found the endmember of evaporitic origin comprised among -20 and -22 m a.s.l., recognized only in 3 of the 9 cores analyzed. The latter has contributed to salinizing the whole aquitard (U3) via diffusion processes, given that the permeability of these sediments is low due to its silty matrix. When in doubt if mixing waters were from agricultural sources or from peaty layers the mineral N was checked, and if above 500 mg/L it was ascribed to peat release (see Supplementary database for the mineral N data), while PO_4^{3-} was of little use to delineate possible agricultural sources since it was always below detection limits in all the samples due to its low solubility in oxidizing environments (Di

Giuseppe et al., 2014). Also the $F^- C_{pw}$ supported the evapoconcentration of seawater with abrupt increases especially in U3 within low permeability layers characterized by higher than actual seawater Cl^-/Br^- values (see Supplementary database for the $F^- C_{pw}$), but given the high reactivity of F^- the relationship was complex with peaks also in peaty horizons where F^- may accumulate via adsorption or precipitation processes. Moreover, the confined aquifer has a hydraulic head higher than the Adriatic Sea and is therefore artesian in this area (Teatini et al., 2009). Thus, it can support slow diffuse upward gradients that may have led to mixing between the evaporitic porewaters and the less saline recharge waters from rivers and rainfall. This behavior is quite common in layered sedimentary coastal aquifers and aquitards characterized by polder-like environments (Casetto et al., 2016; de Louw et al., 2010; Kuang et al., 2015). The same aspect was also stressed in study on the southern Venice coastal aquifers (Gattacceca et al., 2009), where the authors noted the importance of upward groundwater fluxes favored by the network of reclamation channels, which in turn depressed the phreatic water table.

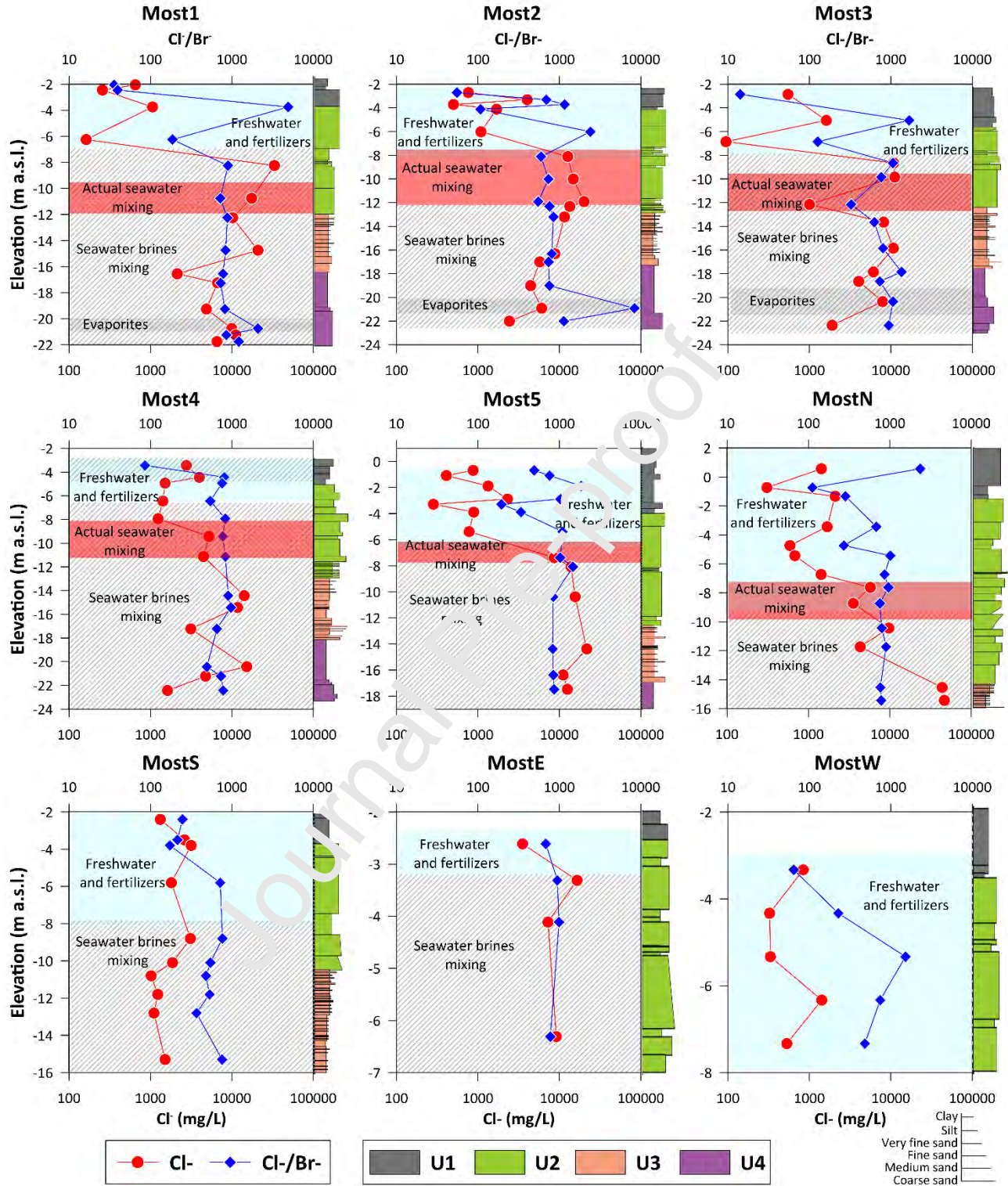


Figure 6. $\text{Cl}^- C_{pw}$ and Cl^-/Br^- values measured in the sedimentary cores and their salinity origins.

The depositional units (U) and sediments' grain size are shown. Note that the scale of vertical

and horizontal axes varies.

Figure 7 shows the overall conceptual model representing the exchange between the watercourses and the groundwater, together with the salinization mechanisms in the context of the hydrostratigraphic environment units, i.e., the saltwater contamination from the deeper evaporitic layer, the circulation of fresh-brackish-salt water from the rivers and toward the reclamation channels, and the present-day saltwater intrusion from the Venice lagoon. From a hydrogeological point of view, the groundwater head gradient is gently sloping from the Venice lagoon and rivers towards the reclamation canals network (Fig. 7), continuously drained by the pumping stations that pump back the water into the river. This short-circuit allow brackish and saline waters of the Venice lagoon to seep into the highly permeable sandy layers of U2 unit. While the confined aquifer provides the vertical head gradient that allows the slow upward migration of brines through the aquitard lenses of U3 and U4 (Fig. 7).

Previous studies based on geophysical surveys (de Franco et al., 2009; Teatini et al., 2011; Tosi et al., 2018; Viezzoli et al., 2019), water monitoring (Carbognin and Tosi, 2003; Lovrinović et al., 2021), and numerical modeling (Teatini et al., 2009) in this area were pivotal in delineating saltwater-freshwater relationships in both unconfined and confined aquifers and the lateral extent and temporal variability of saline groundwater, but they were unable to recognize different sources of salinity. While a recent study (Zancanaro et al., 2020) performed in this site using vadose zone data, highlighted the different origins of porewaters with two main sources: i) the actual seawater intrusion from the Venice lagoon, and ii) the salinity derived from peaty sediments. The Cl^-/Br^- values found by Zancanaro et al. (2020) are in good agreement with the ones here found at deeper depths and in distinct locations, independently proving the results of

this study.

The large-scale characterization via stable isotopes and Cl^-/Br^- values of Gattacceca et al. (2009) recognized the relative importance of evaporated groundwater endmembers. However, they were roughly able to quantify the evaporated groundwater contribution due to the long screen boreholes employed, that often obliterate the true aquifer mixing processes. For this type of analysis, given the complex hydrostratigraphic setting and multiple sources of salinization, the employment of high vertical resolution multi-level samples is fundamental for a better understanding of the salinization processes taking place in the area. In absence of dedicated multi-level samplers monitoring wells, the proposed strategy of analyzing C_{pw} via batch experiments and compare them with the unit associations may allow to distinguish among paleo and actual seawater origins, while standard integrated depth sampling often led to biased or even misleading conceptual models of coastal aquifer salinization (Colombani et al., 2016). This could provide crucial information for the development of numerical transport models that could support local authorities in the proper management of the water resources (Huang and Chiu, 2018; Werner and Gallagher, 2006) also in view of the predicted decreased recharge in Mediterranean coastal areas (Pasico et al., 2021). Limitations of this method arise from the availability of continuous core logs and their sedimentological/stratigraphical interpretation and from the batches' oxidative environment that may alter the C_{pw} TDS. Although, this could be overcome by using environmental tracers like Cl^- and Br^- not affected by redox reactions, or alternatively preserving the redox state of sediments via N_2 flushing and anaerobic incubations (Jiao et al., 2010), but the latter technique is extremely expensive and need highly specialized equipment.

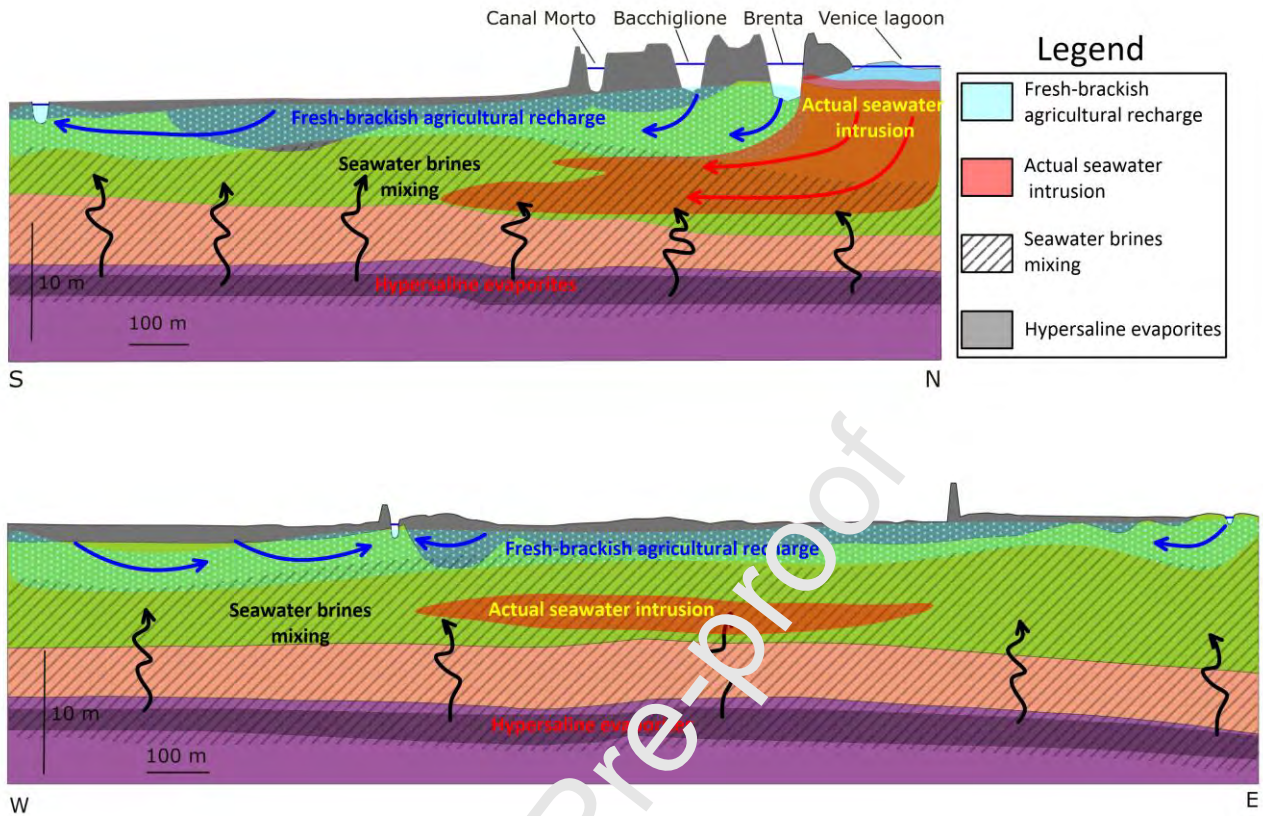


Figure 7. Schematic sketch of the salinization mechanisms and origin in the studied area, based on the porewater profiles.

5. Conclusions

This study shows that more than one hydrologic process contributes to groundwater salinization of the Venice lagoon coastal aquifer. Here, Br^- and Cl^- porewater concentrations coupled with the analysis of depositional unit associations helped to determine the different sources of salinity. The Br/Cl molar ratio and its reciprocal detected in the shallower samples showed that the causes of groundwater salinization in the shallow aquifer are most likely due to agricultural activities and not to the actual seawater intrusion, while the actual seawater wedge forms a thin layer of 2-3 m between the agricultural water (at the top) and the evaporated paleowater (at the bottom).

The main limitation of this approach concerns the biased TDS values derived from the porewater, which were affected by the oxidation of peat and pyrite in the batches. Therefore, only non-reactive environmental tracers shall be used to delineate salinity profiles of porewaters. In summary, the proposed approach has been designed to determine the origin of groundwater salinity in coastal areas to discriminate among actual seawater intrusion and other causes, such as trapped paleo-seawater or evapoconcentrated salts (halides) in transitional environments. The results of this study provide useful information to properly understand and manage groundwater salinization in coastal aquifers where actual seawater intrusion is often erroneously considered to be the main driver, leading to misguided land management policies that do not correctly address and effectively minimize the issue of salinization.

Acknowledgments

This research was supported by the EU co-financing the Interreg Italy–Croatia CBC Programme 2014–2020 (Cluster 2, Specific Objective 2.1) through the European Regional Development Fund as a part of the project “Saltwater intrusion and climate change: monitoring, countermeasures and informed governance” (SeCure AID: 10419304). The authors also acknowledge the project “Monitoring seawater intrusion in coastal aquifers and testing pilot projects for its mitigation” (MoST AID: 10047743). The authors would like to thank Mirco Marcellini for the IC analyses.

References

- Alcalá, F.J., Custodio, E., 2008. Using the Cl/Br ratio as a tracer to identify the origin of salinity in aquifers in Spain and Portugal. *J. Hydrol.* 359, 189–207.
<https://doi.org/10.1016/j.jhydrol.2008.06.028>
- Amorosi, A., Centineo, M. C., Dinelli, E., Lucchini, F., Tateo, F., 2002. Geochemical and

mineralogical variations as indicators of provenance changes in Late Quaternary deposits of SE Po Plain. *Sedim. Geol.* 151(3-4), 273–292. [https://doi.org/10.1016/S0037-0738\(01\)00261-5](https://doi.org/10.1016/S0037-0738(01)00261-5)

American Public Health Association (APHA), 2017. *Standard Methods for the Examination of Water and Wastewater*. 23rd edition. American Public Health Association, American Water Works Association, and Water Environment Federation, Washington DC (1268 pp. ISBN: 978-0-87553-287-5).

Artegiani, A., Bregant, D., Paschini, E., Pinardi, N., Raicich, F., Russo, A., 1997. The Adriatic sea general circulation. Part I: Air-sea interactions and water mass structure. *J. Phys. Oceanogr.* 27, 1492–1514. [https://doi.org/10.1175/1520-0485\(1997\)027<1492:TASGCP>2.0.CO;2](https://doi.org/10.1175/1520-0485(1997)027<1492:TASGCP>2.0.CO;2)

Ashraf, B., AghaKouchak, A., Alizadeh, A., 2017. Quantifying anthropogenic stress on groundwater resources. *Sci. Rep.* 7, 12910. <https://doi.org/10.1038/s41598-017-12877-4>

Barbecot, F., Marlin, C., Gibert, F., Dever, L., 2000. Hydrochemical and isotopic characterisation of the Bathonian and Bajocian coastal aquifer of the Caen area (northern France). *Appl. Geochem.* 15, 791–805. [https://doi.org/10.1016/S0883-2927\(99\)00088-8](https://doi.org/10.1016/S0883-2927(99)00088-8)

Bondesan, A., Furlanetto, P., 2012. Artificial fluvial diversions in the mainland of the lagoon of Venice during the 16th and 17th centuries inferred by historical cartography analysis *Géomorphologie* 2, 175–200. <https://doi.org/10.4000/geomorphologie.9815>

Bonnissel-Gissingner, P., Alnot, M., Ehrhardt, J.-J., Behra, P., 1998. Surface oxidation of pyrite as a function of pH. *Environ. Sci. Technol.* 32, 2839–2845. <https://doi.org/10.1021/es980213c>

Busico, G., Ntona, M. M., Carvalho, S. C., Patrikaki, O., Voudouris, K., Kazakis, N., 2021. Simulating future groundwater recharge in coastal and inland catchments. *Water Resour.*

- Manage. 35(11), 3617-3632. <https://doi.org/10.1007/s11269-021-02907-2>
- Carbognin, L., Tosi, L., 2003. Il Progetto ISES per l'Analisi dei processi di intrusione salina e subsidenza nei territori meridionali delle Province di Padova e Venezia. Istituto per lo Studio della Dinamica delle Grandi Masse, Venice, Italy.
- Cartwright, I., Weaver, T.R., Fulton, S., Nichol, C., Reid, M., Cheng, X., 2004. Hydrogeochemical and isotopic constraints on the origins of dryland salinity, Murray Basin, Victoria, Australia. *Appl. Geochem.* 19, 1233–1254. <https://doi.org/10.1016/j.apgeochem.2003.12.006>
- Caschetto, M., Colombani, N., Mastrocicco, M., Petitta, M., Aravena, R., 2016. Estimating groundwater residence time and recharge patterns in a saline coastal aquifer. *Hydrol. Process.* 30(22), 4202–4213. <https://doi.org/10.1002/hyp.10642>
- Cavallina, C., Bergamasco, A., Cosma, M., Galio, C., Donnici, S., Tang, C., Tosi, L., Zaggia, L., 2022. Morpho-Sedimentary constraints in the groundwater dynamics of low-lying coastal area: the southern margin of the Venice lagoon, Italy. *Water* 14(17), 2717. <https://doi.org/10.3390/w14172717>
- Chapman, S.J., Davidson, M.C., 2001. ^{35}S -sulphate reduction and transformation in peat. *Soil Biol. Biochem.* 33, 592–602. [https://doi.org/10.1016/S0038-0717\(00\)00201-7](https://doi.org/10.1016/S0038-0717(00)00201-7)
- Colombani, N., Volta, G., Osti, A., Mastrocicco, M., 2016. Misleading reconstruction of seawater intrusion via integral depth sampling. *J. Hydrol.* 536, 320-326. <https://doi.org/10.1016/j.jhydrol.2016.03.011>
- Colombani, N., Cuoco, E., Mastrocicco, M., 2017. Origin and pattern of salinization in the Holocene aquifer of the southern Po Delta (NE Italy). *J. Geochem. Explor.* 175, 130–137. <https://doi.org/10.1016/j.gexplo.2017.01.011>

- Cook, P.G., Herczeg, A.L., 2012. Environmental tracers in subsurface hydrology. Springer New York, NY. <https://doi.org/10.1007/978-1-4615-4557-6>
- Da Lio, C., Carol, E., Kruse, E., Teatini, P., Tosi, L., 2015. Saltwater contamination in the managed low-lying farmland of the Venice coast, Italy: An assessment of vulnerability. *Sci. Tot. Environ.* 533, 356–369. <https://doi.org/10.1016/j.scitotenv.2015.07.013>
- Da Lio, C., Tosi, L., 2019. Vulnerability to relative sea-level rise in the Po river delta (Italy). *Estuar. Coast. Shelf Sci.* 228, 106379. <https://doi.org/10.1016/j.ecss.2019.106379>
- de Franco, R., Biella, G., Tosi, L., Teatini, P., Lozej, A., Chierozzo, B., Giada M., Rizzetto F., Claude C., Mayer A., Bassan V., Gasparetto-Stori, G., 2009. Monitoring the saltwater intrusion by time lapse electrical resistivity tomography: The Chioggia test site (Venice Lagoon, Italy). *J. Appl. Geophys.* 69(3-4), 117–130. <https://doi.org/10.1016/j.jappgeo.2009.08.014>
- de Louw, P.G.B., Essink, G.H.P.O., Stuyfzand, P.J., van der Zee, S.E.A.T.M., 2010. Upward groundwater flow in boils as the dominant mechanism of salinization in deep polders, The Netherlands. *J. Hydrol.* 394, 494–506. <https://doi.org/10.1016/j.jhydrol.2010.10.009>
- Di Giuseppe, D., Faccini, P., Mastrocicco, M., Colombani, N., Coltorti, M., 2014. Reclamation influence and background geochemistry of neutral saline soils in the Po River Delta Plain (Northern Italy). *Environ. Earth Sci.* 72(7), 2457–2473. <https://doi.org/10.1007/s12665-014-3154-4>
- Donnici, S., Serandrei-Barbero, R., Bini, C., Bonardi, M., Lezziero, A., 2011. The caranto paleosol and its role in the early urbanization of Venice. *Geoarchaeol.* 26, 514–543. <https://doi.org/10.1002/gea.20361>
- Donnici, S., Serandrei-Barbero, R., Canali, G., 2012. Evidence of climatic changes in the

- Venetian Coastal Plain (Northern Italy) during the last 40,000 years. *Sediment. Geol.* 281, 139–150. <http://dx.doi.org/10.1016/j.sedgeo.2012.09.003>
- Frascaroli, F., Parrinello, G., Root-Bernstein, M., 2021. Linking contemporary river restoration to economics, technology, politics, and society: Perspectives from a historical case study of the Po River Basin, Italy. *Ambio* 50(2), 492–504. <https://doi.org/10.1007/s13280-020-01363-3>
- Freeman, C., Ostle, N.J., Fenner, N., Kang, H., 2004. A regulatory role for phenol oxidase during decomposition in peatlands. *Soil Biol. Biochem.* 36, 1663–1667. <https://doi.org/10.1016/j.soilbio.2004.07.012>
- Gambolati, G., Putti, M., Teatini, P., Camporese, M., Ferraris, S., Gasparetto Stori, G., Nicoletti, V., Silvestri, S., Rizzetto, F., Tosi, L., 2005. Peat and oxidation enhances subsidence in the Venice watershed. *Eos* 86, 217-220. <https://doi.org/10.1029/2005EO230001>
- Gattacceca, J.C., Vallet-Coulomb, C., Mayer, A., Claude, C., Radakovitch, O., Conchetto, E., Hamelin, B., 2009. Isotopic and geochemical characterization of salinization in the shallow aquifers of a reclaimed subsiding zone: the southern Venice Lagoon coastland. *J. Hydrol.* 378(1-2), 46–61. <https://doi.org/10.1016/j.jhydrol.2009.09.005>
- Giambastiani B.M.S., Kananemariam A., Dagnew A., Antonellini M., 2021. Evolution of salinity and water table level of the phreatic coastal aquifer of the Emilia Romagna region (Italy). *Water* 13(3), 372. <https://doi.org/10.3390/w13030372>
- Grilli F., Accoroni S., Acri F., Bernardi Aubry F., Bergami C., Cabrini M., Campanelli A., Giani M., Guicciardi S., Marini M., Neri F., Penna A., Penna P., Pugnetti A., Ravaioli M., Riminucci F., Ricci F., Totti C., Viaroli P., Cozzi S., 2020. Seasonal and interannual trends of oceanographic parameters over 40 years in the northern Adriatic Sea in relation to nutrient

- loadings using the EMODnet chemistry data portal. *Water* 12(8), 2280.
<https://doi.org/10.3390/w12082280>
- Herrmann, A.G., 1972. Bromine distribution coefficients for halite precipitated from modern sea water under natural conditions. *Contrib. to Mineral. Petrol.* 37, 249–252.
<https://doi.org/10.1007/BF00373073>
- Huang, P.S., Chiu, Y.C., 2018. A simulation-optimization model for seawater intrusion management at Pingtung coastal area, Taiwan. *Water* 10(3), 251.
<https://doi.org/10.3390/w10030251>
- Hussain, M.S., Abd-Elhamid, H.F., Javadi, A.A., Sherif, M.M., 2019. Management of seawater intrusion in coastal aquifers: a review. *Water* 11(12), 2467.
<https://doi.org/10.3390/w11122467>
- Jiao, J.J., Wang, Y., Cherry, J.A., Wang, X., Zhi, B., Du, H., Wen, D., 2010. Abnormally high ammonium of natural origin in a coastal aquifer-aquitard system in the Pearl River Delta, China. *Environ. Sci. Technol.* 44(19), 7470–7475. <https://doi.org/10.1021/es1021697>
- Khaska, M., Salle, C.L.G.L., Lancelot, J., team, A., Mohamad, A., Verdoux, P., Noret, A., Simler, R., 2013. Origin of groundwater salinity (current seawater vs. saline deep water) in a coastal karst aquifer based on Sr and Cl isotopes. Case study of the La Clape massif (southern France). *Appl. Geochem.* 37, 212–227. <https://doi.org/10.1016/j.apgeochem.2013.07.006>
- Kuang, X., Jiao, J. J., Liu, K., 2015. Numerical studies of vertical Cl^- , $\delta^2\text{H}$ and $\delta^{18}\text{O}$ profiles in the aquifer–aquitard system in the Pearl River Delta, China. *Hydrol. Process.* 29, 4199–4209.
<https://doi.org/10.1002/hyp.10483>.
- Li, C., Gao, X., Li, S., Bundschuh, J., 2020. A review of the distribution, sources, genesis, and environmental concerns of salinity in groundwater. *Environ. Sci. Pollut. Res.* 27(33), 41157–

41174. <https://doi.org/10.1007/s11356-020-10354-6>

Lorenzen, G., Sprenger, C., Baudron, P., Gupta, D., Pekdeger, A., 2012. Origin and dynamics of groundwater salinity in the alluvial plains of western Delhi and adjacent territories of Haryana State, India. *Hydrol. Process.* 26, 2333–2345. <https://doi.org/10.1002/hyp.8311>

Lovrinović I., Bergamasco A., Srzić V., Cavallina C., Holjević D., Donnici S., Erceg J., Zaggia L., Tosi L., 2021. Groundwater monitoring systems to understand sea water intrusion dynamics in the Mediterranean: The Neretva valley and the southern Venice coastal aquifers case studies. *Water* 13(4), 561. <https://doi.org/10.3390/w13040561>

Manivannan, V., Elango, L., 2019. Seawater intrusion and submarine groundwater discharge along the Indian coast. *Environ. Sci. Pollut. Res.* 26, 31592–31608. <https://doi.org/10.1007/s11356-019-06103-z>

Mastrocicco, M., Colombani, N., 2021. The issue of groundwater salinization in coastal areas of the Mediterranean region: A review. *Water* 13(1), 90. <https://doi.org/10.3390/w13010090>

Mastrocicco, M., Giambastiani, B.M.S., Severi, P., Colombani, N., 2012. The importance of data acquisition techniques in saltwater intrusion monitoring. *Water Resour. Manag.* 26, 2851–2866. <https://doi.org/10.1007/s11269-012-0052-y>

Montety, V. de, Radakovitch, O., Vallet-Coulomb, C., Blavoux, B., Hermitte, D., Valles, V., 2008. Origin of groundwater salinity and hydrogeochemical processes in a confined coastal aquifer: Case of the Rhône delta (Southern France). *Appl. Geochem.* 23, 2337–2349. <https://doi.org/10.1016/j.apgeochem.2008.03.011>

Panno, S.V., Hackley, K.C., Hwang, H.H., Greenberg, S.E., Krapac, I.G., Landsberger, S., O'Kelly, D.J., 2006. Characterization and Identification of Na-Cl Sources in Ground Water. *Groundwater* 44, 176-187. <https://doi.org/10.1111/j.1745-6584.2005.00127.x>

- Park, S.-C., Yun, S.-T., Chae, G.-T., Yoo, I.-S., Shin, K.-S., Heo, C.-H., Lee, S.-K., 2005. Regional hydrochemical study on salinization of coastal aquifers, western coastal area of South Korea. *J. Hydrol.* 313, 182–194. <https://doi.org/10.1016/j.jhydrol.2005.03.001>
- Parrinello, G., Bizzi, S., Surian, N., 2021. The retreat of the delta: a geomorphological history of the Po River basin during the twentieth century. *Water Hist.* 13(1), 117–136. <https://doi.org/10.1007/s12685-021-00279-3>
- Rizzetto, F., Tosi, L., Carbognin, L., Bonardi, M., Teatini, P., 2003. Geomorphic setting and related hydrogeological implications of the coastal plain south of the Venice Lagoon, Italy. IAHS-AISH publication 463–470.
- Samantara, M.K., Padhi, R.K., Satpathy, K.K., Sowmya, M., Kumaran, P., 2015. Groundwater nitrate contamination and use of Cl/Br ratio for source appointment. *Environ. Monit. Assess.* 187, 50. <https://doi.org/10.1007/s10661-014-4211-x>
- Schuwirth, N., Hofmann, T., 2006. Comparability of and alternatives to leaching tests for the assessment of the emission of inorganic soil contamination. *J. Soil. Sediment.* 6, 102–112. <https://doi.org/10.1065/jss2005.10.149>
- Shalev, E., Lazar, A., Wolman, S., Kington, S., Yechieli, Y. and Gvirtzman, H., 2009. Biased monitoring of fresh water-salt water mixing zone in coastal aquifers. *Groundwater* 47, 49–56. <https://doi.org/10.1111/j.1745-6584.2008.00502.x>
- Stober, I., Bucher, K., 1999. Origin of salinity of deep groundwater in crystalline rocks. *Terra Nova* 11, 181–185. <https://doi.org/10.1046/j.1365-3121.1999.00241.x>
- Storms, J.E.A., Weltje, G.J., Terra, G.J., Cattaneo, A., Trincardi, F., 2008. Coastal dynamics under conditions of rapid sea-level rise: Late Pleistocene to Early Holocene evolution of barrier-lagoon systems on the northern Adriatic shelf (Italy). *Quat. Sci. Rev.* 27, 1107–1123.

<https://doi.org/10.1016/j.quascirev.2008.02.009>

- Sun, S., Li, M., Yan, M., Fang, X., Zhang, G., Liu, X., Zhang, Z., 2019. Bromine content and Br/Cl molar ratio of halite in a core from Laos: implications for origin and environmental changes. *Carbonate Evaporite* 34, 1107–1115. <https://doi.org/10.1007/s13146-019-00508-0>
- Teatini, P., Putti, M., Rorai, C., Mazzia, A., Gambolati, G., Tosi, L., Carbognin, L., 2009. Modeling the saltwater intrusion in the lowlying catchment of the southern Venice Lagoon, Italy. *WIT Trans. Ecol. Envi* 127, 351–362. <https://doi.org/10.2435/RAV090311>
- Teatini, P., Tosi, L., Viezzoli, A., Baradello, L., Zecchin, M., Strozzi, S., 2011. Understanding the hydrogeology of the Venice Lagoon subsurface with airborne electromagnetics. *J. Hydrol.* 411, 342–3549. <https://doi.org/10.1016/j.jhydrol.2011.10.017>
- Torresan, S., Critto, A., Rizzi, J., Marcomini, A., 2012. Assessment of coastal vulnerability to climate change hazards at the regional scale: the case study of the North Adriatic Sea. *Nat. Hazards Earth Syst. Sci.* 12, 2347–2358. <https://doi.org/10.5194/nhess-12-2347-2012>, 2012
- Tosi, L., Da Lio, C., Bergamasco, A., Cosma, M., Cavallina, C., Fasson, A., Viezzoli, A., Zaggia, L., Donnici, S., 2022. Sensitivity, hazard, and vulnerability of farmlands to saltwater intrusion in low-lying coastal areas of Venice, Italy. *Water* 14(1), 64. <https://doi.org/10.3390/w14010064>
- Tosi, L., Da Lio, C., Strozzi, T., Teatini, P., 2016. Combining L- and X-Band SAR interferometry to assess ground displacements in heterogeneous coastal environments: The Po River Delta and Venice Lagoon, Italy. *Remote Sens.* 8(4), 308. <https://doi.org/10.3390/rs8040308>
- Tosi, L., Da Lio, C., Teatini, P., Menghini, A., Viezzoli, A., 2018. Continental and marine surficial water - Groundwater interactions: The case of the southern coastland of Venice

- (Italy). Proc. Int. Assoc. Hydrol. Sci. 379, 387–392. <https://doi.org/10.5194/piahs-379-387-2018>
- Tosi, L., Rizzetto, F., Zecchin, M., Brancolini, G., Baradello, L., 2009. Morphostratigraphic framework of the Venice Lagoon (Italy) by very shallow water VHRS surveys: Evidence of radical changes triggered by human-induced river diversions. Geophys. Res. Lett. 36. <https://doi.org/10.1029/2008GL037136>
- Tran, L.T., Larsen, F., Pham, N.Q., Christiansen, A.V., Tran, N., Vu, H.V., Tran, L.V., Hoang, H.V., Hinsby, K., 2012. Origin and extent of fresh groundwater, salty paleowaters and recent saltwater intrusions in Red River flood plain aquifers, Vietnam. Hydrogeol. J. 20, 1295–1313. <https://doi.org/10.1007/s10040-012-0874-y>
- Viezzoli, A., Tosi, L., Teatini, P., Silvestri, S., 2010. Surface water-groundwater exchange in transitional coastal environments by airborne electromagnetics: The Venice Lagoon example. Geophys. Res. Lett. 37, L01402. <https://doi.org/10.1029/2009GL041572>
- Wen, X., Wu, Y., Su, J., Zhang, Y., Li, F., 2005. Hydrochemical characteristics and salinity of groundwater in the Ejina Basin, Northwestern China. Environ. Geol. 48, 665–675. <https://doi.org/10.1007/s00254-005-0001-7>
- Werner, A.D., Gallagher, M.R., 2006. Characterisation of sea-water intrusion in the Pioneer Valley, Australia using hydrochemistry and three-dimensional numerical modelling. Hydrogeol. J. 14(8), 1452–1469. <https://doi.org/10.1007/s10040-006-0059-7>
- Wu, P., Christidis, N., Stott, P., 2013. Anthropogenic impact on Earth's hydrological cycle. Nature Clim. Change 3(9), 807–810. <https://doi.org/10.1038/nclimate1932>
- Zancanaro, E., Teatini, P., Scudiero, E., Morari, F., 2020. Identification of the origins of vadose-zone salinity on an agricultural site in the Venice coastland by ionic molar ratio analysis.

Water 12(12), 3363. <https://doi.org/10.3390/w12123363>

Zecchin, M., Brancolini, G., Tosi, L., Rizzetto, F., Caffau, M., Baradello, L., 2009. Anatomy of the Holocene succession of the southern Venice lagoon revealed by very high-resolution seismic data. *Cont. Shelf Res.* 29, 1343–1359. <https://doi.org/10.1016/j.csr.2009.03.006>

Zhang, D., Yan, M., Fang, X., Yang, Y., Zhang, T., Zan, J., Zhang, W., Liu, C., Yang, Q., 2018. Magnetostratigraphic study of the potash-bearing strata from drilling core ZK2893 in the Sakhon Nakhon Basin, eastern Khorat Plateau. *Palaeogeogr. Palaeoclim. Palaeoecol.* 489, 40–51. <https://doi.org/10.1016/j.palaeo.2017.08.030>